

METALLIC THIN LAYERS AND NANOSTRUCTURES: FABRICATION AND CHARACTERIZATION

THÈSE N° 2169 (2000)

PRÉSENTÉE AU DÉPARTEMENT DE PHYSIQUE

ÉCOLE POLYTECHNIQUE FÉDÉRALE DE LAUSANNE

POUR L'OBTENTION DU GRADE DE DOCTEUR ÈS SCIENCES

PAR

Marcella GIOVANNINI

physicienne diplômée de l'Université de Genève
de nationalité suisse et originaire de Rivera (TI)

acceptée sur proposition du jury:

Prof. K. Kern, directeur de thèse

Dr K. Flipse, rapporteur

Prof. D. Pescia, rapporteur

Prof. Ph. Renaud, rapporteur

Lausanne, EPFL
2000

Abstract

The present thesis reports results on the controlled growth and on the magnetic properties of surface supported nanostructures.

The first part of the work deals with the self-organized growth of well-defined metal nanostructure on single-crystal metal surfaces. At the beginning we discuss strain relief in 2D nanostructures. We measured the minimal size an atomic monolayer (ML) thick Ag island on Pt(111) must have in order to contain dislocations. From comparison of this size with the mean spacing between dislocations in continuous Ag films we found direct evidence for strain relief at the island edge. The dislocation formation as a function of the island size, as well as the dislocation shape, were calculated using a *Frenkel-Kontorova* model. The comparison between calculation and experiment shows that the system Ag/Pt(111) is close to a commensurate-incommensurate phase transition which naturally explains strain relief at steps and annihilation of partial dislocations induced by the presence of Ag adatoms on the islands.

Subsequently, we studied the successive surface reconstructions as a function of film thickness of Ag and Cu grown epitaxially on Pt(111). For 2 ML Ag or Cu on Pt(111) the partial surface dislocations form regular ($n \times n$) networks ($n = 13$ for Cu/Pt(111), $n = 25$ for Ag/Pt(111)). These patterned surfaces were used afterwards as templates to grow a periodic island (Fe, Co, Ag) networks.

The three systems for which we found regular island formation are the growth of Ag on 2MLAg/Pt(111), of Co on 2MLCu/Pt(111), and of Fe on 2MLCu/Pt(111). The regular-island formation mechanism was elaborated for all cases. In the first system, dislocations of the 2MLAg/Pt(111) substrate are repulsive barriers for diffusing Ag atoms, whereas in the case of Co and Fe islands on 2MLCu/Pt(111), the dislocation intersection nodes are traps for diffusing atoms. The net result is similar for all three systems: a periodicity transfer from the dislocation network to the island array. The energy barriers for Ag atoms diffusing on the 2MLAg/Pt(111) dislocation network were quantitatively determined using Monte-Carlo simulations in comparison with temperature dependent experimental island densities (200 ± 30 meV for diffusion over the dislocations, 84 ± 8 meV for diffusion on the pseudomorphic stacking areas between the dislocations).

In the second part of the thesis, we performed *in situ* magnetic measurements on

thin films and islands. Using the magneto-optical Kerr effect. First, we measured the out-of-plane and in-plane magnetism of thin Co layers on Pt(111). Upon increasing film thickness, we observed a rotation of the magnetization easy axis from out-of-plane to in-plane. At room temperature, this transition takes place between 2 and 3 ML. Semi-quantitative measurements showed that the in-plane saturation magnetization increases linearly from 3 ML on up to the highest measured coverages of 22 ML. The out of plane magnetized for films thinner than 3 ML showed a strong coercive field increase around 1 ML. As a consequence, it was not possible to saturate the samples between ~ 0.5 and ~ 1.5 ML with the experimentally available magnetic field of 0.44 Tesla.

We also investigated the temperature dependence of our samples' magnetic behavior. The coercive field of any given film will decrease as the temperature rises up to the Curie temperature where it will completely disappear. This behavior is not different from bulk behavior. However, the Curie temperature of thin layers is much lower than that of bulk. The thinner the film, the lower the Curie temperature.

Finally, we measured the magnetism of ultrathin films in correlation with their topography. For example, we wanted to know what minimal size an island must have in order to exhibit ferromagnetic behavior, whether coalescence between islands is necessary for the appearance of ferromagnetism, or if the structure's height plays any role. We also measured the magnetism of the periodic island network described above.

The last part of this document reports on experiments done in collaboration with professor J. Kirschner's group at the *Max-Planck-Institut für Mikrostrukturphysik*, in Halle, (Germany) where we investigated correlations between magnetism and structure on films of Co grown on a thin (100) oriented W crystal which was used as a cantilever to detect stress in the Co films. For structure measurements, we applied low energy electron diffraction (LEED) together with beam deflection stress measurements. The magnetic properties of the thin Co films on W(100) were characterized with the Kerr technique.

Here again, the observed magnetization increase was proportional to the Co film thickness, up to at least 80 Å. From LEED measurements, the crystallographic structure (orientation and interatomic distances) of Co layers as a function of its thickness was inferred. LEED measurements showed in particular that the Co film grows pseudomorphically on W(100) up to 2-3 Å, corresponding to a ~ 1.5 to thickness of 2.5 ML. This was correlated to bending measurements, which showed a strain relief as the growth morphology changed from pseudomorphic to non-pseudomorphic.

Résumé

La présente thèse rend compte des résultats obtenus sur la croissance et l'étude de structures à l'échelle nanométrique.

La première partie de ce travail traite de la croissance auto-organisée de nanostructures métalliques bien définies sur des surfaces métalliques monocristallines. En premier lieu nous discutons comment des structures nanométriques bidimensionnelles relâchent leurs contraintes. Nous avons déterminé la taille minimale qu'une île d'une couche atomique d'épaisseur doit avoir pour contenir des dislocations. En comparant cette taille avec l'espacement moyen entre dislocations dans un film continu d'Ag, nous avons trouvé la preuve directe d'un relâchement des contraintes au bord des îles. La présence de dislocations en fonction de la taille des îles, ainsi que la forme des dislocations ont été calculées en utilisant le modèle de *Frenkel-Kontorova*. La comparaison entre les calculs et l'expérience montrent que le système Ag/Pt(111) est proche de la transition "commensurable-incommensurable", ce qui explique naturellement le relâchement des contraintes sur les bords et l'annihilation des dislocations partielles induites par la présence d'atomes d'Ag adsorbés sur les îles.

Par la suite, nous avons étudié les différentes reconstructions de surfaces obtenues lors de la croissance épitaxiale du Cu sur Pt(111) et de l'Ag sur Pt(111) pour différentes épaisseurs. Pour deux couches atomiques de Cu ou d'Ag sur Pt(111), les dislocations partielles de surface forment un réseau régulier ($n \times n$), ($n = 13$ pour le Cu sur Pt(111) et $n = 25$ pour l'Ag sur Pt(111)). Nous avons par la suite utilisé ces surfaces structurées comme patrons pour faire croître des réseaux d'îlots périodiques (de Co, Fe et Ag).

Les trois systèmes nous ayant permis de faire croître des réseaux d'îlots réguliers sont la croissance d'Ag sur 2MLAg/Pt(111)¹, de Co sur 2MLCu/Pt(111) et de Fe sur 2MLCu/Pt(111). Le mécanisme de formation des îlots réguliers a été élaboré pour ces trois systèmes. Dans le premier système, les dislocations formées par 2MLAg/Pt(111) sont des lignes répulsives pour les atomes d'Ag, alors que pour les îlots de Co et de Fe sur 2MLCu/Pt(111), les nœuds de croisement des dislocations agissent comme des pièges pour les atomes. Le résultat final est semblable pour les trois systèmes: un transfert de la périodicité du réseau sur les îlots. Des simulations de Monte-Carlo comparées aux résultats expérimentaux de densités d'îles, nous ont permis de déduire les barrières d'énergie pour la diffusion des atomes d'Ag sur le réseau de dislocations formé par 2MLAg/Pt(111) (200 ± 30 meV pour passer par dessus les dislocations, et 84 ± 8 meV

¹Nous utilisons l'abréviation anglaise ML (MonoLayer) pour couche d'épaisseur monoatomique, 2MLAg/Pt(111) signifiant deux couches atomiques d'Ag déposées sur le Pt(111).

pour diffuser entre les dislocations).

Dans la deuxième partie de cette thèse, nous avons effectué des mesures magnétiques de nos films et îlots à l'aide d'un appareil de détection utilisant l'effet Kerr, que nous avons monté sur notre chambre expérimentale pour des mesures *in situ*. Tout d'abord, nous avons mesuré le magnétisme de fines couches de Co sur Pt(111), dans le plan et normalement au plan. Nous avons observé une rotation de l'axe d'aimantation préférentiel, de normal à parallèle au plan lorsque l'épaisseur du film augmente. A température ambiante, cette transition a lieu entre deux et trois couches atomiques. Des mesures semi-quantitatives ont montré que l'aimantation de saturation dans le plan augmente linéairement à partir de 3 ML et jusqu'aux épaisseurs maximales mesurées (22 ML). L'aimantation hors du plan pour les films plus fin que 3 ML, montre une forte augmentation du champ coercitif autour de 1 ML, avec pour conséquence l'impossibilité de saturer les échantillons entre ~ 0.5 et ~ 1.5 ML avec l'aimant à notre disposition.

Nous nous sommes aussi intéressés à la dépendance en température du comportement magnétique de nos échantillons. Ainsi, le champ coercitif d'un film donné va diminuer lorsqu'on augmente sa température, jusqu'à disparaître entièrement à la température de Curie. Ce comportement n'est pas différent de celui des échantillons massifs. Cependant, la température de Curie des films ultrafins est beaucoup plus basse que celle d'un échantillon massif. Plus le film est fin, plus la température de Curie diminue.

Finalement nous avons fait des mesures magnétiques corrélées à des mesures de topographie. Par exemple, nous avons voulu savoir à partir de quelle taille d'îlots un comportement ferromagnétique est possible, si la coalescence entre les îles est nécessaire pour un tel comportement, ou si la hauteur des structures joue un rôle. Nous avons également mesuré le magnétisme des structures d'îlots réguliers décrit plus haut.

La dernière partie de ce document rapporte un travail fait en collaboration avec le groupe du professeur J. Kirschner au *Max-Planck-Institut für Mikrostrukturphysik*, à Halle en Allemagne. Nous y avons étudié les corrélations entre magnétisme et structure sur des films de Co évaporés sur une fine lamelle de W, orientée (100). Nous disposions pour les mesures de structures d'un diffractographe aux électrons de basse énergie (LEED) ainsi que de mesures de torsion de la lamelle; les mesures magnétiques ont été faites à l'aide d'un appareil de détection utilisant l'effet Kerr.

L'augmentation de l'aimantation est, ici aussi, proportionnelle à l'épaisseur des films de Co, et ce au moins jusqu'à 80 Å. A l'aide des mesures LEED, nous avons pu déduire la structure cristallographique (orientation et distance interatomique) qu'adopte le Co en fonction du nombre de couches atomiques déposées. En particulier les mesures LEED ont montré que le film de Co croît de façon pseudomorphe au W(100) jusqu'à 2-3 Å, correspondant à un film de Co de ~ 1.5 à 2.5 ML d'épaisseur. Ce résultat est mettre en corrélation avec les mesures de torsions qui révèlent un relâchement de la contrainte lorsque le mode de croissance passe de pseudomorphe à non-pseudomorphe.

Contents

Abstract	i
Résumé	iii
1 Introduction	1
2 The Surface Magneto-Optical Kerr Effect	5
2.1 Introduction	5
2.2 Theoretical framework	7
2.2.1 Macroscopical derivation of the Kerr ellipticity and Kerr rotation	8
2.2.2 The classical theory	11
2.2.3 The quantum theory	12
3 Experimental	14
3.1 The ultra high vacuum chamber and its measurements tools	14
3.2 The SMOKE measurement method	17
4 Nucleation and growth of Ag and Cu on the Pt(111) substrate	23
4.1 Introduction to nucleation theory	23
4.2 Strain relief at hexagonally close-packed surfaces	29
4.2.1 Cu growth on Pt(111)	33
4.2.2 Ag growth on Pt(111)	38
5 Nanofabrication of regularly dispersed islands	45
5.1 Nucleation of Ag on 2MLAg/Pt(111)	45
5.2 Nucleation of Co and Fe on 2MLCu/Pt(111)	55
5.2.1 Attempt of Co and Fe nucleation on 2MLAg/Pt(111)	55
5.2.2 Creating regularly spaced islands of Co and Fe on 2MLCu/Pt(111): formation mechanism	56
6 Magnetic behavior of thin films and islands	64
6.1 Co/Pt(111)	64
6.1.1 Experimental procedures	64

6.1.2 Results	65
6.2 Co/2MLCu/Pt(111)	79
6.3 Co/W(100)	81
7 Conclusion and Outlook	89
A Signification of the main symbols used:	92
B List of the acronyms used in the text	93
List of Publications	99
Curriculum Vitae	100
Remerciements	101

Chapter 1

Introduction

Research on nanoscale structures has tremendously developed over the last two decades. Nanostructures are involved in all sorts of research fields, from fundamental physics to biology, including astronomical [1] and medical [2] applications. There are two main reasons of this strong interest in nanoscale structures: First, from a pure fundamental point of view, their fabrication allows the study of physical properties that differ strongly from those observed in macroscopic material or in single atoms. Chemical and physical properties of nanostructures depend on their size and shape. Thus the possibility of fabricating nanostructures opens a new field of research and will eventually allow a more complete understanding of the laws of nature. Second, from the technological point of view, mastering nanostructure fabrication opens new and interesting prospects. One of the possible applications is the ever increasing miniaturization of electronic devices, such as memory devices or detectors. But the physics happening at the nanoscale can also be exploited to fabricate completely new devices based on different principles than the actual electronic devices, such as the magnetic processing of data [3].

One possibility to grow surface-supported nanostructures and thin layers is by Molecular Beam Epitaxy (MBE): a beam of atoms or molecules of a substance is directed a onto a substrate, on which the condensated adatoms diffuse and arrange to form islands and layers. The shape and size of the structures formed depends on the materials involved, on temperature and on the deposition flux. These structures are said to be self-assembled, in opposition to structures formed by assembling single atoms with the tip of an STM, or by lithography methods.

In recent years, intensive efforts have been made to understand the atomic processes involved during growth, in order to gain control over the structures formed during MBE. For example, the atomic processes play an important role in thin layer growth morphology or in dendritic island formation as further explained below.

Film growth is usually classified in three growth modes [4, 5]: the Frank-Van der Merwe growth, when the layer grows 2D or layer by layer, the Volmer-Weber or three dimensional growth, and an intermediate mode, the Stranski-Krastanov mode where the first few layers grow 2D, and a transition to 3D growth occurs at a critical thickness. From a thermodynamic point of view, which of these modes appears depends on the

interface free energy between the substrate and the adsorbate, and on the surface free energies of both elements. However MBE growth normally occurs far from thermodynamic equilibrium, and is governed by atomic processes like terrace-diffusion, step-diffusion, adatom trapping on or exchange in the substrate, and so on. It was found that the presence of impurities in the substrate, the step density, or the substrate temperature could strongly influence the layer growth mode (see for example [6]).

The dendritic island formation is another example of the importance of atomic processes on the substrate. According to the diffusion-limited aggregation (DLA) model, where 2D islands are formed as randomly diffusing particles stick irreversibly to the perimeter of a growing aggregate, the resulting islands are randomly ramified. In many real systems however, dendritic islands form with preferred growth directions [7,8]. This was shown [9] to be due to the diffusion of atoms at the island edges, which is more or less favored depending on the coordination of the diffusing atom to the islands and to the underlying substrate in the transition state. The symmetry observed in dendritic growth is correlated to the substrate symmetry.

In the present thesis, we study metallic ultrathin layers and nanostructures. We focus on two aspects: controlled fabrication of nanostructures, and the characterization of their magnetic properties ($M_{saturation}$, $H_{coercitive}$, T_{Curie}). The fabrication part includes heteroepitaxial growth studies, in particular the pattern formed by strain-induced dislocations on different systems, and nucleation experiments on the patterned substrates.

Our main analysis tool for the structure characterization part was the scanning tunneling microscope (STM). Developed in 1986 by Binning *et al.* [10, 11], this very powerful technique allows real-space imaging of surfaces at the atomic scale. It also permits the manipulation of atoms and molecules, letting the experimentalist form new artificial structures atom by atom [12,13]. However, we did not use the STM to form the nanostructures presented here. The main drawback of the controlled assembly of atoms with the help of the STM is that it is a serial, thus time-consuming method. We wanted to control the nanostructure growth in parallel for all islands formed, thus enabling the application of macroscopic, averaging tools for physical properties measurements such as the magnetism.

It was possible for instance to control the dislocation patterns formed during heteroepitaxy by adjusting the sample temperature. With these dislocation patterns as template, a set of 2D islands, constant in size and regularly dispersed, were obtained by evaporating a metal (on a patterned substrate) at a given temperature.

Once the controlled nanostructure fabrication was mastered, we performed magnetic measurements on these nanostructures. These were done using a Surface Magneto-Optical Kerr Effect (SMOKE) device that was mounted onto the experimental Ultra High Vacuum (UHV) chamber. SMOKE is a very convenient way to measure surface magnetism *in situ* in UHV. The laser source and the detector can be outside the chamber, the laser-beam passing through a window. The sample magnetization is measured by the change in polarization of the reflected light.

The interest of probing the magnetism of nanostructures comes from the fact that ferromagnetism is a collective effect between the spins of each of the atoms constituting

a magnet. It is therefore not clear whether ferromagnetism shows up for structures with reduced dimensions, or whether it appears for a structure formed by a small number of atoms. Many experimental studies have been and are still done on the magnetism of nanostructures and thin layers, leading to important discoveries from the fundamental as well as from the applied point of view. For example it was found in the 80s, that the direction of the magnetic moment of ultrathin Fe layers deposited on Ag(100) was out of plane, whereas it is in-plane for thicker films. contrary to what's happening for thicker films [14]. Perpendicular anisotropies were then found in many other epitaxial systems, and they are now exploited in recording medias based on Co/Pt(111) multilayers [15], which allows a higher storage density. Other important discoveries include giant magnetoresistance effects [16, 17], the enhanced magnetic moment for monolayers with respect to bulk materials or the film thickness dependence of the Curie temperature. The subject of thin-layer and nanostructure magnetism is far from being dealt with, in particular the studies of submonolayer magnetism are only at their beginning.

In this work, we study magnetic structures with reduced-dimensions. The main advantage of our experimental chamber is that it combines a magnetic measurement tool (the SMOKE) with a very powerful topographic tool (the STM), allowing a precise characterization of the structure-magnetism correlation in surface supported nanostructures.

The present document is divided in seven chapters, the first one being this introduction. The second chapter introduces the Kerr technique used to measure the magnetic properties of the sample. It gives a brief outline of the physics involved in the magneto-optical Kerr effect. The third chapter describes the experimental setup: the UHV chamber, the sample preparation and the main measurement tools, the STM and the SMOKE system.

Our results are presented in the fourth, fifth and sixth chapters. The fourth chapter focuses on the heteroepitaxial growth and on the formation of surface dislocations. It begins with an introduction to nucleation theory. Then the strain relief process in heteroepitaxy on hexagonal close-packed substrate is discussed as a function of film thickness for two systems: Cu and Ag heteroepitaxy on Pt(111). The different ways these systems can relieve strain are described, as well as the patterns formed by this strain relief. In particular the regular network of dislocations obtained for both systems is described in detail. We also discuss the mean dislocations interspacing for submonolayer Ag on Pt(111) and the appearance of dislocations in Ag islands on Pt(111) as a function of the island sizes. Experimental results are compared with theoretical calculations, using a Frenkel-Kontorova (FK) model.

Regularly dislocated surfaces are used as a substrate to fabricate nanostructures in parallel, as exposed in chapter five. Regular arrays of islands were obtained for three metals: silver, cobalt and iron. The last two were chosen for their magnetic properties. The mechanisms involved in the regular island formation are described in detail. For the Ag nucleation case in particular, atomic processes during nucleation

were identified. Kinetic Monte-Carlo simulations were performed in order to confirm our results concerning the regular-island formation mechanism and to extract the diffusion barriers energies on the dislocated substrate. On the other hand, for silver and cobalt, it was by the careful observation of the STM images that we were able to understand the mechanisms involved during nucleation.

The sixth chapter includes all magnetic measurements done on the Co structures and layers presented in chapters four and five. It also includes the results obtained on a different system Co/W(100) that was studied in collaboration with Prof. J. Kirschner's group at the Halle Max-Planck Institute Germany, during the author's stay in that institute. The chapter is divided in three parts: Co/Pt(111), Co/2MLCu/Pt(111) and Co/W(100).

In the Co/Pt(111) part, we report results on thin-layer magnetism as a function of layer thickness. The influence of deposition- and measurement-temperature on film magnetism is investigated. For submonolayer coverage, we focus on the role of coalescence and the island's height on the magnetism of the system.

The second part, on Co/2MLCu/Pt(111), reports the magnetic measurement results on the regular network of islands. Measurements were performed at different Co coverages (*i.e.* different island sizes), and different sample temperatures.

Finally, for the Co/W(100), thin-layer magnetism is correlated with crystallographic structures characterized by LEED measurements as a function of film thickness. Stress measurements were also performed *in situ* during film growth. Correlation between film stress and crystallographic structure is also investigated.

The thesis ends with a conclusion in which the important results discussed in the document are summarized, and suggestions are made for further research and possible improvements to our experimental chamber in an outlook.

Chapter 2

The Surface Magneto-Optical Kerr Effect

Magnetic measurements of the fabricated thin layers and nanostructures constitute an important part in the present work. These magnetic measurements were done using the Surface Magneto-Optical Kerr Effect (SMOKE). The SMOKE is a very sensitive tool to probe thin layer magnetism, and is very convenient to use for *in situ* measurements inside the Ultra High Vacuum (UHV) chamber, since the laser-diode source as well as the photodiode detector can be placed outside the chamber. Developing and optimizing a SMOKE setup on our UHV chamber was also part of the present thesis. The experimental setup is described in chapter 3. The present chapter deals with the SMOKE principles and the SMOKE measurement method.

2.1 Introduction

The Surface Magneto-Optical Kerr Effect is one among many Magneto-Optical (MO) phenomena. By MO phenomena, we mean all effects which occur when light interacts with a magnetized sample. For example the Zeeman effect (which is the variation of the frequency of light emitted by atoms when placed in a magnetic field) is a MO effect, as well as the Faraday, the Cotton-Mouton or the Voigt effects. Before giving a more detailed description of the SMOKE, we shall give a brief overview of some other MO phenomena and their discoveries.

The first MO effect discovered was the Faraday effect. It was first observed in 1845 in a piece of glass placed between the poles of a magnet [18]. Faraday observed that when linearly polarized light propagates through a magnetizable medium placed in a magnetic field, its plane of polarization rotates in the medium. This effect is explained by circular birefringence, i.e. different indices of refraction for the left and right circularly polarized light, in which the linearly polarized wave can be decomposed. It implies also circular dichroism because of the relation between the absorption coefficient and the index of refraction. The Voigt effect, a special case of the Faraday effect, is the

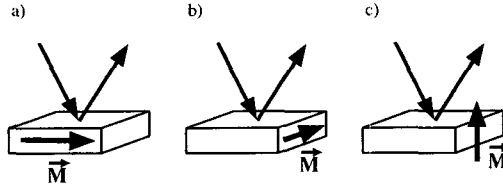


Figure 2.1: The three standard configurations for MOKE: a) Longitudinal configuration. The magnetic field is in the plane of the sample surface, and parallel to the incident light. b) Transverse configuration. The magnetic field is in the plane of the sample surface, but perpendicular to the incident light. c) Polar configuration. The magnetic field is normal to the sample surface.

linear birefringence observed when the light is propagating through a medium in a direction perpendicular to the applied magnetic field. The Cotton-Mouton effect appears in a liquid whose molecules are electrically and magnetically anisotropic. The applied magnetic field orients the molecules and induces a linear birefringence in the medium.

The Kerr effect, known as the Magneto-Optical Kerr Effect (MOKE) was discovered by J. Kerr in 1876 [19, 20], about 30 years after the Faraday effect. It is the analog of the Faraday effect, only not in transmission but in reflection of light at a magnetized medium. There are three standard configurations for the MOKE (polar, transverse and longitudinal) depending on the relative orientations of the magnetic field, the surface and the incident light. These configurations are sketched in Fig. 2.1. In the polar Kerr Effect, the magnetization is perpendicular to the plane of the film. In the transverse Kerr Effect the magnetization is in the film plane and perpendicular to the plane formed by the incident and reflected light, whereas in the longitudinal Kerr Effect, the magnetization, also lying in the plane of the film, is oriented parallel to the plane formed by the incident and reflected light.

In longitudinal and polar Kerr effects, linearly polarized light acquires a Kerr rotation and a Kerr ellipticity upon reflection. Fig. 2.2 sketches the transformation of the electric field after reflection on the magnetized sample. The part of the induced response which is in-phase with the incident light is responsible for the light rotation, while the out-of-phase part gives rise to the ellipticity.

When the magnetization direction of the sample is reversed, the Kerr rotation and ellipticity reverse sign. The rotation and ellipticity induced by the polar Kerr effect is an order of magnitude larger than those induced by the longitudinal Kerr effect. The transverse Kerr effect is different from the two others in that it doesn't change the polarization of an incident linearly polarized wave, nor does it induce ellipticity.

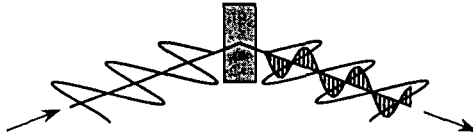


Figure 2.2: Schematic representation of the magneto-optic interactions. The incident light is linearly polarized, and the light reflected from the magnetized film has a Kerr rotation and a Kerr ellipticity. (Taken from [21])

This is because there is no component of the light propagating along the magnetization direction. The only effect seen in this case is a small change in reflectivity upon magnetization reversal, but only for p-polarized light (i.e. for light for which the polarization vector is in the incident-reflected light plane, contrary to s-polarized light which has its polarization vector perpendicular to the incident-reflected light plane).

The Surface Magneto-Optical Kerr Effect (SMOKE) is the MOKE applied to surfaces, where only a few monolayers at the sample surface are made of a magnetic material, whereas the bulk is nonmagnetic. It was first used in 1985 as an experimental technique to study surface magnetism of iron monolayers epitaxially deposited on Au(111) [22]. The three standard MOKE configurations (polar, longitudinal and transverse) are still valid for SMOKE, since these two names stand for one single technique. One of the characteristics of SMOKE is that the measured signal (Kerr rotation for longitudinal and polar SMOKE; Kerr attenuation in the case of transverse SMOKE) is proportional to the quantity of magnetic material deposited on the substrate (up to a few hundred Angstroms): if the depth of penetration of the incident light in the sample is bigger than the magnetic material layer thickness, as the SMOKE signal is proportional (to first order) to the magnetization, then it is also proportional to the magnetic film thickness. For metals, the distance over which light penetrates, given by the optical skin depth, is typically 150 to 200 Angstroms [23].

The physical origin of the Kerr effect in ferromagnetic metals lies in the spin-orbit interaction between the electron spin and the orbital angular momentum [24]. The electric field of the light interacts with the electron dipoles via the orbital wavefunctions, which are in turn influenced by the electron spin via the spin-orbit interaction [25]. This is explained in more detail in the next section.

2.2 Theoretical framework

In this section we shall give a concise theoretical explanation for the MOKE in two steps. In section 2.2.1, we present a macroscopical approach relating the Kerr ellipticity and the Kerr rotation to the dielectric susceptibility term through Maxwell's equations. The dielectric susceptibility tensor can then be calculated by microscopic theories, either

classical or quantum mechanical. The classical approach gives a direct (although not exact) understanding of the physics behind the Kerr phenomena and is presented in section 2.2.2. We shall discuss the limits of this approach, and give the broad lines and results of the quantum mechanical calculation in section 2.2.3.

One can also set out and calculate the absolute values of the Kerr ellipticity and the Kerr rotation for a specific system [26]. This allows to correlate quantitatively the Kerr signal to the sample magnetization. However, we refer the reader to further literature for such calculations since they are beyond the scope of the present thesis. Typically, and also in this thesis, SMOKE is used to characterize the qualitative magnetic behavior of the thin films, like ferro- para- or superparamagnetism and the coercive field. The saturation magnetization or the magnetic moment per atom are not inferred. In a review article, H. Ebert [26] gives an overview of different theoretical approaches. He also presents a theoretical derivation of the optical conductivity tensor in transition metals. Closer to our measurements, P. M. Oppeneer gives the results of *ab initio* calculations made for Fe and Ni [27]. This field of research is still active, and recent papers present new calculations of the MOKE [28].

2.2.1 Macroscopical derivation of the Kerr ellipticity and Kerr rotation

Assuming that the form of the electric susceptibility tensor χ_e ($\mathbf{P} = \chi_e \epsilon_0 \mathbf{E}$) is known, magneto-optical effects can be described using Maxwell's equations¹:

$$\nabla \times \mathbf{E} = -\frac{\partial \mathbf{B}}{\partial t} \quad (2.1)$$

$$\nabla \times \mathbf{B} = \mu_0 \frac{\partial \mathbf{D}}{\partial t}, \quad (2.2)$$

where $\mathbf{D} = \epsilon \mathbf{E}$ and $\epsilon = \epsilon_0(1 + \chi_e)$ is the dielectric function.

The magneto-optical effect is contained in the dielectric function, or in an equivalent way, in the dielectric permittivity tensor $\kappa = (1 + \chi_e) = \epsilon/\epsilon_0$, which depends on the material and on the applied magnetic field vector. For a plane wave propagating through the medium:

$$\mathbf{E} = \mathbf{E}_0 e^{i(\omega t - \mathbf{k} \cdot \mathbf{r})} \quad (2.3)$$

$$\mathbf{B} = \mathbf{B}_0 e^{i(\omega t - \mathbf{k} \cdot \mathbf{r})}, \quad (2.4)$$

we have: $\nabla \rightarrow -i\mathbf{k}$ and $\frac{\partial}{\partial t} \rightarrow i\omega$. Taking the curl of Equ. 2.1 and using Equ. 2.2, we have:

$$\begin{aligned} \nabla \times (\nabla \times \mathbf{E}) &= -\nabla \times \frac{\partial \mathbf{B}}{\partial t} \\ -i\mathbf{k} \times (-i\mathbf{k} \times \mathbf{E}) &= \mu_0 \epsilon \omega^2 \mathbf{E}, \end{aligned}$$

¹We use MKSA units; bold symbols denote vectorial and tensorial quantities. A review of all symbols used in this chapter is given in appendix

and finally \mathbb{I} is the unitary matrix):

$$(k^2\mathbb{I} - \mathbf{k}\mathbf{k} - \omega^2\mu_0\epsilon)\mathbf{E}_0 = 0, \quad (2.5)$$

or in components:

$$(k^2\delta_{lm} - k_l k_m - \omega^2\mu_0\epsilon_{lm})E_{0m} = 0. \quad (2.6)$$

Replacing $\epsilon_0\mu_0$ by $\frac{1}{c^2}$, using $k_0 \equiv \omega/c$, and with the index of refraction given by $\mathbf{n} = \mathbf{k}/k_0$, Equ. 2.5 can be rewritten:

$$(n^2\mathbb{I} - \mathbf{k}\mathbf{k}/k_0 - \kappa)\mathbf{E}_0 = 0. \quad (2.7)$$

Equ. 2.7 possesses a nontrivial solution for \mathbf{E}_0 only if the above matrix determinant vanishes. This gives an equation for n which is called Fresnel equation [29]. This equation is quadratic in n and depends on the direction of \mathbf{k} , yielding two values for n for each direction of \mathbf{k} .

An isotropic or cubic medium with an applied field in the z direction has a dielectric permittivity tensor of the form²:

$$\kappa = \begin{pmatrix} \kappa_1 & \kappa_2 & 0 \\ -\kappa_2 & \kappa_1 & 0 \\ 0 & 0 & \kappa_3 \end{pmatrix}, \quad (2.8)$$

where κ_2 is an odd function of the magnetization \mathbf{M} whereas κ_1 and κ_3 are even functions of \mathbf{M} . As an example, for a wave propagating along the magnetic field direction, the solutions of Fresnel's equation are [30]:

$$n_{\pm}^2 = \kappa_1 \pm i\kappa_2, \quad (2.9)$$

the plus and minus sign corresponding to a solution for right circularly polarized (RCP) light, respectively for left circularly polarized (LCP) light.

To quantify the MOKE effect, it is necessary to calculate the reflection coefficients. These are obtained by taking into account the electromagnetic boundary conditions, i.e. the continuity of the normal component of \mathbf{H} and of the tangential component of \mathbf{E} at the surface of the reflecting medium.

Let us first consider the polar Kerr effect at normal incidence. The proper modes are then RCP and LCP waves with indices of refraction given by Equ. 2.9. The reflected amplitude for each mode (noted + and -) are given by:

$$r_{\pm} = E_{1\pm}/E_{0\pm} = -\frac{n_{\pm} - 1}{n_{\pm} + 1} \quad (2.10)$$

²Note that magneto-optical effects on isotropic materials or cubic crystals make them act as anisotropic uniaxial crystals, whose main axis is in the applied magnetic field direction. Thus the form of κ here is the same as that of an uniaxial crystal

We can write $r_{\pm} = |r|e^{i\phi}$, which yields:

$$\frac{r_+}{r_-} = \left| \frac{r_+}{r_-} \right| e^{i(\phi_+ - \phi_-)}. \quad (2.11)$$

Thus, for an incident linearly polarized light which can be resolved in an RCP and an LCP component of equal magnitude, the reflected light will be elliptically polarized due to a difference in amplitude of the two reflected circular components. Moreover the major axis of the ellipse will be rotated with respect of the direction of polarization of the incident light due to the phase difference introduced between the two reflected circular components. So the reflected light is characterized by a Kerr ellipticity and a Kerr rotation which are given by:

$$\begin{aligned} \epsilon_K &= -\text{Re} \left(\frac{n_+ - n_-}{n_+ n_- - 1} \right), \\ \theta_K &= -\text{Im} \left(\frac{n_+ - n_-}{n_+ n_- - 1} \right). \end{aligned}$$

Or using the complex Kerr rotation: $\phi_K = \theta_K + i\epsilon_K$,

$$\phi_K \approx i \frac{\sqrt{n_+} - \sqrt{n_-}}{\sqrt{n_+ n_-} - 1} \approx \frac{\sigma_{xy}}{\sigma_{xx} \sqrt{1 + (4\pi i/\omega)\sigma_{xx}}} \quad (2.12)$$

Note that we use here the electric conductivity tensor σ instead of the permittivity tensor κ . These quantities are related by the Hartree-Appleton relation:

$$\epsilon_0 \kappa = \epsilon = \frac{\sigma}{-i\omega} + \epsilon_0 \quad (2.13)$$

This result is correct for the polar Kerr effect at normal incidence. When light reflects from the sample at oblique incidence, the calculations become more complicated because the normal modes are not pure RCP and LCP waves anymore. Results [30] for the two geometries, polar and transverse at oblique incidence, used in the present thesis are given below, where we denote by s and p the two linear polarizations perpendicular and parallel to the plane of incidence, r_{sp} being $\frac{r_s}{r_p}$, or the amplitude of the p reflected wave for s incident wave. These results are correct through terms of order \mathbf{M} , thus we use $\epsilon_1 = \epsilon_3 \approx n_0^2$, $|\epsilon_2| \ll \epsilon_1$.

Polar:

$$\begin{aligned} r_{pp} &= \frac{n_0 \gamma - \gamma'}{n_0 \gamma + \gamma'} & r_{ss} &= \frac{\gamma - n_0 \gamma'}{\gamma + n_0 \gamma'} \\ r_{sp} &= r_{ps} = \frac{\epsilon_2/n_0}{(\gamma + n_0 \gamma')(n_0 \gamma + \gamma')} \end{aligned} \quad (2.14)$$

Transverse:

$$\begin{aligned} r_{pp} &= \frac{n_0 \cos \theta_0 - 1}{n_0 \cos \theta_0 + 1} \left(1 + \frac{(\sin 2\theta_0) \epsilon_2 / n_0}{n_0^2 \cos^2 \theta_0 - 1} \right) \\ r_{ss} &= \frac{\cos \theta_0 - n_0}{\cos \theta_0 + n_0} \end{aligned} \quad (2.15)$$

In these equations, $\gamma = \cos\theta_0$ and $\gamma' = \sqrt{1 - \sin^2\theta_0/n_0^2}$. Note that in the transverse Kerr configuration, the proper modes of Equ. 2.7 are s and p polarized waves, with $n_s^2 = \kappa_3 = n_0^2$ and $n_p = \kappa_1 + \kappa_2^2/\kappa_3$. Only the p wave is sensitive to the magnetization through the term κ_2 which is to first approximation proportional to \mathbf{M} . Thus in the transverse Kerr configuration, the reflected wave only changes in intensity upon reversal of the magnetization, as already mentioned in section 2.1.

In a publication of 1996, Chun-Yeol You and Sung-Chul Shin [31] showed that for an arbitrary magnetization direction and oblique incidence, the Kerr effect can be expressed as the product of two factors: a prefactor which is a simple function of the optical parameters of the media and the direction of the magnetization, and a main factor which is just the polar Kerr effect at normal incidence.

2.2.2 The classical theory

In a first approach, magneto-optical effects can be understood through the electrons of the solid being subjected to the Lorentz force. In a classical picture, we consider a system of harmonically bound electrons in an oscillating electric field and with a static magnetic field along the z axis, which is taken normal to the sample surface (the electron's motion being in the sample surface plane). It is easy to see that an electric field in the x direction will produce a motion of the electrons in the x direction and thereby, because of the z -direction of the magnetic field, causes a force on the electrons in the y -direction. Thus the motion of the electron will rotate from the x direction towards the y direction. The equation of motion of each electron is:

$$m\ddot{\mathbf{r}} + b\dot{\mathbf{r}} + k\mathbf{r} = -e\mathbf{E}_0 e^{j\omega t} - e\mu_0 \dot{\mathbf{r}} \times \mathbf{H} \quad (2.16)$$

where b is a damping coefficient, and $(k/m)^{1/2}$ is the natural frequency of the electron (k stands for the force constant of the periodic electron potential). The last term is the Lorentz force. The substitution $\mathbf{r} = \mathbf{r}_0 e^{j\omega t}$ yields a pair of equations for the x and y components of \mathbf{r}_0 that are coupled by the Lorentz force. By solving these equations, we find that the amplitude of the electric dipole moment $-e\mathbf{r}_0$ is a linear function of \mathbf{E}_0 , the coefficients being the elements of the electric susceptibility of the harmonically bound electron (by definition: $\mathbf{P} = \chi_e \epsilon_0 \mathbf{E}$). For an assembly of N such oscillators the polarizability is [30]:

$$\begin{aligned} \chi_{xx} = \chi_{yy} &= \frac{Ne^2}{\epsilon_0 m} \frac{\omega_0^2 - \omega^2 + i\omega\gamma}{(\omega_0^2 - \omega^2 + \omega\gamma)^2 - 4\omega^2\omega_L^2} \\ \chi_{xy} = -\chi_{yx} &= \frac{Ne^2}{\epsilon_0 m} \frac{-2i\omega\omega_L}{(\omega_0^2 - \omega^2 + \omega\gamma)^2 - 4\omega^2\omega_L^2} \\ \chi_{zz} &= \frac{Ne^2}{\epsilon_0 m} \frac{1}{\omega_0}, \end{aligned} \quad (2.17)$$

where $\gamma = b/m$ is the width of the resonance and $\omega_L = e\mu_0 \mathbf{H}/2m$ is the Larmor precession frequency. The free electron limit is obtained by allowing $\omega_0 \rightarrow 0$. In the absence of a magnetic field, the off-diagonal elements vanish and χ is scalar.

2.2.3 The quantum theory

The classical picture presented above is not adequate for the description of ferromagnetic systems. First it cannot explain that the Kerr rotation is larger by several orders of magnitude in ferromagnets than in paramagnetic materials [24]. Moreover it does not take into account the magnetization direction dependence of the tensor $\sigma(\omega)$. This magnetization direction dependence comes from the fact that the presence of a spontaneous magnetization in a system will transform its symmetry according to the magnetization direction. For example a cubic system will have a tetragonal effective symmetry if the magnetization is aligned along the [001] direction, and a trigonal respectively orthorhombic symmetry if the magnetization is aligned along the [111] respectively [110] direction [26].

This reduction in symmetry due to the magnetization occurs because of the spin-orbit coupling. Without spin-orbit coupling, the symmetry of a spin-polarized system would be that of the corresponding paramagnetic state. Thus it is necessary to add the spin-orbit coupling in the MOKE theory to account for the effect of ferromagnetism, and this must be done in the framework of the quantum mechanical theory. The general quantum mechanical expression for the susceptibility is given by the Kubo linear response theory, which relates χ to the expectation value (or thermal average) of retarded commutators of operators.

The following expression for the optical conductivity tensor obtained within the framework of the Kubo linear response theory [32], is general and can be evaluated for specific samples with band structure calculations (which allow explicit, although approximate evaluation of all quantities involved).

$$\sigma_{xx}(\omega) = \frac{ie^2}{m^2\hbar} \sum_{\mathbf{k}} \sum_{jj'} \frac{|\Pi_{jj'}^x|^2}{\epsilon_{jj'}} \left[\frac{1}{\omega - \epsilon_{jj'} + i\delta} + \frac{1}{\omega + \epsilon_{jj'} + i\delta} \right] \quad (2.18)$$

$$\sigma_{xy}(\omega) = \frac{ie^2}{m^2\hbar} \sum_{\mathbf{k}} \sum_{jj'} \frac{1}{\epsilon_{jj'}} \left[\frac{\Pi_{j'j}^x \Pi_{jj'}^y}{\omega - \epsilon_{jj'} + i\delta} - \frac{\Pi_{j'j}^x \Pi_{jj'}^y}{\omega + \epsilon_{jj'} + i\delta} \right] \quad (2.19)$$

where $\epsilon_{jj'}$ is the energy difference between states k_j and $k_{j'}$ in bands j and j' .

$$\epsilon_{jj'} \equiv \epsilon_{jj'}^k = (E_j^k - E_{j'}^k), \quad (2.20)$$

δ the inverse relaxation time and $\Pi_{jj'}^x$ are the matrix elements of the electronic momentum operator $p = (\hbar/i)\nabla$ between the states corresponding to E_j^k and $E_{j'}^k$.

$$\prod_{jj'}^{\lambda} = \langle \psi | P_{\lambda} | \psi \rangle. \quad (2.21)$$

The magnetically ordered state of a solid as well as the spin-orbit coupling are included in the Bloch state functions ψ and in the eigenenergies E_j obtained through

band structure calculations. Then the matrix element $\Pi_{jj'}^{\sigma}$ must be evaluated. Finally the Kerr rotation and ellipticity are obtained using Equ. 2.12.

Band structure calculations are standard [33], and the extension to spin-polarized solids is usually done using the spin density functional theory [27, 33], although other approaches exist (see for example: [28, 32, 34]). In the spin density functional theory, two separate calculations are done in parallel for the majority and minority spin systems that are coupled by a spin dependent exchange correlation potential $V_{xc}^{\uparrow\downarrow}$. This potential is conveniently treated as a perturbation to the Hamiltonian. Alternatively, a fully relativistic Dirac formalism can be used. Instead of treating the spin-orbit coupling as a perturbation, it is directly included when solving the Dirac equation. We refer to the above mentioned literature for more details on band structure calculations, the important point here being that they are used to calculate 2.18 and 2.19.

This ends the chapter on the theoretical aspects of the SMOKE. The experimental use of this method for magnetic measurements in the present work is treated in the next chapter (section 3.2).

Chapter 3

Experimental

3.1 The ultra high vacuum chamber and its measurements tools

The UHV Chamber:

Our Molecular Beam Epitaxy (MBE) experiments involve atomic scale phenomena at the interface between a clean single crystal metal surface and a second metal condensed on it from the vapor phase. To ensure ideal conditions, the presence of foreign atoms or molecular species has to be reduced to a minimum. Therefore all experiments are performed in an ultra high vacuum (UHV) chamber with a base pressure of $5 \cdot 10^{-11}$ to $1 \cdot 10^{-10}$ millibars.

The UHV chamber is equipped with standard surface analysis tools: an auger-electron spectrometer and a quadrupole mass spectrometer, plus a beetle type Scanning Tunneling Microscope (STM) described hereafter. Additionally we mounted a SMOKE measurement tool in order to measure the magnetic properties of the sample. The SMOKE setup will be described in detail in section 3.2.

The sample:

The sample stays permanently in the chamber and consists of a platinum monocrystal which is cut perpendicularly to the (111) crystallographic direction. Different metals can be deposited by evaporation on this substrate. The evaporation is made either from a Knudsen cell or from rods in an electron beam evaporator. Silver and Copper were evaporated from the Knudsen cell, whereas we used rods for cobalt and iron in the e-beam evaporator.

Before each experiment the platinum crystal was cleaned from all deposited material and from adsorbed impurities. A typical cleaning procedure consisted of several cycles comprising argon ion sputtering at a sample temperature of 800 K, oxygen exposure at 800 K ($P_{O_2} = 5 \cdot 10^{-8}$ mbar) and flash annealing to $T = 1400$ K, followed by a slow

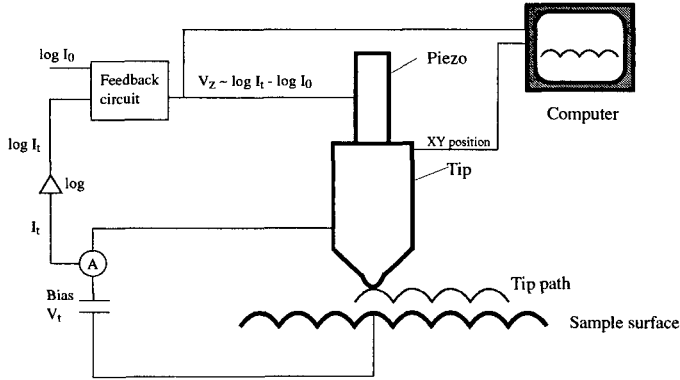


Figure 3.1: Principle of the STM (see text).

cooling (-3 K/s from 1400 K to 1200 K, -6 K/s from 1200K to 900 K and then free cooling without any sample heating). The number of cycles as well as the duration and temperature of sputtering stages depended on how much material had been deposited on the former experiment.

The Variable temperature STM:

Our main analysis tool was a home-built variable-temperature STM [35–37] which we used for the characterization of the sample as well as for the flux calibration. The STM was discovered in the eighties by Binnig *et al.* [10, 11]; they exploited the following feature: if two elements are brought close enough to each other, an overlap occurs between the electron wave functions of the two elements and electrons can tunnel from one element to the other. If a difference of voltage is applied between the two elements, a DC tunnel current in the order of nanoamperes flows between the two electrodes. If one of the two poles is a tip, we obtain a local probe for the other electrode.

The basic principle of an STM is sketched in Fig. 3.1. A sharp metal tip, in our case made of tungsten, is brought close enough to the sample for a tunnel current I_t to be established as a bias voltage is applied between the tip and the sample. In the usual constant current mode, I_t is compared to a preset constant value I_0 and the height of the tip is adjusted so that $I_t = I_0$. The tip is mounted on a piezoelectric crystal (piezo), to which a voltage proportional to $(\log I_t - \log I_0)$ is applied, allowing the tip adjustment. This applied voltage is recorded along with the lateral tip position and provides a map of the surface topography¹.

Our variable temperature STM consists of two elements: the STM itself and a manipulator that carries the sample and permits its temperature control. The sample is

¹Note that the tip height measured is not the pure topography of the sample surface. The tunnel current depends also on the density of states of the tip and sample surface.

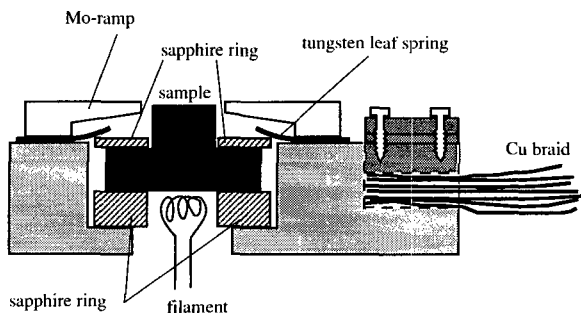


Figure 3.2: The sample holder. The temperature control is achieved by simultaneously cooling the sample with liquid helium through the Cu braid, and heating it with the filament under it.

mounted on a holder thermally coupled to a liquid helium flux cryostat. A copper braid allows thermal conductivity with a minimum mechanical vibration transfer (see Fig. 3.2). While the sample is cooled down through the copper braid, a filament placed under the sample heats it. The temperature is measured on the sample by a NiCr/Ni thermocouple, and is adjusted (to 0.01 K) by controlling the current in the filament. Heating the sample is achieved either by radiation (at low temperature) or by accelerating electrons from the filament to the sample by applying a positive voltage ($U = 400$ V) to the sample in order to obtain higher temperatures. Regulating the filament current can be done either by hand or automatically through a PID feedback. The sample temperature can vary from 30 K to over 1400 K. The manipulator on which the sample holder is fixed can be turned in order to bring the sample in front of all preparation and analysis tools in the chamber. The sample temperature can be controlled at each phase of the experiment.

The tunneling microscope is a home built beetle type STM, which is suited to study samples at varying temperatures (see Fig. 3.3). Its geometry of three supporting piezo tubes fixed to a metal head, with the center scanning piezo tube, reduces the thermal drift, since thermal contraction and expansion of the scan piezo is, to first approximation, compensated by an equal contraction and expansion of the support piezo tubes. The STM head is set down on a circular triple helix molybdenum ramp surrounding the sample. this allows the coarse approach of the tip as well as the lateral displacement by inertial motion: asymmetric triangular pulses are applied to the piezos leading to a slip-stick motion over the ramps.

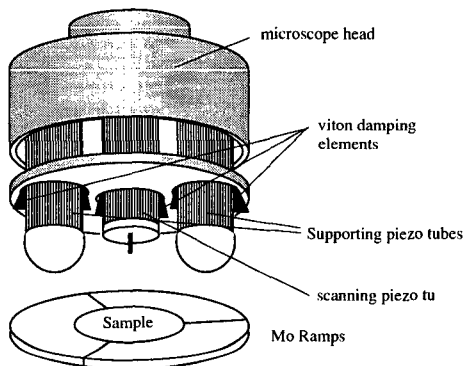


Figure 3.3: The home made beetle type STM.

3.2 The SMOKE measurement method

In conjunction with studying the topography of islands and layers of different metals on Pt(111), we wanted to measure the magnetism of these samples, in particular of thin films and islands of Co and Fe. Therefore we integrated a Surface Magneto Optical Kerr Effect setup. A SMOKE system consists of three parts: an electromagnet to apply a magnetic field to the sample, a laser source and a light detector. We designed two different sources for the magnetic field: a coil placed above the sample for polar SMOKE measurements and an iron electromagnet with its two poles on each side of the sample for transverse SMOKE measurements². The geometry of the chamber did not allow longitudinal SMOKE measurements. The lack of space in the chamber and the accessibility of the sample to the laser beam also forced us to design the vertical coil in a conical shape, and to limit its size, limiting thereby the maximum magnetic field. Fig. 3.4 sketches the SMOKE setup in our UHV chamber.

The magnets:

The vertical coil is made of kapton isolated copper wire, 1.06 mm in diameter and of roughly 27 m in lengths, for a total resistance of 0.5 ohms. It is mounted on an aluminum support held by a stainless tube that allows for water cooling³. The aluminum support has a conical opening in the middle to allow the laser beam to reach the sample. The magnetic field obtained at the sample position was measured in air, outside and inside the chamber by placing a Hall probe under the coil. Inside the chamber, the Hall probe was placed at the exact sample position. Both measurements gave exactly the same

²See Fig. 2.1 for the definitions of transverse, longitudinal and polar SMOKE.

³With $R = 0.5 \Omega$ and a current of 8 A, the coil's power is of 32 W. Without any cooling, the pressure in the UHV chamber would rise rapidly, due to the heating of the coil.

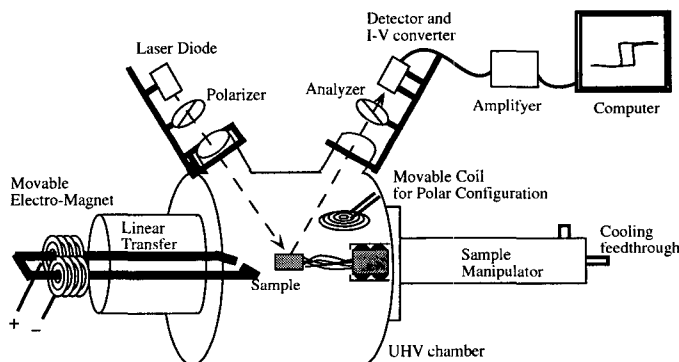


Figure 3.4: The SMOKE setup mounted to our UHV chamber. The laser beam reaches the sample at a 35 degrees from the surface normal. SMOKE measurements can be done in polar and transverse configuration.

result, although the Hall probe position was not exactly the same, which means that the exact lateral position of the probe is not critical. The measured magnetic field versus the coil current is shown on Fig. 3.5. Unlike the lateral position, the vertical position of the sample has a strong influence on the measured field: at a coil current of 6 A, lowering the Hall probe two millimeters under the base of the coil diminished the magnetic field by 10 percent.

Precise positioning of the coil and sample were achieved by the fine graduated rotational and linear transfers which allowed the placement of the sample and of the coil at reproducible measurement positions.

The magnetic field for transverse SMOKE measurements is achieved through a soft iron electromagnet with its poles inside the chamber close to the sample, and the coils located outside of the chamber. There are four independent coils made of a copper wire of one millimeter in diameter. Each coil has a length of 6.5 cm, an inner diameter of 37.5 mm, and consists of four layers of Cu wire, each of which has ~ 65 turns. The total length of the copper wire in all 4 coils is about 120. m, giving rise to a total resistance of 2.9Ω . With the maximum current available of 12 A, the magnetic field per coil is ~ 60 Gauss without the iron. The total length of the Cu wire was chosen to obtain the maximum magnetic field given our current and voltage source (the source delivers 12 A for 40 V), and given the geometry of the coils (imposed by the soft metal shape and size). We calibrated the magnetic field between the two poles of the electromagnet, at the sample position, while varying the current to reproduce the experimental conditions. Because of the hysteresis of the electromagnet, the obtained magnetic field depended not only on the electrical current, but also on the speed with which the hysteresis loops were swept. Fig. 3.6 shows the measured magnetic field at the sweep speed normally used in our experiments, 0.19 A/s . We also plotted the characteristics of the magnet when

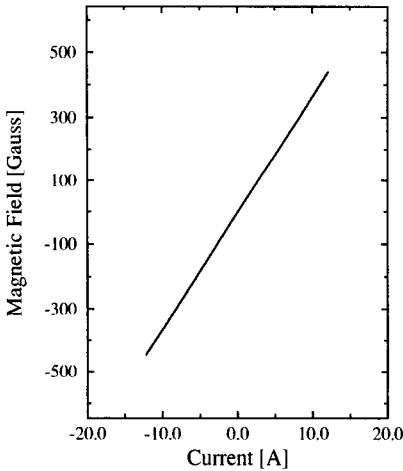


Figure 3.5: Polar setup: Magnetic field at the sample position versus the coil current. At the maximum current of 12 A we have a magnetic field of 440 Gauss.

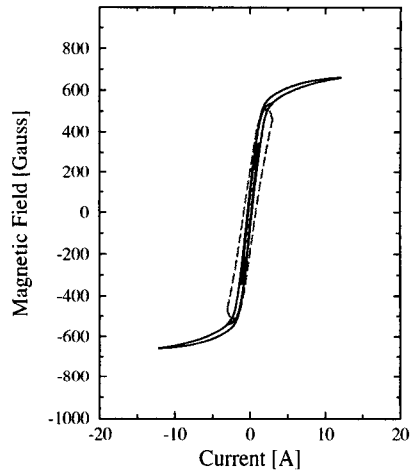


Figure 3.6: Transverse setup: Characteristics of the electromagnet. The three plain lines show the magnetic field obtained while sweeping the current at a speed of 0.19 A/S. The dashed curve shows the magnetic field obtained at the higher speed of 1.22 A/S.

varying the current faster to show how the hysteresis of the electromagnet changes.

The light source:

The polarized light source is made of a laser diode (LT 023 MD, Sharp ©, $\lambda = 780$ nm, $P_0 = 5$ mW) mounted on a head containing a Peltier element (AC-9550, Lightstar ©) which allows its temperature control to ≤ 0.1 K. The Peltier element and the laser diode are connected to a thermoelectric controller (TC 5100, Seastar Optics ©) combined with a laser diode driver (LD-2310, Seastar Optics ©). With both devices, the diode temperature and the light power output, as well as the forward current of the diode can be controlled.

A lens (Huldo 31-781 ©) used as collimator to produce a 1 mm diameter parallel light beam, is mounted directly after the laser diode, and the whole light source (diode, temperature head and lens) is fixed on an optical table which allows precise tilting and rotating of the light source (see Fig. 3.7). This table, together with a polarizer placed after the lens, is fixed on the UHV chamber through a rail, thus allowing coarse translation in three perpendicular directions: two directions in the plane of the window, and one normal to it. Translation in the plane of the window is achieved by moving the rail itself, allowing coarse displacement of the light beam. Translation in the direction

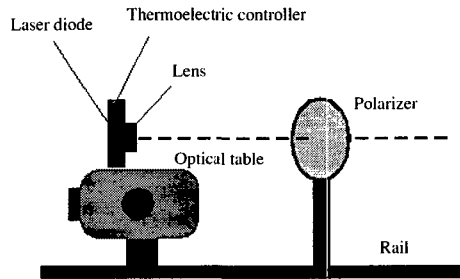


Figure 3.7: The laser diode in its temperature head and with its lens on the optical table which allows accurate focalization of the beam on the sample. The optical table and the polarizer are fixed on a rail held on the chamber which allows coarse displacement of the laser beam.

along the rail is simply achieved by sliding the different objects (polarizer and optical table) on the rail.

The detector:

After reflection on the sample, the laser beam exits the UHV chamber through another window, and is captured by a detector placed after an analyzer. The detector is made of a photodiode followed by an IV converter. The photodiode converts the light intensity into a current, which is then converted to a voltage signal. The detector is thus only sensitive to the light intensity, regardless of its polarization or its ellipticity. The role of the analyzer is to transform a polarization rotation into a change of intensity. Although it reduces the total signal by a factor of ten, placing a red filter just before the photodiode also increases the signal to noise ratio by a factor of 2. After the IV converter, the signal is amplified and filtered, and a background DC signal can be subtracted. In addition, all measurements are averaged on many hysteresis loops, improving considerably the signal to noise ratio. Fig. 3.8 shows the polar signal obtained on 1.2 ML Co/Pt(111) at 140 K before and after averaging the curves.

Window birefringence:

One undesirable side effect of the magnetic field on the polarized light is the so called window effect. By passing through the window, which is also exposed to the magnetic field, the linearly polarized light acquires an ellipticity and a rotation due to the Faraday effect. For weak signals, as those expected for submonolayers of magnetic materials, the window effect can hide the magnetic behavior. This effect can be subtracted from the measured signal by a reference measurement on a non magnetic sample under the same experimental conditions than the subsequent measurement on the magnetic sample. Fig. 3.9 shows the transverse signal before and after the window effect subtraction

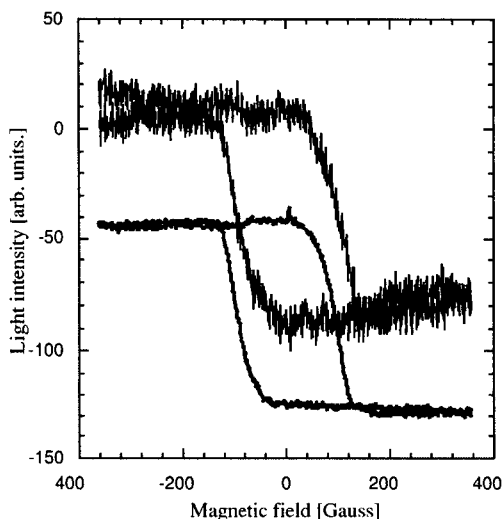


Figure 3.8: Example of noise reduction by averaging on several sweeps. This is a measurement in the polar configuration of 1.2 ML Co/Pt(111) done at a sample temperature of 140 K.

on 8 monolayers Co on Pt(111). At small coverages the orders of magnitude of the window effect and of the signal are comparable, rendering the subtraction of the window birefringence essential to the data analysis.

This subtraction method however is time consuming, especially because before subtraction, the two signals must be normalized to the light intensity measured for parallel polarizer and analyzer. As high purity windows are available which considerably reduce the Faraday effect, such windows were mounted on the chamber in a later stage. Most of the magnetic results shown in this work were measured with those windows.

Measurement procedure:

To conclude this experimental section on the SMOKE, we shall give a brief description of the measurement procedure used for the magnetic measurements. Once the sample is ready, the magnetic field is set at a fixed value (in order to magnetize the sample), the light source and the detector are adjusted to maximize the detector signal. During this phase, the polarizer and the analyzer are aligned in the same direction. The DC signal obtained is noted, and will be used in normalizing the forthcoming measurement⁴. Then the polarizer and analyzer are set at right angle to each other so that the detected signal

⁴Note that when heating or cooling the sample between two measurements, this DC signal was subject to changes, and was therefore remeasured. The DC signal also tended to drift with time, rendering long measurements unreliable.

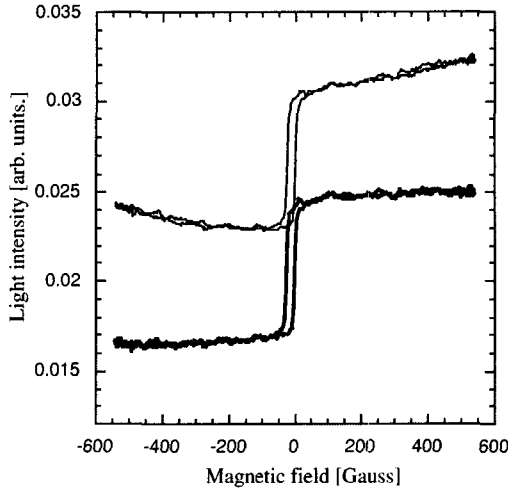


Figure 3.9: Transverse SMOKE signal of 8 ML Co deposited on Pt(111) at 350 K. The thin line is the signal before correction of the window effect, and the bold line after this correction.

almost vanishes. This way, the ratio between the change of light intensity measured while changing the magnetization and the DC background signal is more favorable.

The signal is amplified twice: first at the IV converter, and second after the removal of the background DC signal. Sweeps of the magnetic field are then started, and the resulting signal is recorded (with the 16 bits ADG's and the computer setup which is also used for the STM measurements), *before averaging several sweeps together*.

Chapter 4

Nucleation and growth of Ag and Cu on the Pt(111) substrate

This chapter deals with nucleation and film growth of Ag and Cu on the homogeneous and isotropic substrate Pt(111). After a brief introduction to nucleation theory, we present STM results on strain relief in these heteroepitaxial layers. We will focus on strain relief at island edges and on the regular dislocation and moiré patterns forming in continuous Ag and Cu films on Pt(111). Out of the various partly metastable strain relief patterns, the periodic ones receive particular attention as they serve as templates to grow regularly spaced and equally sized islands (see chapter 5)

4.1 Introduction to nucleation theory

The present and next chapters deal with two-dimensional islands and with mono- and multilayer films grown on a metallic substrate. These islands and layers are created by molecular beam epitaxy and their formation takes place through nucleation and growth processes. Since the morphology critically depends on the interplay of these processes, we will give a concise description of them.

In molecular beam epitaxy, atoms are evaporated with the flux F onto a substrate, where, after adsorption, different diffusion processes occur with well defined rates. Depending on the elements involved (substrate and deposit) and on the substrate temperature, each atom may either stick wherever it lands (statistical growth), reevaporate (incomplete condensation), diffuse on the surface, combine with another atom to form a dimer, or bury itself into the substrate. For net growth to occur, the system must be out of equilibrium, *i.e.* more atoms must stay on the surface than reevaporate.

Each condensed atom will diffuse randomly until it meets a location where the binding energy is big enough to capture the atom in a stable way¹. The capture of an

¹By stable we understand that other atoms will stick to the captured atom before it escapes, so that the growth of the cluster is faster than its decay.

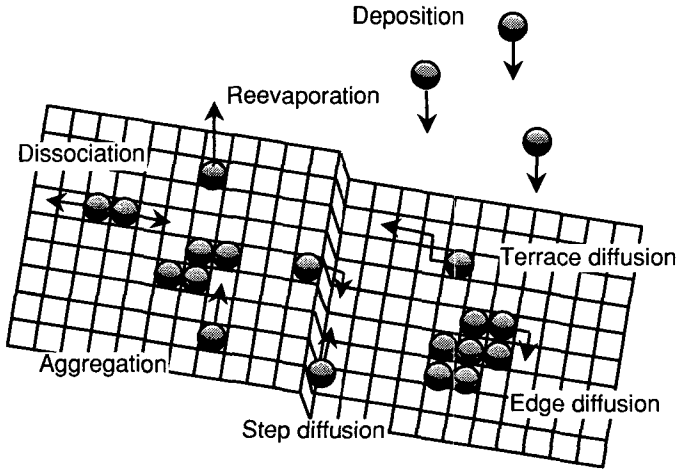


Figure 4.1: Some of the processes involved in molecular beam epitaxy.

atom can be achieved by any irregularity of the surface, for instance a step, a dislocation, an impurity a vacancy, etc . . . or by another diffusing adatom. In this last case, a dimer is formed, which will grow into a bigger island as other atoms attach to the cluster. Depending on the temperature, a formed island can dissociate or atoms can diffuse along an existing island or along a step. Atoms can also climb up or down steps or existing islands, and dimers or bigger islands might diffuse. Some of these processes are sketched in Fig. 4.1.

In a basic approach, the situation can be simplified. First, complete condensation (*i.e.* no reevaporation processes occurs) can be assumed (in our case of metal/metal epitaxy, this assumption is justified since $E_a \approx 2\text{eV}$ $ggK_B T$). Second, dissociation and island diffusion can be ruled out since at the temperatures involved in our experiments, dimers turn out to be stable and immobile. Third, we haven't considered edge diffusion nor the climbing of atoms up and down steps since we are mostly interested in island densities and size-distributions and not in island shapes. Similarly, the burying of the adatom into the substrate, or alloy formation, is not considered in the following introduction to nucleation theory. Finally we assume *homogeneous and isotropic substrates*, *i.e.* surfaces without any irregularities such as impurities or dislocations, so that the only possible trap for a diffusing adatom is another diffusing atom or a stable nucleus. This is naturally not true in real experiments. It is possible, however, to work under sufficiently clean conditions, and with sufficiently well prepared substrates, so that the impurity density is much smaller than the cluster density. One can further select large terraces for the STM investigation and thereby reduce the influence of steps. Therefore the experiments to be reported below do actually come quite close to the ideal situation of a defect free substrate.

The above simplifications being accepted, it is interesting to focus on the island density evolution during deposition. The four following stages can be distinguished: the pure nucleation stage, the nucleation plus island growth stage, the pure island growth stage and finally the coalescence stage. At the beginning of deposition, the monomer density is low and the chances are much greater for an atom landing on the surface to find another atom than one of the very few dimers that have already formed. Thus a dimer is formed for every two atoms and the dimer, respectively island density grows linearly in time. This is the pure nucleation stage. Then, as the island density increases, more and more atoms will meet an island instead of a new atom. This is an intermediate stage, where the existing islands grow bigger, and new islands are still forming. The third stage happens when the average distance between two existing islands corresponds to the mean free path of the diffusing atoms. At this point, each atom landing on the surface will meet an island: This is the pure growth stage, where the island density remains constant. Obviously, this saturation island density is directly related to the diffusivity of the atoms. The exact relationship between these two quantities is given below. Finally, the last stage happens when islands start to coalesce, leading to a decrease of the island density. Eventually the island density drops to zero as all islands connect together to form a continuous film.

In the mean-field nucleation theory [6,38,39], this island formation is described by a set of coupled rate equations which describe the evolution of the density of monomers and stable clusters with time. Equations (4.1) and (4.2) show the rate equations in the case of complete condensation and stable dimers.

$$\frac{dn_1}{dt} = F - 2\sigma_1 D n_1^2 - \sigma_x D n_1 n_x - F(t - n_1) - 2F n_1 \quad (4.1)$$

$$\frac{dn_x}{dt} = \sigma_1 D n_1^2 + F n_1 \quad (4.2)$$

In these equations, n_1 and n_x stand for the density of atoms, respectively stable clusters, in atoms (clusters) number per lattice site. F is the flux of atoms arriving from the gas phase on the surface, in units of atoms per lattice site. D is the terrace diffusion coefficient describing the mean square displacement of an adatom, and σ_1 and σ_x are the capture rates of monomers, respectively stable clusters of any size x . Coalescence is not considered in these equations.

The first term on the right hand side of equation (4.1) stands for the increase of monomers due to atom deposition with flux F . The second and third terms denote the decrease of monomers due to the formation of dimers, respectively, due to the capture of a diffusing atom by a stable cluster. The last two terms describe the decrease of monomers due to direct impingement onto stable islands and monomers, respectively. In equation (4.2), the first term on the right hand side stands for the increase of stable clusters due to the event of two atoms meeting each other and forming a stable dimer. The second right-hand term stands for the formation of such dimers due to

direct impingement onto a monomer. The integration of these coupled differential equations yields the density of stable islands as a function of time, respectively coverage; it equally gives a relationship between the maximum (saturation) island density and the diffusion coefficient.

This island density evolution can be monitored in VT-STM nucleation experiments and Fig. 4.2 shows that it is well described by the mean field nucleation theory. The plot shows the island density evolution up to the saturation stage, leaving out the decay part. In the inset we show a Kinetic Monte-Carlo (KMC) simulation of the island density, including its decays to zero [40].

In the more general case of larger stable clusters, this integration yields the following expression for the maximum island density:

$$n_x = \eta(\Theta, i) \left(\frac{D}{F}\right)^{-\chi} \exp\left(\frac{E_i}{(i+2)kT}\right) \quad (4.3)$$

where $\chi = \frac{i}{i+2}$ is the scaling exponent and i is the critical cluster size (corresponding to the limit between stable and unstable clusters. If $i = 1$, the dimer is stable) and E_i its binding energy. In the simple case considered here, where $i = 1$, $E_1 = 0$ and equation (4.3) reduces to $n_x \propto (\frac{D}{F})^{-1/3}$. The diffusion coefficient (in lattice sites per second) can be expressed as

$$D = \frac{1}{2d} \nu_0 \exp\left(\frac{-E_m}{k_B T}\right), \quad (4.4)$$

where d is the dimension of the motion, ν_0 is the attempt frequency and E_m is the energy barrier for a diffusing atom to hop from one atomic site to another. With Eqs. 4.3 and 4.4, we can extract a precise value for E_m and ν_0 through an Arrhenius plot of the saturation island density.

An example of an island density Arrhenius plot obtained for Ag growth on Pt(111) is shown in Fig. 4.3. The simple development above describes only the linear part of the plot. The deviation seen at very low temperatures comes from the fact that at low temperatures, the diffusivity is so small that a considerable amount of the deposited atoms is still present as isolated monomers when the deposition flux is stopped. The formation of new dimers and the cluster growth occurring after the deposition flux is stopped are named the *postnucleation* and *postgrowth*. They can be introduced in the scaling theory in order to reproduce the experimental curve in the whole range of temperature². The *postnucleation* and *postgrowth* effects come from the fact that at very low temperatures many monomers are still diffusing on the substrate after the deposition flux has been stopped. These diffusing adatoms will form new dimers or attach to existing islands in the absence of an incoming flux.

Coming back to island formation, we emphasize that randomness rules almost all processes involved. Atoms land randomly in time and space on the surface, then they

²Note that the relevant parameter is not the temperature, but the ratio between the diffusivity D and the flux F . The temperature can be used as a parameter to vary D . *Postnucleation* and *postgrowth* effects play a role only when $\frac{D}{F} < 10^5$.

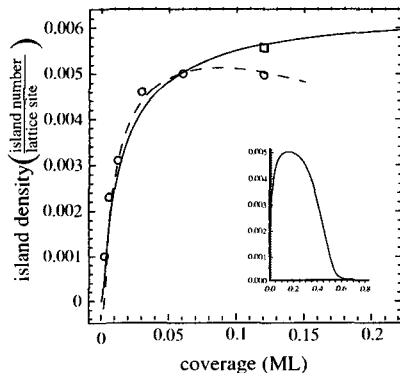


Figure 4.2: Island density versus coverage for Ag grown on Pt(111) at 75 K [40]. The round symbols are the experimental data. The plain curve corresponds to the mean-field nucleation theory (which does not consider coalescence) and the dashed line is a guide to the eye. We see that for this system, the saturation island density is reached for a coverage over 0.06 ML. At 0.12 ML islands already start to merge and the island density is slightly smaller than at 0.06 ML. The square symbol is the experimental island density that would have been obtained without coalescence. This value was inferred by differentiation of coalesced islands from the others through their shape. The inset shows the typical shape of the island density curve up to a coverage leading to a continuous film.

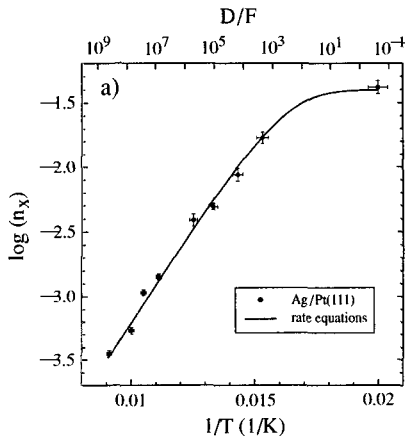


Figure 4.3: Arrhenius plot of saturation island densities ($\Theta = 0.12\text{ML}$) for Ag/Pt(111). For this system and at these temperatures, dimers are stable. The breaking of the slope for very low temperature is due to the *post-nucleation* and *postgrowth* effects (see text). From [41].

diffuse into random directions at random instants until they meet another atom and form an island. The result is a set of islands randomly dispersed on the surface with a wide size distribution, as can be seen in Fig. 4.4 which shows an example of Ag nucleation on Pt(111) at 95 K.

For many purposes it is desired to have control on the island shape or size, or on the



Figure 4.4: Example of random nucleation on an homogeneous substrate. Ag deposited on Pt(111) at 95 K with $F = 1.1 \cdot 10^{-3}$ ML/s

island's spatial distribution. For example, it is interesting to control the shape and size of the islands in order to study physical properties of small clusters. Perfect control of small islands shape is already obtained by moving atoms one by one with an STM tip. But this is time consuming, and works only for a little number of clusters. We want to focus on the possibility to control nucleation processes at a larger scale, on billions of islands simultaneously.

One possibility to influence the nucleation process is the use of anisotropic or inhomogeneous substrates. For instance, stepped surfaces can be used to obtain elongated islands of a few atoms in width [42–45]. Another example is the nucleation of Ni on the herringbone reconstruction of gold(111), which presents some regularity due to the preferential site for exchange in one of the two elbows of the gold reconstruction [46,47]. The presence of impurities on the substrate may trap the diffusing adatoms [48,49] or act as repulsive spots [50,51], changing significantly island densities, but not island spatial distribution since impurities are randomly dispersed on the substrate. In Fig. 4.5, we compare Ag nucleation on a pure Pt substrate with Ag nucleation on a Pt substrate containing impurities. A well defined density of impurities was introduced in the substrate by evaporating a small quantity of Ag at elevated temperature, so that Ag adatoms bury into the first Ag layer. We see that for a given temperature, the more impurities are introduced, the higher the saturation island density. In other words, the introduction of repulsive impurities on the substrate decreases the mean free path of diffusing adatoms.

By comparison with impurities, surface dislocations are interesting because they often arrange themselves in a regular way. Furthermore, they are often present in heteroepitaxy, providing a quite general tool to control nucleation in many systems. Generally, surface dislocations strongly influence nucleation island densities by changing the barrier energy for diffusing atoms. [52–54]. In many cases they represent repulsive barriers for adatoms diffusing on the surface. This has, for example, been shown for Al/Au(111) [55]. It is also corroborated by Effective Medium Theory (EMT) calculation performed for Pt/Pt(111) [56]. Before showing in the next chapter how a dislocated substrate can not only change the island density but also narrow the size and spatial distribution of deposited islands, we shall explain how surfaces with a regular network of dislocations are created.

4.2 Strain relief at hexagonally close-packed surfaces

Patterned substrates form because systems try to relieve the surface strain by reconstructing the atomic layer at the surface in a different manner than internal layers in the crystal. Some elements show spontaneous surface reconstruction for certain crystallographic directions, due to lower coordination number of surface atoms than that of bulk atoms which induces tensile surface stress. Examples of close-packed surfaces

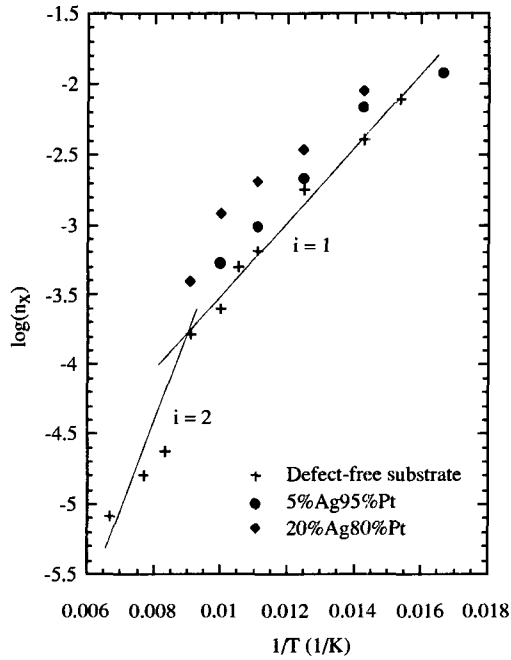


Figure 4.5: Comparison of the island densities obtained on clean Pt(111) substrate and on substrates containing 5%, respectively 20% of repulsive impurities. The breaking of the line at high temperature in the defect-free nucleation curve is an effect of the change of critical cluster size: above 110 K, dimers are not stable anymore.

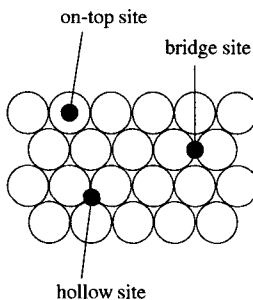


Figure 4.6: Definition of the different adatom adsorption sites

that reconstruct are Au(111) [57] and Pt(111) [49,58]. However, most materials find it energetically more favorable to keep their bulk structure at the surface. A more general case leading to dislocation is that of heteroepitaxy, i.e. growth on a substrate of different material than the adsorbate.

The deposition of one metal on another leads to strain in the surface due to lattice mismatch between the two materials. Basically there are three possibilities for the system to deal with this stress. The first one occurs when the substrate-adlayer interaction is much stronger than the atom-atom interaction in the adlayer: the adlayer adopts the lattice spacing of the substrate, the layer grows isotropically strained and is said to be commensurate. Opposite to this scenario, when the lateral interactions between film atoms are very strong with respect to the corrugation of the adlayer-substrate potential, allowing little displacement of the adlayer atoms with respect to their preferred inter-spacing, the layer grows incommensurate. All the strain occurs then at the interface between the two materials, and the layer presents a moiré structure which is a long range undulation due to the periodic change of adatom adsorption position among the different possible sites of the substrate: “hollow”, “bridge” and “top” sites (see Fig. 4.6). The last case of strain relief is the intermediate situation, when both (substrate-layer and intralayer) interactions are of comparable strengths. Then the system will minimize the energy by placing most atoms in pseudomorphic hollow sites, and relieving the surface strain within a few atoms placed on unfavorable sites (top and bridge sites). These atoms form the so called partial surface dislocations, or misfit dislocations.

Naturally, misfit dislocation formation costs energy, and they appear only when the energy cost of growing n strained layers is larger than forming misfit dislocations. For close-packed metal-metal overlayer systems, it is easier to form misfit dislocations (than for square systems for example), because there are two almost equivalent sites which are energetically favorable for an adatom sitting on the substrate. Namely the fcc and hcp site, corresponding respectively to ABCABC and ABCABA stacking. Hence the system can form dislocations by introducing a stacking fault: surface dislocations separate domains of different stacking.

There are two types of misfit dislocations, sketched in Fig. 4.7: if the strain is

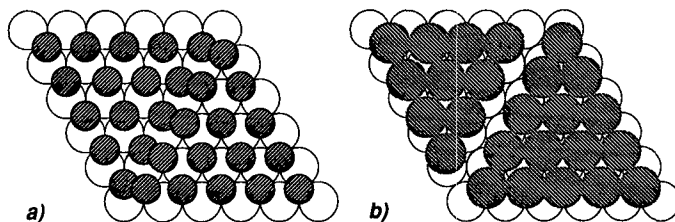


Figure 4.7: High and low density partial dislocations. The displacement of atoms with respect to the substrate may extend onto several atoms on each side of the dislocation.

compressive, *i.e.* if the adlayer has a larger lattice spacing than the substrate, the partial dislocation lacks half an atom and therefore reduces the density. The partial dislocation is a low density one. In the opposite case, if the strain is tensile, one atom of the adlayer will sit on an unfavorable site between the two stacking domains resulting in a locally higher density at the partial dislocation. Because hcp and fcc sites are not strictly equivalent, reconstructed surfaces present usually a larger area of fcc stacking than that of hcp stacking, as demonstrated for 2MLAg/Pt(111) [59], the reconstructed surface of Au(111) [60] and that of Pt(111) [54, 61].

The patterns formed by the surface dislocations depend on how the dislocation lines arrange themselves. This is largely determined by the following constraints. On the first hand, a dislocation line relieves strain in only one direction, namely the direction perpendicular to it. Therefore, in order to relieve strain isotropically, the system must form dislocation lines in all possible directions (three in the case of hcp(111) surfaces shown in Fig. 4.7). On the other hand, crossing of dislocations costs energy since it implies regions with very high or very low atom densities at the crossing points. Hence, many systems avoid dislocation crossing, forming mesoscopic domains in which the strain is anisotropically relieved, the strain being relieved isotropically at a macroscopic scale. (See Fig. 4.16 a) for an example of these striped reconstructions). An other important feature in determining the overall appearance of a dislocated substrate, is the long-range repulsive interaction between dislocations. This tends to make the interspacing between them constant.

During multilayer deposition, a given system may go through all three configurations, from pseudomorph to moiré. Generally the first monolayer grows pseudomorphic with respect to the substrate; as more material is deposited, the energy cost for the overlayers to grow pseudomorphic becomes bigger than the energy cost involved in forming dislocations, and dislocations appear in order to relieve the strain. As the film thickness increases, the film will progressively adopt its bulk structure. The dislocations will disappear and be replaced by a moiré, the undulation of which is the signature of the substrate underlayer. The corrugation of this moiré pattern decreases as the film thickness increases, until a flat single crystal of the film appears.

Stable configuration versus number of deposited monolayers has been calculated by

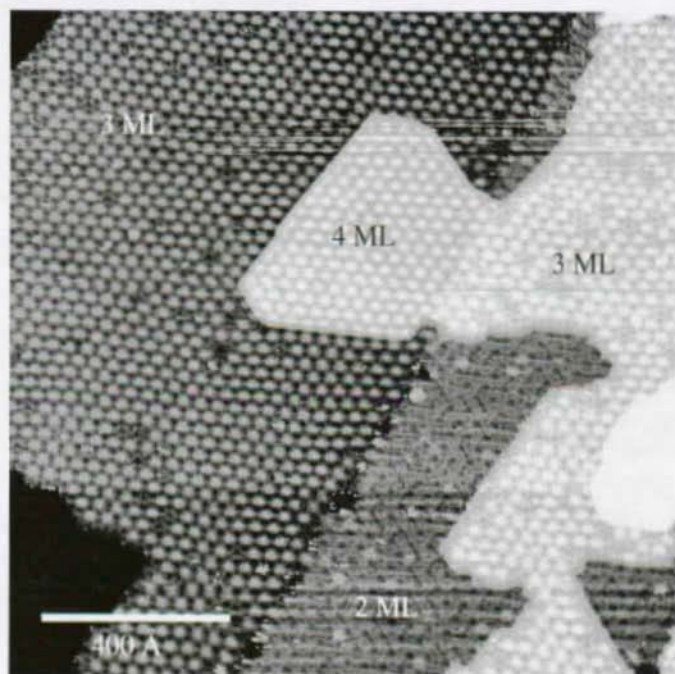


Figure 4.8: STM image of 3ML Cu on Pt(111). Labels on the image indicates how many Cu monolayers are locally deposited. The first monolayer (not shown) grows pseudomorph. The second monolayer contain partial dislocations that relieve extensive stress, whereas the third and upper layers have moiré structures.

J. C. Hamilton and S. M. Foiles for Cu on Ru(0001) [62]. They showed that this sequence of structure (from pseudomorphic to moiré) is a general feature, valid for a wide range of overlayer systems where the adatoms are smaller than the substrate atoms. We will see in detail how this sequence applies for two systems, Ag/Pt(111) [63] and Cu/Pt(111). Ag has a larger lattice constant than Pt, whereas Cu is smaller than Pt. However, the sequence is valid for both systems, as will be shown in section 4.2.2.

4.2.1 Cu growth on Pt(111)

The lattice constant of Cu is 7.88% smaller than that of Pt and STM images of Cu overlayers on Pt(111) grown at room temperatures show several surstructures from pseudomorphic layer to moiré structures. This is shown in Figs. 4.8 and 4.9 where respectively three and one and an half monolayers have been deposited on Pt(111). The first monolayer grows pseudomorphic to the Pt(111) substrate. As the second ML is

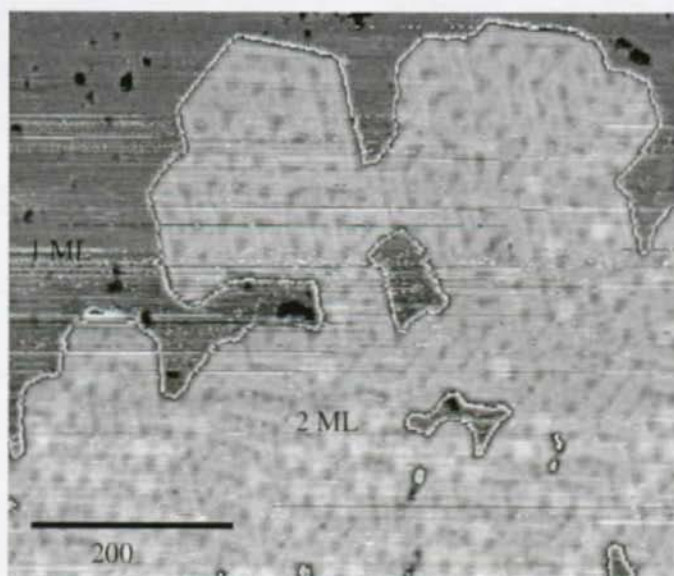


Figure 4.9: 1.5ML Cu on Pt(111). The second monolayer is reconstructed whereas the first one is pseudomorph

deposited, misfit dislocations appear to relieve the strain. These dislocations disappear in the third ML, which present a moiré reconstruction to which we will come back later.

The second monolayer deserves a little more attention since it shows two energetically degenerated reconstructions. The first of these reconstructions, shown in Fig. 4.10, is formed by three sets of parallel high density partial dislocations crossing each other at an angle of 120° and relieving stress in all three directions. At each crossing point of three dislocations, a bright knot with a dark center is present. This knot is a reordering of Cu atoms in the crossing area in order to avoid the unfavorable on-top site at the crossing point. The dislocation network has a trigonal symmetry³ and a periodicity of $35 \pm 5 \text{ \AA}$, corresponding to 12 to 13 Pt atoms⁴. The unit cell of this pattern consists of a quasi-parallelogram separated in two by a dislocation line and with a knot at one angle. The two parts of the quasi-parallelogram have slightly different sizes, the bigger one being probably the fcc stacking area, whereas the other is the hcp stacking area. The inset of Fig. 4.10 shows the bigger cell which forms a quasi-hexagon and which includes three unit-cells.

³The alternation of fcc and hcp areas transforms the hexagonal symmetry into a trigonal one.

⁴Assuming that the strain is relieved by placing $N+1$ Cu atoms on N Pt atoms, a pure geometric argument predicts the periodicity of the network to be of 11 to 12 Pt atoms.

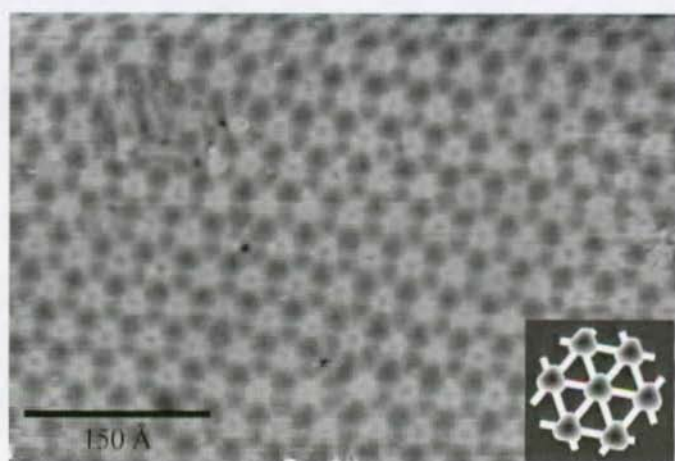


Figure 4.10: STM image of the trigonal dislocation network of 2ML Cu on Pt(111). The partial dislocations are bright whereas the dark parts are hcp and fcc stacking areas. Note that the fcc and hcp parts around each node have slightly different sizes, the larger ones being probably the fcc stacking areas. The inset shows three unit cells forming the larger hexagons.

Fig. 4.11 shows a ball model of the trigonal network. The bright knots involve the displacement of several rows of Cu atoms out of the fcc or hcp sites. The exact number and position of Cu atom displaced is not visible on the STM image. Likewise the width of the partial dislocations is not known. The ball model only shows qualitatively how the dislocation pattern appears, and suggests a solution to reproduce the experimental periodicity corresponding of 11 Pt atoms, on which 12 Cu atoms sit. We assumed the center of each knot to be filled with fcc Cu atoms, and the dislocations lines to be only two Cu atoms in width. Around each fcc center of the node, all atoms are slightly displaced, forming a circle of higher density, which appears bright in the STM image.

The other reconstruction of the second monolayer is a labyrinth-like dislocation pattern, where the partial dislocations avoid crossing each other and where the mean dislocation interspacing is 20 ± 5 Å. Fig. 4.12 shows an STM image of this labyrinth pattern. Both configurations relieve strain effectively in all three directions. These two reconstructions have been observed without significant preference for one or the other, sometimes both coexisted on the same terrace, as in Fig. 4.13. Since the coexistence prevailed at higher deposition temperatures (up to 400 K), we conclude that both structures are energetically degenerated.

From the third monolayer on, the pattern switches to a moiré, which is recognizable by its very long range order; the periodic undulation keeps its phase even over steps. In the fourth, fifth and sixth monolayers, the moiré is defect free. The periodicity and corrugation of the moiré remain constant within the error bars, being 35 ± 2 Å and

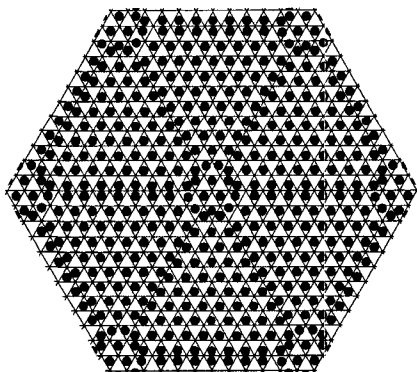


Figure 4.11: Ball model of the trigonal dislocation pattern of 2MLCu/Pt(111). The black dots represent the Cu atoms and the underlying Pt substrate is represented by the hexagonal line pattern, each Pt atom being at the intersection of three lines. The up- and down-triangles represent the hcp respectively the fcc sites. For the sake of simplicity, only one Cu layer is drawn. We assumed the center of the nodes to be occupied by fcc Cu atoms. The periodicity is 11 Pt atoms and 12 Cu atoms.

approximately 0.4 \AA respectively. This is compatible with a ball model, where the difference in height of a Co atom at on-top site and a Co atom at hollow, respectively bridge site would be of 0.7 \AA , respectively 0.5 \AA . The convolution of the STM tip with the substrate can explain that we measure a little less corrugation. Fig. 4.14 shows the moiré of the fourth monolayer Cu/Pt(111).

In the third monolayer however the moiré contains some triangular reconstructions as shown in Fig. 4.15. These triangles are very similar to the ones observed in the first monolayer of Au/Ni(111) [64] and that of Ag/Cu(111) [65]. The triangles in these systems are due to partial dislocation loops in the uppermost substrate layer associated with a removal of substrate atoms which migrate into the overlayer or onto its surface. The substrate surface reconstructs in a regular pattern of triangular dislocation loops, the inner part of which are hcp stacking areas. Jacobsen *et al.* [64] showed that in spite of the large amount of energy involved in forming the partial dislocation loops and the hcp regions, the triangular structure is energetically almost identical to the moiré structure. The reason for this is that the fcc to hcp shift of the underlying atoms in the triangular areas makes it possible for those overlayer atoms which would be on on-top sites in a moiré to coordinate to three atoms underneath rather than to one. Our system differs from those two examples in that the triangular pattern appears in the third monolayer Cu instead of the first overlayer Ag or Au as in the two examples above. This implies that the triangular partial dislocations form in the second monolayer Cu instead of in the substrate. This also means that the atoms removed from the second monolayer

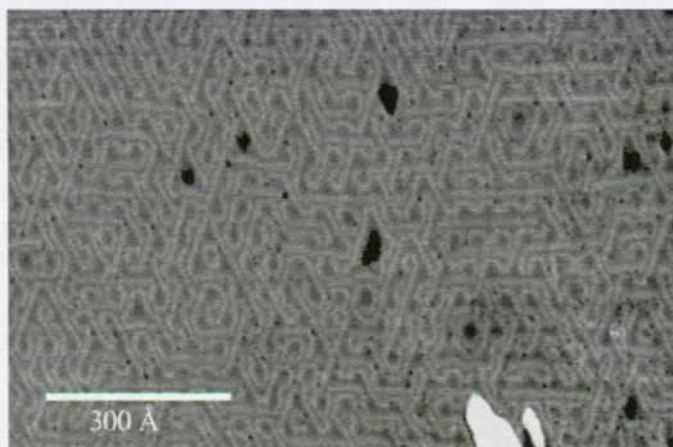


Figure 4.12: STM image of the labyrinth-like pattern formed by the second monolayer of Cu on Pt(111). The system relieves strain in all three directions without crossing dislocations.

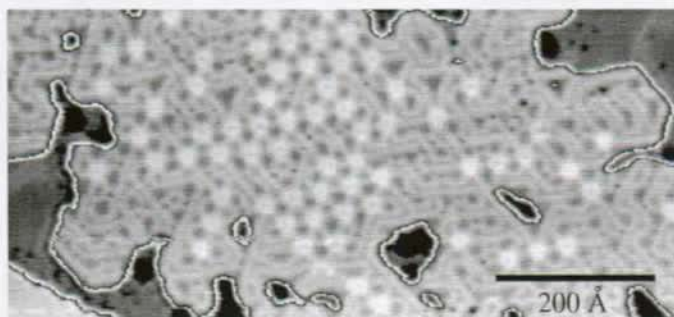


Figure 4.13: The two coexisting strain relief patterns (labyrinth and trigonal) of the second monolayer of Cu on Pt(111). The presence of both reconstructions on the same terraces and at a deposition temperature of 350 K indicates that they are nearly energetically equivalent.

can more easily be incorporated in the third monolayer, since no 2D alloy formation is necessary. In 3MLCu/Pt(111), the coexistence of moiré and triangles indicates that these two configurations are almost equivalent in energy, just as calculated in Au/Ni(111) and Ag/Cu(111).

To conclude, Cu growth on Pt(111) is a good illustration of heteroepitaxial growth, where the different phases (pseudomorph, dislocated, moiré) follow each other according to the predictions made by considering the competition between intralayer and substrate-layer interactions and the energy cost of each configurations as a function of film thickness. We will see in the next section that in the case of Ag/Pt(111), this

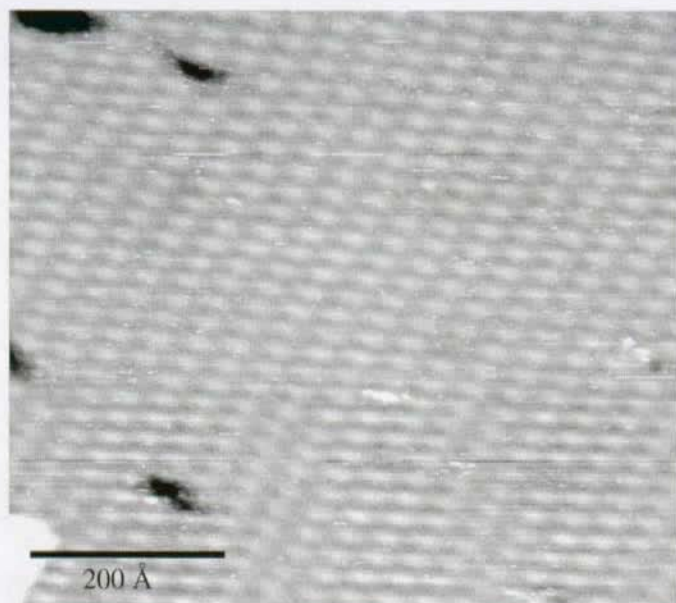


Figure 4.14: Moiré of the fourth monolayer Cu on Pt(111)

succession in structures is not strictly followed.

4.2.2 Ag growth on Pt(111)

Contrary to the Cu/Pt(111) case, the system Ag/Pt(111) doesn't strictly follow the pseudomorphic, through dislocated, to moiré sequence. The pseudomorphic stage occurs for submonolayer deposition, when islands are smaller than 200 Å. Dislocations appear in islands larger than 200 Å in diameter but then disappear again as the first monolayer is completed, to reappear in the second monolayer.

The disappearance of dislocations at the first monolayer completion is due to the 2D adatom gas present on top of the adlayer once it is completed [63]. This was demonstrated by growing Ag islands on the first ML before it is completed. This was done by two deposition steps. One at 300 K to prepare the large 2D islands, and one at low temperature to generate second layer islands on top of some of the first layer islands. In these experiments we clearly saw that dislocations disappear only in those monolayer islands that were covered by second layer islands. This demonstrates that it is the presence of the 2D adatom gas on top of the adlayer rather than the layer completion that is determinant in lifting the dislocations.

The effect here is opposite to the reconstruction of Pt(111), which can be induced by a two dimensional Pt gas on its surface [54]. Here the two dimensional Ag gas leads to

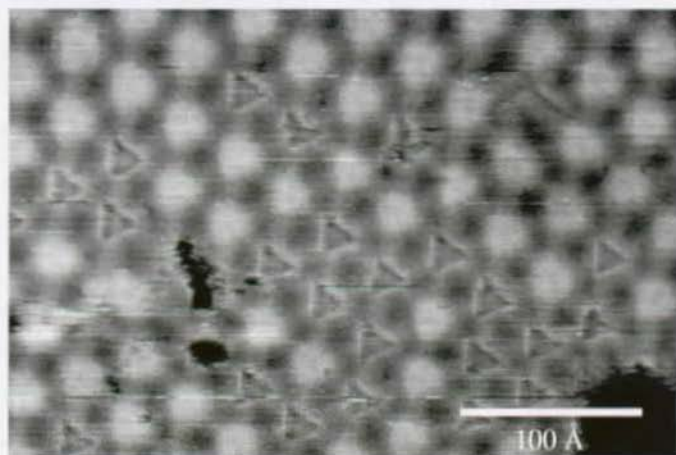


Figure 4.15: Moiré of the third monolayer of Cu on Pt(111). The triangles appear only in the third monolayer and are believed to be due to partial dislocation loops in the underlayer.

the disappearance of the dislocation pattern. On Pt(111), the pseudomorphic surface, being under tensile stress, tends to incorporate atoms. The 2D adatom gas facilitates this incorporation, and the reconstruction results of a surface laying on a layer which contains less atoms than the overlayer. In Ag/Pt(111), the Ag layer is under compressive stress, since silver has a bigger lattice constant than platinum. Surface dislocations (which in this case result from the lack of half an atom) appear in order to remove this stress. If an adatom gas is present on the surface, there are two possible scenarios: either the adatoms are incorporated into the layer, increasing strain but gaining in coordination, or the adatoms are left on top. In the present case, the incorporation is more favorable and the reconstruction is lifted.

With the exception of the dislocations disappearing on the completed first monolayer, Ag/Pt(111) respects the pseudomorphic-dislocated-moiré sequence with increasing film thickness. Fig. 4.16 shows STM images of 0.8 ML, 1.6 ML, 3 ML and 10 ML Ag/Pt(111). In the first images, the striped dislocation pattern of the first ML before completion is shown. For 1.6 ML, the reconstruction of the second ML is visible, together with the first ML in which all dislocations have been lifted. Again, as in the former case of 2MLCu/Pt(111), the second monolayer of Ag on Pt(111) has two different reconstructions. In this case however, both are energetically different. A striped reconstruction, which forms during deposition at room temperature is metastable and turns into a trigonal reconstruction when annealed at 800 K. Both reconstructions, before and after annealing are shown in Fig 4.16 b) and c). The trigonal reconstruction will be described in more detail in section 5.1.

Fig. 4.16 d) shows the third ML of Ag/Pt(111). The strain relief pattern of both layers is quite different than the equilibrium dislocation pattern of the second ML. The

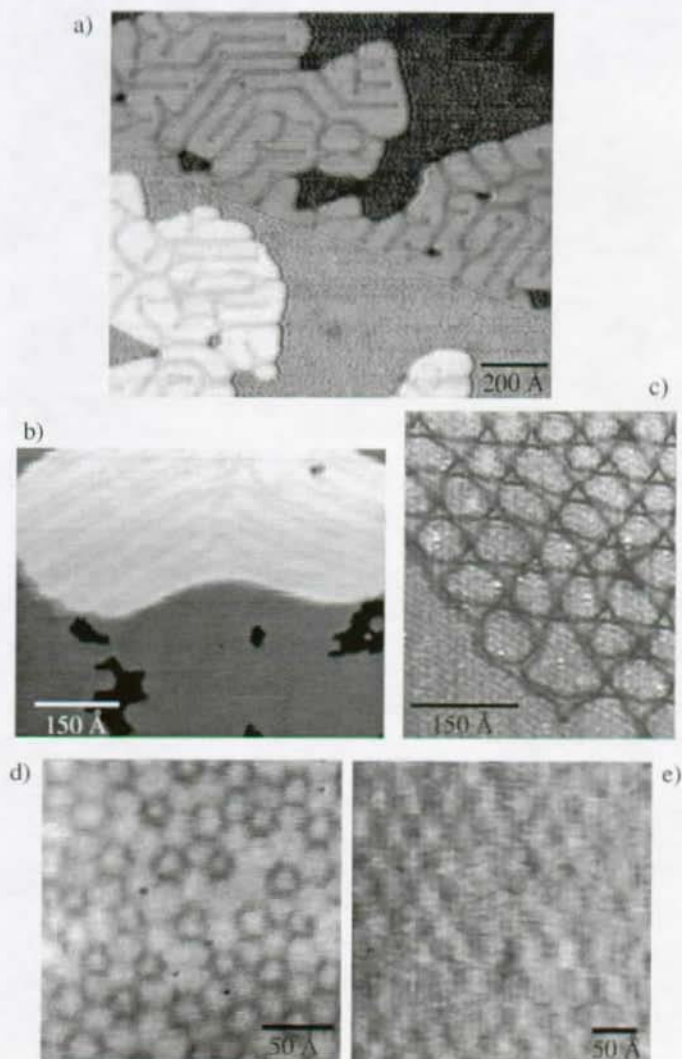


Figure 4.16: Ag grown on Pt(111). a) 0.8MLAg/Pt(111); room temperature deposition. The striped dislocation pattern is seen on the first Ag ML. b) and c): 1.6 ML Ag/Pt(111) before and after annealing at 800 K. In the first ML, the dislocations are lifted. d) 3 ML Ag/Pt(111), room temperature deposition. This dislocation pattern progressively attenuates to form a moiré structure still visible at 10 ML e).

periodic structure, resembling the regular reconstruction seen on 2MLCu/Pt(111), is made of protruding areas surrounded by darker lines hexagonally arranged and connected between them by partial dislocation lines. The transitions are much smoother than for 2ML, and the pattern comes close to a moiré. This periodic superstructure persists over several ML. The corrugation decreases and transforms progressively to a moiré upon increasing film thickness. At 10 ML (Fig. 4.16 e), the moiré corrugation is still visible, although very weak.

After the study of multilayer Ag/Pt(111) reconstructions, we focused on the submonolayer stage of the same system. In particular, the appearance of dislocations in the submonolayer Ag/Pt(111) was studied in details. A surprising feature with this system is the unusually large imbalance between fcc and hcp stacking areas. For a Ag adatom on Pt(111), there is a tiny difference in binding energy between hcp and fcc sites. This difference cannot explain why fcc domains are more than three times wider than hcp domains. Light can be shed on this fact by modeling the dislocation structure through a 2D Frenkel-Kontorova model. In this model, nearest-neighbor atoms are connected by springs and sit in a corrugated substrate potential. It has been successfully applied to Au(111) [61] and Cu/Ru(0001) [62] where it reproduced experimental results (fcc domains twice as wide as hcp domains). For our case of Ag on Pt(111), the substrate-overlayer interaction is modeled through a corrugated 2D substrate potential of the form:

$$\begin{aligned}
 V_{Pt-Ag}(\vec{r}) = & V_0 + V_1 \sum_{\vec{G} \in G_1} \cos(\vec{G} \cdot \vec{r}) \\
 & + V_2 \sum_{\vec{G} \in G_1} \sin(\vec{G} \cdot \vec{r}) \\
 & + V_3 \sum_{\vec{G} \in G_2} \cos(\vec{G} \cdot \vec{r}), \quad (4.5)
 \end{aligned}$$

where G_1 is a set of three reciprocal lattice vectors of length $4\pi/\sqrt{3}a$, one along the x axis (crystallographic $\langle 1\bar{1}0 \rangle$ direction) and the other two oriented at $\pm 120^\circ$ with respect to the x axis; G_2 is a set of three reciprocal lattice vectors of length $4\pi/a$, along the y axis and at $\pm 120^\circ$ to the y axis (the y axis being the crystallographic $\langle 11\bar{2} \rangle$ direction of the Pt(111) surface). The parameters V_0, V_1, V_2 and V_3 have been determined by computing the total energy of the fcc, hcp, bridge and on-top configuration of 1 ML pseudomorphic Ag on Pt(111) using first principles calculations within the generalized gradient approximation. The calculated fcc-hcp energy difference is 21 meV, the fcc-bridge difference is 59 meV, and the fcc-top energy difference is 277 meV [66].

The Ag-Ag interactions in the overlayer are modeled using a Morse potential:

$$V_{Ag-Ag}(r) = D[e^{-2m(r-r_0)} - 2e^{-m(r-r_0)}]. \quad (4.6)$$

Whether the layer grows commensurate or dislocated, as well as the period of the incommensurate layer, depend on input parameters of the two potentials: the substrate

potential and the atom-atom interaction in the overlayer. In the latter, three constants are relevant: r_o , the lattice constant of bulk Ag with respect to that of Pt; the cohesive energy between two overlayer atoms D and the bulk modulus of the deposited material m . Those three parameters are deduced from bulk values: r_o is set to 1.041; $m = 3.882(\text{l.u.})^{-1}$ and $D = 492 \text{ meV}$.⁵ With these values for the Morse potential, we find that Ag is commensurate on Pt(111). The unusual large ratio of fcc stacking areas seen in the experiments is explained by the fact that the system Ag/Pt(111) is very close to the commensurate-incommensurate phase transition. Actually, a small increase of D above the theoretical estimate⁶ results in a transition from the commensurate to the incommensurate structure. Furthermore, the spacing between the dislocations is a function of the Morse potential parameters. The dislocations interspacing diverges as the parameters approach critical values where the phase transition occurs. The critical value for D is 547 meV, its bulk-deduced value is 492 meV, the value which reproduces the experimental dislocation interspacing is 570 meV [66].

This divergence of dislocation interspacing near the commensurate-incommensurate phase transition, related with an imbalance between fcc and hcp stacking, is also observed in the reconstruction of Pt(111). The clean Pt(111) surface undergoes a commensurate-incommensurate phase transition when heated to more than 65% of its melting temperature [58]. Near the phase transition the relative fraction of fcc domains is much larger than that of hcp domains.

The Frenkel-Kontorova (FK) model can also be applied to calculate the equilibrium island shape and the equilibrium dislocation structures for Ag islands on Pt(111). STM experiments showed that dislocation structures and island shapes depend on the size of the islands. The islands were created using the following procedure [63]: first 0.12 ML of Ag was deposited at 50K on the Pt(111) substrate, then the film was annealed to 300K in order to enable 2D Ostwald ripening. Subsequently another 0.25 ML of Ag was added at 300 K, resulting in island growth. The islands prepared in this way had a suitable distribution of sizes and shapes necessary for the investigation of their transition from pseudomorphic to dislocated. It was found that dislocations do not appear in islands smaller than 200 Å in diameter, although the spacing of dislocation pairs in a continuous submonolayer film is 75 Å. From 200 Å to 400 Å, there was a gradually increasing probability of finding dislocations in the islands, and islands more than 400 Å across invariably contained dislocations. Dislocations can either be parallel to each other or form y-shapes. Fig 4.17 shows an island with only one pair of dislocations, and Fig. 4.18 show an island with a y-shaped pair of dislocations.

The FK model was used to calculate the energies of hexagonal islands with several different metastable dislocation structures. Four structures were taken into consideration:

⁵One lattice unit (l.u.) is defined by the platinum nearest neighbor spacing as $a\frac{\sqrt{2}}{2} = 2.77 \text{ Å}$, where a is the Pt bulk lattice constant.

⁶ D is estimated by taking the bulk cohesive energy of silver, and dividing it by 6. This value is a lower limit for D because surface Ag-Ag bonds are stronger than bulk Ag-Ag bonds, due to the lower coordination at the surface.

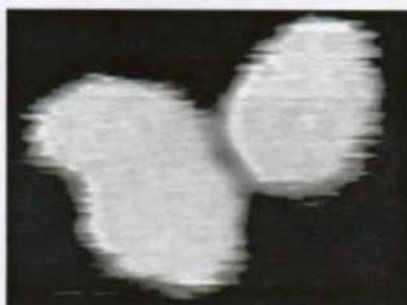


Figure 4.17: STM image of an island crossed by a single pair of dislocations.



Figure 4.18: STM image of an island crossed by a y-shaped dislocation.

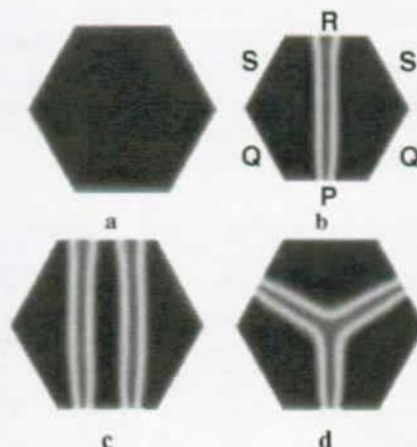


Figure 4.19: Island models used in the calculations. The islands are hexagonal: a) pseudomorphic island; b) island with one pair of dislocations; c) Island with two pairs of dislocations; d) island with a y-shaped dislocation.

the pseudomorphic island without dislocations, the island with one single dislocation pair, the one with two parallel dislocation pairs and finally, the island with a Y-shaped pair of dislocations. Fig 4.19 shows these four configurations. The energies were calculated as a function of island size, using the same FK parameters as those listed above. These calculations gave the following results: islands less than 240 Å wide are stable in the pseudomorphic configuration; for islands between 240 Å and 320 Å in width, the single pair of partial dislocations is the most stable structure; and for islands over 320 Å in diameter, the stable structure is the double pair of partial dislocations.

These calculations are in qualitative agreement with the experimental result that dislocations appear in islands once they are much larger than the dislocation interspacing in submonolayer films. However they do not reproduce the necking effect observed in dislocated islands, where the dislocation meets the island edge. On the other hand, real islands are far from being hexagonal. The FK model gives hexagonal islands as lowest energy configuration, but we do not put a difference of A and B steps in the calculations, nor do we consider the cost for kink sites, etc ... We would presumably obtain dislocation shapes more in accordance with our results if the calculation was done with a given island shape (round, triangular, etc ...), inspired by the real observed shape.

To conclude this section on strain relief at hexagonally close-packed surfaces, we want to stress the following: because crossing of partial surface dislocations is unfavorable (it implies atoms at on-top sites, which is energetically unfavorable), most systems relieve stress in only one direction. This leads to striped dislocation patterns, as can be seen on the bilayer of Cu on Ru(0001) [67], the reconstruction of Au(111) [57] or the bilayer of Ag on Pt(111) grown at room temperature [59]. However, some systems manage to relieve strain in all directions, either by crossing dislocations, as does the annealed bilayer of Ag on Pt(111) and the trigonal network of dislocations of Cu/Pt(111), or with labyrinth-like patterns such as the one observed as a second structure of the second monolayer of Cu on Pt(111) (see fig. 4.12), where the dislocations frequently change direction. It is the trigonal network obtained on 2MLAg/Pt(111) and on 2MLCu/Pt(111) that are of great interest in controlling the nucleation processes because of their high spatial regularity. This will be shown for the growth of Ag, Co and Fe islands in sections 5.1 and 5.2. Note that surface reconstructions and periodic strain relief patterns in thin films are quite frequent, and often show great spatial regularity. Thus they are a potentially powerful tool to generate template surfaces for the growth of regularly spaced islands as we will present in the following chapter. The strain relief processes and patterns presented here for Ag and Cu/Pt(111) are likely to be valid for a wide number of metal on fcc(111)-metal systems.

Chapter 5

Nanofabrication of regularly dispersed islands

In the present chapter, we shall show through three practical examples how strain relief in heteroepitaxial growth can be used to grow regularly dispersed islands. We will discuss the cases of Ag islands on 2MLAg/Pt(111) and those of Co and Fe on 2MLCu/Pt(111).

5.1 Nucleation of Ag on 2MLAg/Pt(111)

One example of controlled nucleation through deposition on dislocated surfaces is that of Ag island formation on the 800K annealed second monolayer of Ag on Pt(111). As mentioned earlier on, in 2MLAg/Pt(111) the compressive strain due to lattice mismatch is relieved in a striped pattern of partial dislocations which separate hcp from fcc stacking areas. The striped reconstruction is metastable, and turns to a trigonal network of dislocations when annealed at 800 K [59]. This trigonal network has the advantage of relieving mismatch strain isotropically, whereas the striped reconstruction relieves strain only in one close packed direction, leaving two directions under considerable compressive strain. It is this annealed second monolayer of Ag on Pt(111) which will be used to nucleate an ordered array of islands by transferring its symmetry to the Ag islands.

The dislocated substrate:

The dislocation network shown in Fig. 5.1 consists of three sets of parallel dislocations running in the three close-packed directions. It has a remarkable regularity, due to the long range elastic repulsive interaction between dislocations. The periodicity of 25 substrate atoms relieves efficiently the compressive strain¹.

Although the trigonal network relieves strain isotropically, it has the drawback that it implies crossing of dislocations, which in turn implies unfavorable adatom positions

¹The Ag lattice constant is 4.3% larger than the Pt lattice constant. Assuming N Ag atoms on $N-1$ Pt atoms, a pure geometric argument predicts a 24 to 25 Pt atoms periodicity to relieve the strain.

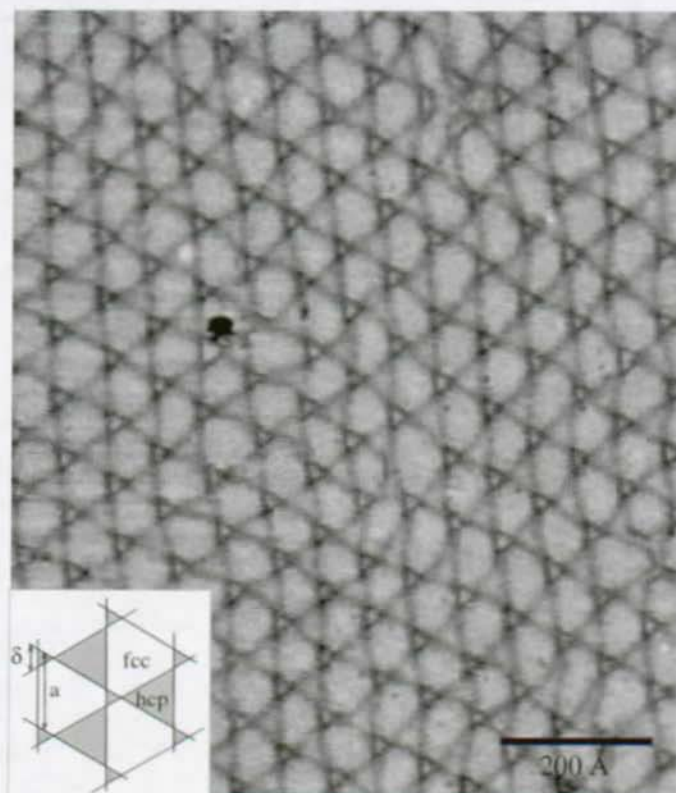


Figure 5.1: 2MLAg/Pt(111) deposited at 300 K and then annealed to 800 K. The black lines are partial dislocations separating fcc from hcp stacking areas. The strain relief pattern presents a perfect regularity due to the long-range mutual repulsive interaction between the dislocations.

at the crossing point. The system avoids the crossing of three dislocations in a single point by shifting one set of dislocations with respect to the two other sets by an offset δ (see inset in Fig. 5.1) [59]. This shift has the additional advantage that it permits larger fcc than hcp stacking areas. The unit cell of the dislocation pattern consists of a large quasi hexagon with fcc stacking and two triangles of different size with hcp stacking, whereas without this δ shift, the unit cell would consist of two triangles of equal size, each one with different stacking.

Nucleation experiments

Ag nucleation on this template shows larger island densities than those obtained with nucleation on Ag(111), which is a signature that dislocations interact strongly with diffusing atoms. Moreover, at low temperatures most islands nucleate off from the dislocations, from which we infer that these dislocations represent repulsive barriers for diffusing atoms².

A closer look at the island density versus substrate temperature (during deposition) reveals three different temperature regimes illustrated in Fig. 5.2. At temperatures below 90 K, the mean free path of an adatom is smaller than the distance between two dislocations. Consequently most atoms will nucleate before they meet the repulsive barrier of the dislocation and island densities versus temperature shows a similar behavior than the one observed on homogeneous and isotropic substrates. STM images in this temperature range show many small islands within each unit cell of the reconstruction pattern (Fig. 5.2 a). Above 130 K, on the other hand, the mean free path of an adatom is much larger than the dislocation interspacing, and the dislocations are readily crossed by the adatoms which form few and large islands similar to those obtained on homogeneous and isotropic substrates with a small diffusion barrier or at high temperature deposition (Fig. 5.2 c).

The most interesting case is the intermediate situation, between 90 K and 130 K. At these temperatures, the adatoms have a mean free path on the pseudomorphic stacking areas, which is larger than the dislocation interspacing, but they don't have enough thermal energy to overcome the repulsive barrier of the dislocations. Therefore all atoms landing in a unit cell of the dislocation pattern form one single island. The result is that within a large range of temperatures (90 K to 130 K) the island interspacing remains constant and corresponds to the substrate periodicity [68]. This striking behavior is shown in fig. 5.2 b), where 0.1ML Ag have been deposited on the trigonal pattern at 110K. At this temperature, the periodicity of the pattern is successfully transferred to the Ag islands.

A detailed STM image of the regular island pattern (fig. 5.3) shows in addition that the islands nucleate on the quasi-hexagon of the unit cell, which by narrowing down the nucleation site increases the regularity of the island interspacing. This implies preferential binding to fcc stacking areas, and that atoms can more easily diffuse from one of the two hcp triangles towards the fcc quasi-hexagon, than the other way around.

The three stages of nucleation can readily be seen in the Arrhenius plot of island densities represented in Fig. 5.4. We can distinguish two slopes at high and low temperatures which are linked by a plateau of constant island densities. In classical nucleation theory, the slopes reveal the energy barrier E_m for one atom to hop from one site to another (see section 4.1). Here clearly the slope at low temperature is a signature of the diffusion within the supercell of the dislocation network (intracell diffusion), whereas

²At higher temperatures we can not see this effect because the average diameter of the islands is larger than dislocation interspacing.

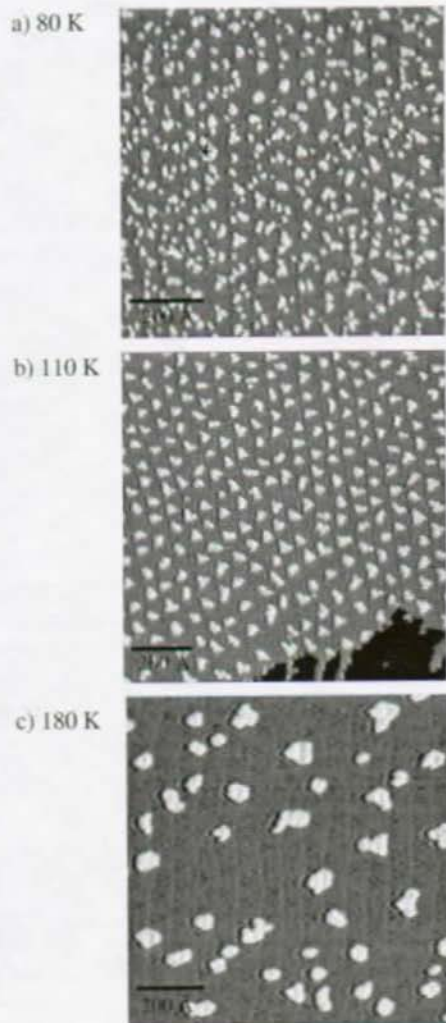


Figure 5.2: 0.1 MAg/2MAg/Pt(111) deposited at a) 80 K, b) 110 K, c) 180 K. Depending on the deposition temperature, Ag atoms can or cannot cross dislocations, leading to three different island distributions. The regular pattern observed in b) is obtained when depositing Ag between 90 K and 130 K.

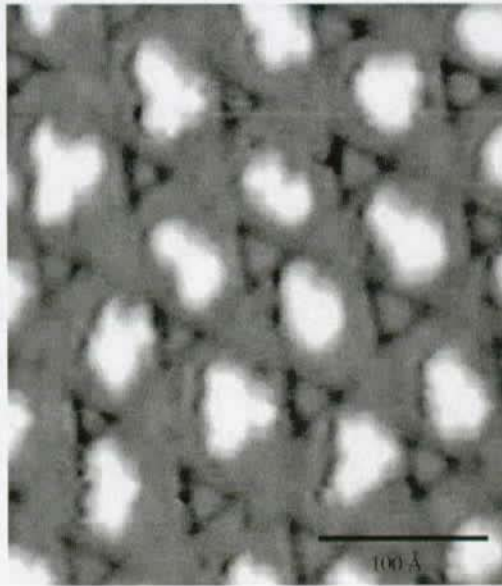


Figure 5.3: Detail of the islands formation on the dislocation network. Ag islands nucleate preferentially on the quasi-hexagon of the unit supercell, and away of the partial dislocations, which leads to a highly ordered island pattern.

the high temperature slope characterizes the diffusion over the dislocations (intercell diffusion). However we are reluctant to use classical nucleation theory to calculate energy barriers for diffusion within the unit cell and across the dislocations because the theory is developed for homogeneous and isotropic substrates.

Kinetic Monte-Carlo simulations

To obtain a quantitative understanding of the activation energies for these diffusion processes, we chose to perform kinetic Monte-Carlo (KMC) simulations on a hexagonal lattice with a (25×25) superstructure [68]. For simplicity we did not distinguish between fcc and hcp sites, hence the unit cell was a simple rhombus, surrounded by the dislocations acting as repulsive line defects. Fig. 5.5 compares the potential used for the KMC simulations and a more realistic one, not used because it implied too many parameters.

In a typical KMC simulation of epitaxial growth, there is a list of displacement processes for adatoms, like diffusion in a selected direction or deposition of a new atom onto the surface, each with a certain rate, thus a certain probability to occur. The rates are given by Boltzmann terms containing the attempt frequency as prefactor and

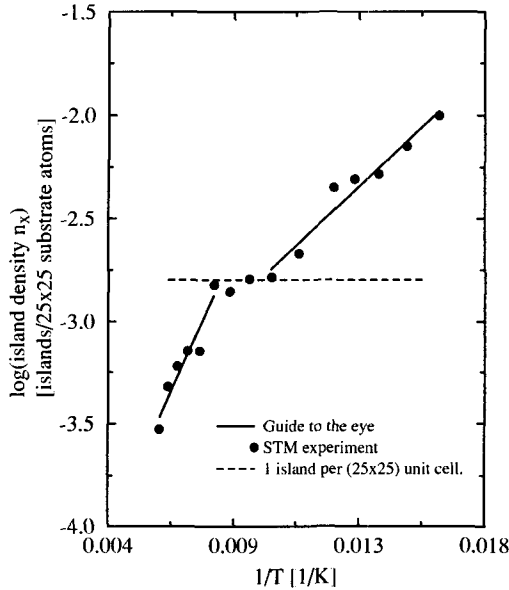


Figure 5.4: Arrhenius plot of a measured island densities. The two full lines are guides to the eye; the dashed line marks density corresponding to one island per surstructure supercell, and the full symbols correspond to STM experiments.

the energy barrier in the exponent. Each atom on the surface has a certain number of possible displacements, depending on its position. For example an atom situated at a step can only diffuse along the step into the two opposite directions, or dissociate from the edge to the free terrace.

With a random number generator, a process is selected out of the total list of possible processes for all atoms, with a probability proportional to its rate and to the number of appearance of this process in the process list. After taking out the move of the selected atom into the selected direction, the process list is updated since the coordination of the atom itself or that of its neighbors might have been affected by the move. Then a new process is randomly selected, and the whole procedure is repeated.

According to the experimental situation (T , F), we did not consider atom dissociation (critical nucleus size $i = 1$) nor reevaporation from the substrate in our simulations. From the different processes allowed, three are most relevant: atom deposition, terrace diffusion and diffusion over a dislocation line. The atom deposition rate is of $\nu_{dep} = F \cdot$ (system size), F being the flux of deposition in atoms per seconds per unit cell. The terrace diffusion, equal in all six directions on the pseudomorphic stacking areas, has a jump rate of $\nu_n = \nu_0 \exp(-\frac{E_m}{k_b T})$ for each direction, E_m being the barrier for diffusion within the unit supercells and ν_0 being the corresponding attempt frequency. The diffusion

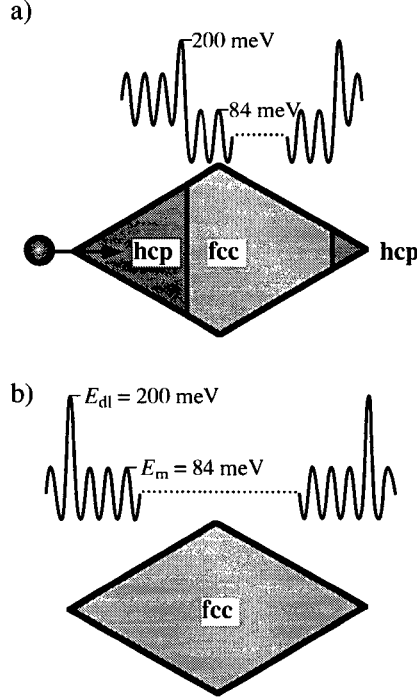


Figure 5.5: Potential used for the Kinetic Monte-Carlo simulations. Fig a) shows a realistic model of the supercell with its associated potential, and Fig. b) shows the simplified model used in our Kinetic Monte-Carlo simulations.

over a line of dislocation has a jump rate of $\nu_n = \nu_{dl} \exp(\frac{E_{dl}}{k_b T})$, E_{dl} being the barrier for diffusion across the unit supercells and ν_{dl} being the corresponding attempt frequency. Thus our four free parameters for the Monte-Carlo simulation are E_m , E_{dl} , ν_0 and ν_{dl} (F and the temperature T are set by the experiment, $F = 7 * 10^{-4}$ [atoms/second and unit cell] and $60 \text{ K} \leq T \leq 180 \text{ K}$).

The simulations (Figs. 5.6 and 5.7) clearly show a transition between two slopes. Through experimenting with various values for E_m and E_{dl} , we convinced ourselves that the high temperature slope was independent of E_m , whereas the low temperature slope relied mainly on E_m . The attempt frequencies, on the other hand, determined the absolute values of the island density for both regimes. Fig. 5.6 shows a set of Monte-Carlo simulation results, where we set E_m to 100 meV, and for different E_{dl} . We can clearly see that the greater the dislocation barrier, the steeper the high temperature slope and the wider the plateau with constant island density. Note that the low temperature island densities are not affected by the choice of E_{dl} .

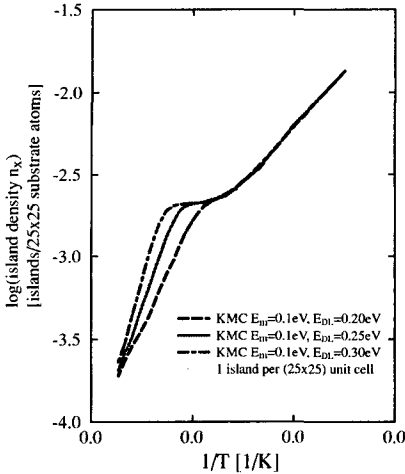


Figure 5.6: Kinetic Monte-Carlo simulations of nucleation on a dislocated surface. The plot shows three simulations where only E_{dl} varied.

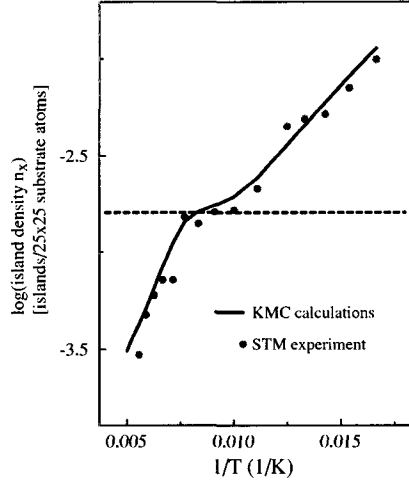


Figure 5.7: This figure shows the good agreement between Kinetic Monte-Carlo simulations and experiment. In the simulations, the plateau is less pronounced than in experiment. This is due to the simplicity of our model, where in particular we did not account for the long range influence of a dislocation on a diffusing atom.

With the values $E_m = 84 \pm 8$ meV, $E_{dl} = 200 \pm 30$ meV, $\nu_0 = 2 \cdot 10^8 s^{-1}$ and $\nu_{dl} = 1 \cdot 10^{10} s^{-1}$ we reproduced experimental results, as shown in Fig. 5.7. The strong repulsion at dislocations explains the extended temperature regime of ordered nucleation. The barrier of intracell diffusion lies between the values measured for Ag(111) self-diffusion ($E_m = 100 \pm 10$ meV), and diffusion on the coherently strained, pseudomorphic first Ag layer on Pt(111) ($E_m = 60 \pm 10$ meV) [52]. This result is in accordance with the finding that diffusion energy decreases with increasing compressive strain in the system [52]. In the fcc and hcp stacking areas of the second layer, the compressive strain is less than in the first layer, but not yet entirely relieved.

In our simulations, the plateau between the two slopes is less pronounced than in the experiment. This is due to the simplicity of the model for the substrate potential. Indeed, we didn't take into account the long range repulsion of the dislocations toward diffusing adatoms. In the experiment, islands are found to nucleate more or less in the center of the quasi-hexagon because of this long-range repulsion. In the Kinetic Monte-Carlo simulations, they nucleate anywhere in the unit cell, and they often touch the dislocations. Thus it is easier to find two islands within a unit cell of the superstructure,

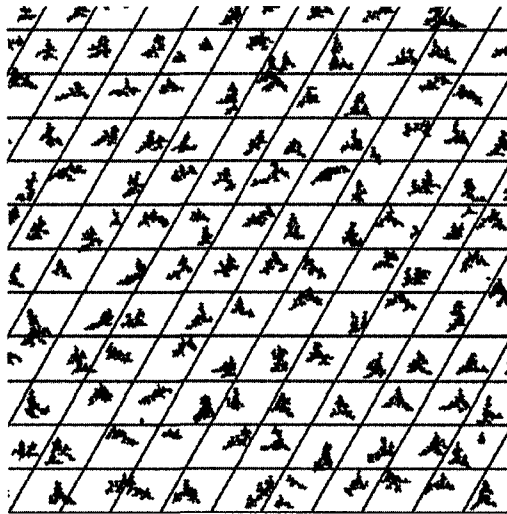


Figure 5.8: Kinetic Monte-Carlo simulation of island growth on a dislocated surface at 110 K. Although the island density corresponds to one island per unit-cell of the superstructure, the islands are not as regularly dispersed as in the experiment. We can see that several islands overgrow dislocations, which is seldom observed in the experiments.

or even an island overgrowing a dislocation. This can be seen in Fig. 5.8 which shows a detail of one of the lattice files produced in our KMC simulations, at a temperature where the average island density corresponds to one island per supercell of the dislocation pattern.

Island size distribution

A valuable side-effect of the ordered nucleation at the intermediate temperature range is an enhanced size uniformity. In Fig. 5.9 the size distribution obtained for ordered nucleation on a dislocation network is compared to that obtained after random nucleation on an homogeneous and isotropic surface. The island size distribution is much narrower in our case than in random nucleation, and is also narrower than that obtained after Ostwald ripening of dimers and trimers [41]. This can be explained because atoms deposited into a network unit cell stay confined to this cell by the surrounding dislocations. In the limit of completely repulsive edges of the supercells, sufficiently high mobility of the atoms to ensure nucleation of only one island, the size distribution of the islands (number of atoms per island) is binomial³: $P_k = \binom{n}{k} p^k q^{n-k}$ (with $p = \Theta, q = 1 - \Theta, k$

³It corresponds to the probability of finding exactly k successes in n trials, when the probability in each single trial is a constant p . Success is defined by depositing one atom, therefore p is given by $p = \Theta$.

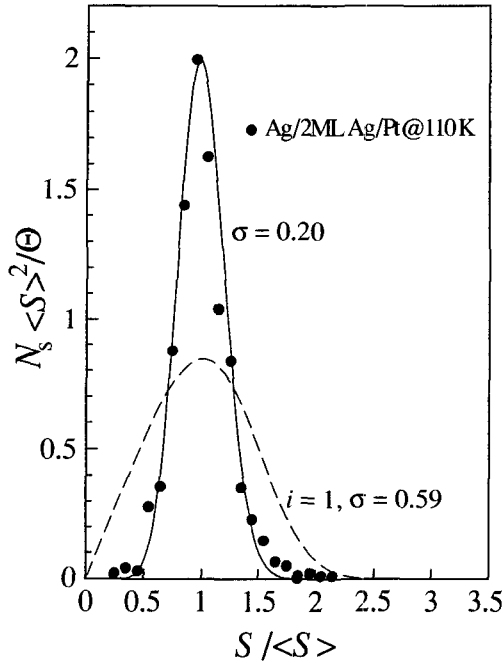


Figure 5.9: Comparison between the experimental size distribution for ordered nucleation (black dots) and the theoretical (and experimentally confirmed) distribution for random nucleation on an isotropic substrate (dashed line). The full curve is a binomial fit to the experimental data. Both size distributions are normalized according to scaling theory [39]. (Θ denotes the coverage, s is the island size in atoms, $\langle s \rangle$ its mean value and N_s the density of islands with size s per substrate atoms.)

being the island size, n the size of the unit cell, and Θ the coverage) [68]. The binomial distribution has a relative standard deviation (normalized to the average island size) of $\sigma = (q/np)^{1/2}$, which yields in our case of $p = 0.1$ and $n = 625$, $\sigma = 0.12$. Our experimental value of $\sigma = 0.20$ is larger. This measured value is an upper limit to the width of the real size distribution, because there is a residual width due to the convolution of tip and island shape. On the other hand, the calculated binomial standard deviation represents a theoretical lower limit to the width of the real size distribution. However the formula of the relative standard deviation reveals the potential of the method: in a system with a superstructure unit-cell as large as in the present case, and a coverage of $\Theta = 0.5$ ML, one expects the relative width of size distribution to be only 4% in cluster areas!

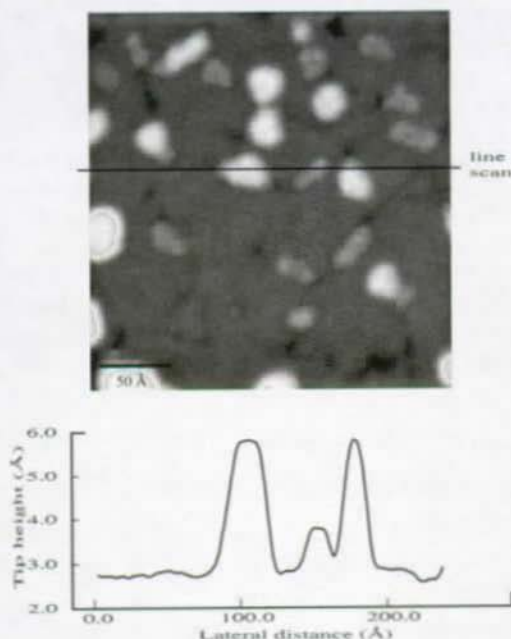


Figure 5.10: Co deposited at 300 K on 2MLAg/Pt(111). A line scan profile is shown under the STM image. The dislocation pattern is destroyed, and two different heights of island coexist, demonstrating that Co has buried in the substrate.

5.2 Nucleation of Co and Fe on 2MLCu/Pt(111)

5.2.1 Attempt of Co and Fe nucleation on 2MLAg/Pt(111)

As nucleation of Ag on 2MLAg/Pt(111) gave promising results, we first tried to nucleate Co and Fe on the same substrate, but we soon noticed that this did not work: Co and Fe islands seemed to nucleate randomly at all temperatures. High resolution STM images gave us the answer as to why it didn't work: the regular dislocation pattern disappeared when Co or Fe were deposited onto the substrate. Fig. 5.10 shows an STM image of the substrate after deposition of Co at 300 K. We clearly see that the dislocation array is largely perturbed, leaving only a small triangle or a piece of dislocation here and there. This can be explained because the Co and Fe surface free energies are much larger than that of Ag, favoring exchange at the surface. Furthermore, Co and Fe are much smaller than Ag, and can easily fill the dislocations, which in addition are low density regions (soft walls): they have half an atom of Ag less than the pseudomorph stacking areas.

So we looked for another element than Ag, which would be smaller than Pt, so that misfit dislocations would be high density regions (hard walls). This element also had

to have a higher surface free energy than Ag, in order to avoid exchange processes with atoms from the Pt(111) surface. Cu seemed to be a good candidate. The following table shows the lattice constant and the surface energies of Ag, Pt, Co, Fe and Cu:

	Ag	Pt	Co	Fe	Cu
Surface energy ⁴ [mJ/m ²]	1550	2550	2550	2550	1850
Lattice spacing [nm]	0.4085	0.3924	0.3545	0.2867	0.3615

Naturally it is necessary that the Cu/Pt(111) system also forms regular dislocation patterns. This is the case as already discussed in section 4.2.1 where the (13x13) dislocation network formed by 2MLCu/Pt(111) was described. In the following section, we present the results of Co and Fe deposition onto this network.

5.2.2 Creating regularly spaced islands of Co and Fe on 2MLCu/Pt(111): formation mechanism

Nucleation experiments on the 2MLCu/Pt(111) substrate demonstrated that the technique used to grow regularly dispersed Ag islands was applicable to other metals. Figs. 5.11 and 5.12 show the monodispersed islands of Fe and Co obtained on the 2MLCu/Pt(111) dislocation network. The result is very similar to the one obtained on the Ag/2MLAg/Pt(111) system. However important differences exist between the Ag system and the two presented here that we shall explore in the following.

First, the preparation technique differs between both systems⁵. In order to obtain the regular network of islands presented here, it is necessary to evaporate 0.1 ML Co on the dislocation network of the second monolayer Cu on Pt(111) at temperatures lower than 100 K, and to anneal subsequently the layer between 200 K and 250 K. Direct deposition at these higher temperatures does not lead to regularly placed islands. This is attributed to a thermally activated exchange, which is suppressed upon deposition at $T \leq 100$ K. Indeed, the surface energies of Co and Fe are higher than that of Cu, favoring the burying of Co and Fe into the Cu template (see table 5.2.1). Site exchange can be replaced at low temperatures since the diffusing atoms have not enough thermal energy to overcome the activation barrier for exchange. When deposited at 200 K, the adatoms have enough energy to make the exchange with the Cu atoms.

Another immediately sizable peculiarity of the present system, is that Co and Fe islands are not only regularly dispersed and of constant size, but also of nice triangular shape. Most likely however, this special shape has nothing to do with the dislocation network, or to the regular islands formation mechanism. Triangular shapes are also observed for other systems like Co on Pt(111) [70], Co/Ru(0001) [71–73], Fe/Au(111) [74, 75] and Pt homoepitaxy [76]. The atomic processes leading to triangles have recently

⁴According to Miedema [69].

⁵We refer to the Fe/2MLCu/Pt(111) and Co/2MLCu/Pt(111) systems as one single system, that we oppose to the Ag/2MLAg/Pt(111) system.

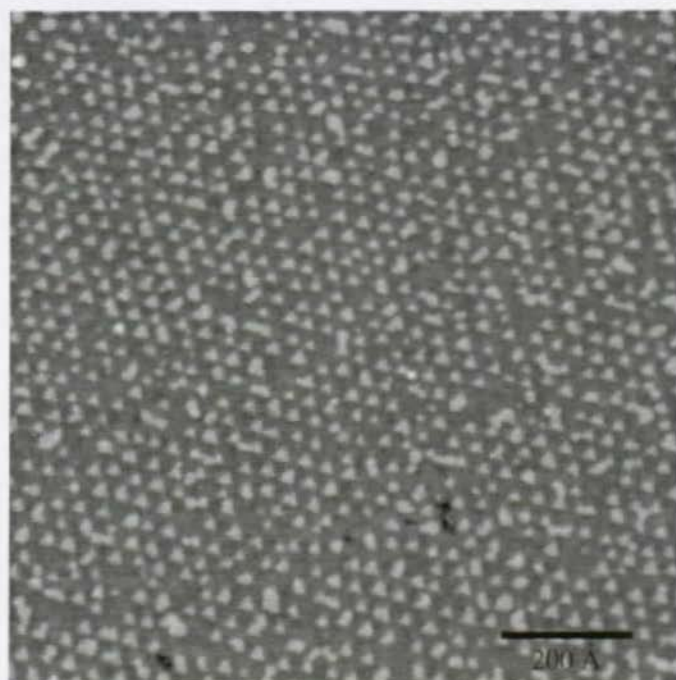


Figure 5.11: 0.1 ML Fe deposited on the dislocation pattern of 2MLCu/Pt(111) at 100 K, and then annealed to 250 K.

been identified [41, 77]. Diffusion anisotropy around island corners, in conjunction with diffusion along island edges, is responsible for the island shape.

To convince ourselves that the triangular shape plays no role in the island distribution, we can plot the island size distribution for this system and compare it with the island size distribution obtained on Ag/2MLAg/Pt(111). If the island shape did play a role for the regular pattern formation, this additional constraint to island formation would narrow the island size distribution. This is not the case, as can be seen in Fig. 5.13, where the size distributions for Co and Fe islands have been plotted, together with the binomial curves for Ag/2MLAg/Pt(111) of Fig. 5.9.

More serious according to the island formation mechanism, is that annealing at higher temperatures than 250 K does not lead to a complete loss of the island regularity. Instead, large regions of monodispersed islands remain, and coexist with "giant" triangular islands. The higher the annealing temperature, the larger the "giant" islands. Fig. 5.14 shows Fe islands after annealing at 300 K. An unchanged regular array of triangular islands coexists with larger islands, some of them with triangular shape.

The use of Fe atoms in large islands implies that they must lack elsewhere. There

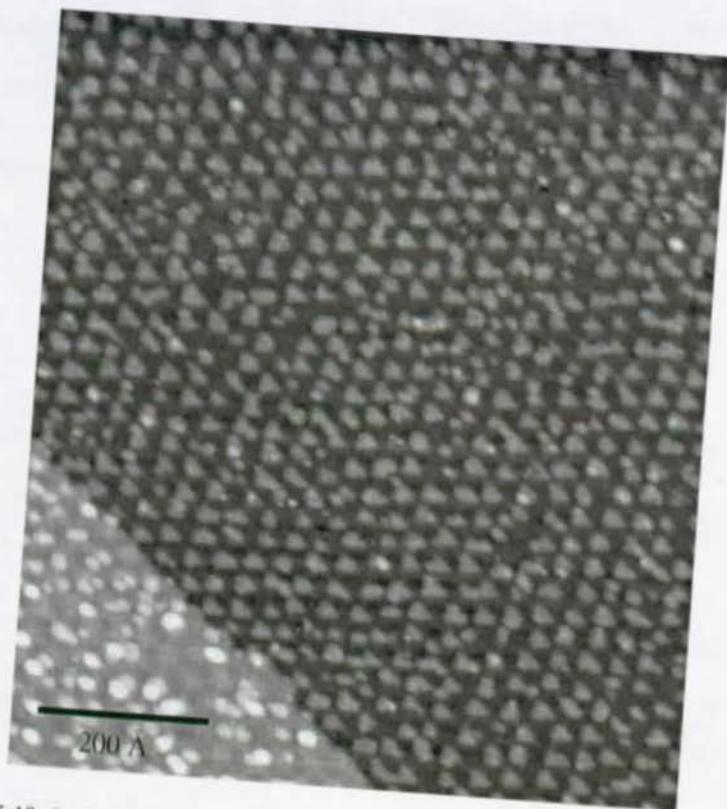


Figure 5.12: 0.1 ML Co deposited on the dislocation pattern of 2MLCu/Pt(111) at 90 K, and then annealed to 200 K.

are some regions without any islands, but these are often located far from the large islands. Two possible scenarios may explain the formation of large islands and bare patches. At high temperatures some Fe atoms may bury into the substrate, forming the empty patches. This implies the removal of Cu atoms which may locate themselves around existing islands, filling the Fe island interspacing and forming these large islands. The other scenario is a sufficiently high atom mobility to reorganize on the substrate, together with preferential places for the large islands to form. Larger islands would not form anywhere, but on special places showing an irregularity of the underlying dislocation array. The first scenario is the most likely, because of the high propensity for Fe atoms to bury into the Cu surface (see table 5.2.1).

In order to understand how the regular Co and Fe islands are formed, we wanted to see where triangular islands form on the dislocation superstructure. The STM image of 0.1 ML Fe after annealing at 300 K shown in Fig. 5.15 was specially treated to enhance the surface corrugation contrast. Three important points can be seen on this STM image.

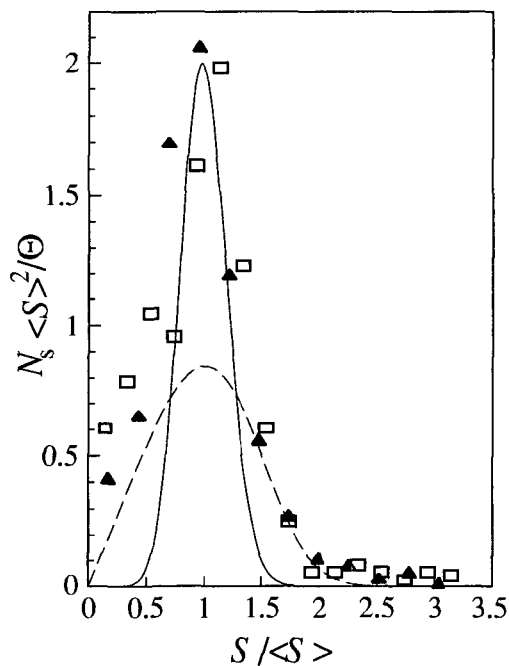


Figure 5.13: Size distributions for the Fe (plain symbols) and Co (empty symbols) ordered nucleation. The plain curve is the binomial fit of the Ag/2MLAg/Pt(111) size distribution of Fig. 5.9. For clarity, we did not reproduce the Ag/2MLAg/Pt(111) experimental dots. We see however that the size distribution is similar for all three cases. The dashed curve is the theoretical distribution for random nucleation.

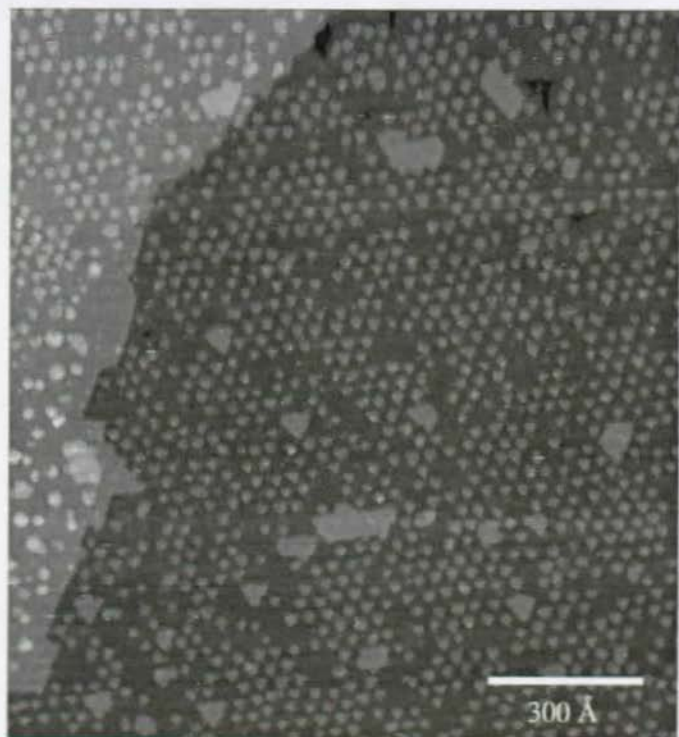


Figure 5.14: 0.1 ML Fe deposited on the dislocation pattern of 2MLCu/Pt(111) at 100 K, and then annealed to 300 K. The regular network remains on most part of the surface. However, bare patches appear, together with the larger islands which seem to be the merges of several small islands.

First, it shows clearly that triangular islands nucleate preferentially on the nodes of the dislocation array, as opposed to what happens for the regularly dispersed Ag islands. Thus the model used in the Ag system can not be used here. Second, it is seen that large islands are the merge of several small islands. They form by first making bridges between the islands and then by filling somehow the space around them to reform a triangular island. The one labelled 3 on the Fig. 5.15 is the merge of three small islands. The superstructure visible on the island can either be due to the strong corrugation of the substrate under it, or to the presence of triangular Co islands connected by Cu atoms. Finally, at the spot labelled 4 the figure shows that the 2MLCu/Pt(111) superstructure on areas bare of islands is the labyrinth one. It is difficult to know whether this defect in the trigonal dislocation pattern preexisted or was induced by Fe atoms burying in the substrate. However, it is seen that the labyrinth structure is correlated with the bare

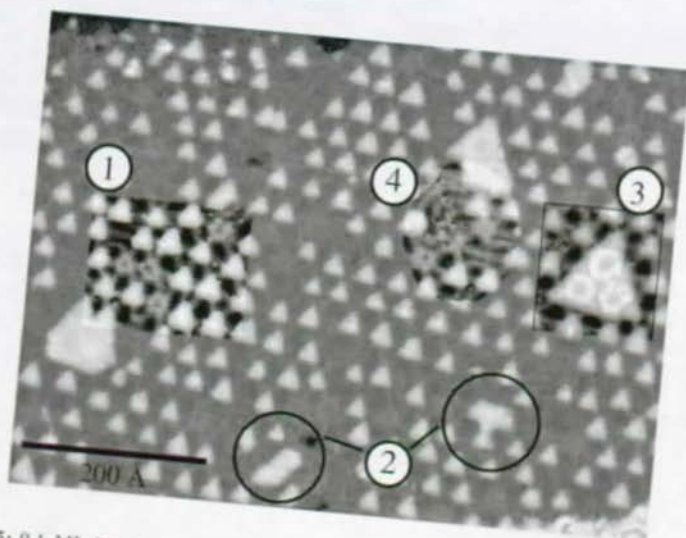


Figure 5.15: 0.1 ML Fe deposited on the dislocation pattern of 2MLCu/Pt(111) at 100 K, and then annealed to 300 K. Region labelled 1 shows how the islands nucleate on the nodes of the dislocation pattern. Both regions labelled 2 show two and three island merging. On the large triangle labelled 3, a structure is clearly seen. It can either be due to the strong corrugation of the substrate or to the presence of two metals in the big triangles, the three spots being the former Co triangle, and the rest being Cu atoms. The area labelled 4 shows a piece of surface without any islands on it. There, the trigonal dislocation pattern is disturbed by the labyrinth pattern.

areas.

It is interesting to note that the merge of islands already happens at a smaller length scale. At 60 K, small islands nucleate so as to form groups of three islands. Upon annealing, these groups of three islands merge to form the small triangular islands that are so nicely ordered. On Fig. 5.16, the annealing of Fe islands from 60 K to 350 K is shown in three steps. At the intermediate temperature of 200 K, triangular islands coexist with some elongated islands which are the merge of two small islands. At 350 K, we have the big triangular islands, already shown in Figs. 5.14 and 5.15.

Before concluding on the regular island formation mechanism in the cases of Co and Fe, we want to emphasize that the coexistence of two energetically equivalent reconstructions of the second monolayer of Cu on Pt(111) (see chapter 4) made it difficult to interpret our results. In our experiments, it often happened that the monodispersed islands did not form. It was difficult to know whether this was due to the mere absence of the trigonal reconstruction, or to its disappearance while depositing Co and Fe, or because of too many impurities, etc ... Thus we must be cautious when drawing conclusions about the regular Co and Fe islands formation mechanism.

To summarize, the following features were determined for the Co and Fe nucleation on 2MLCu/Pt(111). First, triangular monodispersed islands of Co and Fe form by preferential nucleation on the nodes of the trigonal network, contrary to what happens on the Ag/2MLAg/P(111) system. Second, deposition on the labyrinth-like reconstruction does not lead to regularly dispersed islands. Third, at very low temperatures (60 K), three small islands nucleate around each dislocation node. They merge into small triangular islands upon annealing at 200 K. Annealing at higher temperatures leads to missing triangles in the hexagonal pattern, and to larger islands which are the merge of several small islands. Most likely, this happens by atom exchange between Co or Fe atoms and Cu atoms from the substrate. The higher the annealing temperature, the more atoms merge in a single island. Finally, deposition at 200 K or higher does not lead to monodispersed islands, presumably because of atom exchange between Co or Fe and the underlying Cu template.⁶

⁶The thermal energy adds up to the adsorption energy gained by the atoms upon binding on the template.

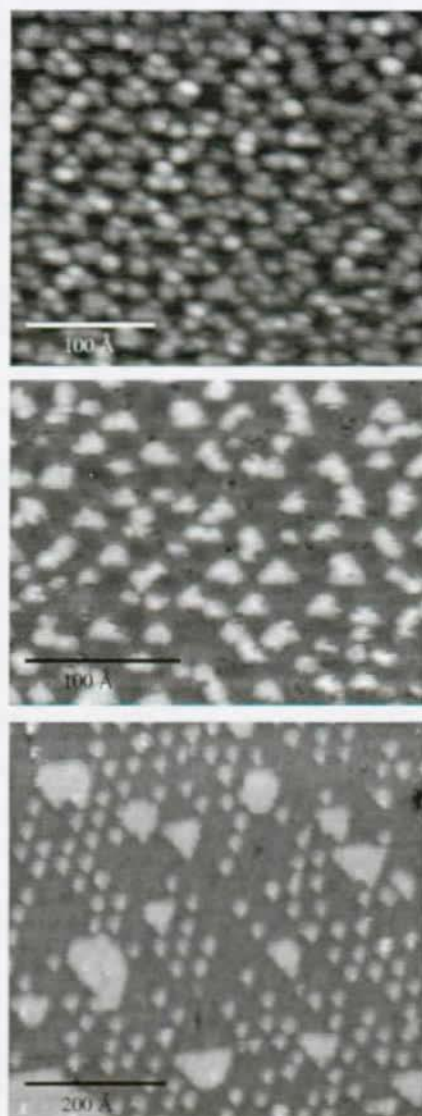


Figure 5.16: 0.1 ML Fe deposited at 60 K and imaged at 60 K (top); the islands are grouped by three. They merge upon annealing to form the triangular islands (middle 200 K annealing temperature, bottom panel 350 K).

Chapter 6

Magnetic behavior of thin films and islands

6.1 Co/Pt(111)

In this chapter, we will present the SMOKE measurements done on monolayers and submonolayers of Co deposited on Pt(111). The organization of the chapter is the following: first we will give a description of our experimental procedure, i.e. how we measured what, what difficulties we had and what were the solutions we applied. Then we will present our results, which focus on three aspects and three corresponding paragraphs. In the first one, we will present the magnetization versus coverage for coverages between 1 and 20 ML. We will present our polar and transverse SMOKE results for these coverages. In a second paragraph we will treat the effect of temperature on the hysteresis curves for a specific coverage. Finally we will concentrate on low coverages and present our results for submonolayers of Co on Pt(111) with different preparation conditions and subsequently different morphologies for the Co islands.

6.1.1 Experimental procedures

We applied two different procedures when investigating the magnetism of thin layers of Co on Pt(111), each with its advantages and drawbacks. The initial experimental procedure was the following: After cleaning the Pt(111) crystal following the preparation described in chapter 3, we deposited the desired amount of Co on the sample facing the Co evaporator. Next the sample was oriented to face the STM head, and we took STM images in order to characterize the sample morphology. Then the STM was removed, and SMOKE measurement were done¹. Possibly new Co deposition was done, followed by new STM and SMOKE measurements.

This procedure was time consuming and led to reproducibility difficulties. Although

¹The order of STM and SMOKE measurements was sometimes reversed.

measurements were reproducible qualitatively, they were not so quantitatively. Two identical measurements done on two different days gave different absolute SMOKE intensities, (although the SMOKE signal was normalized to the reflectivity of the sample spot with parallel aligned polarizer and analyzer) making difficult an investigation of the SMOKE signal versus Co coverage. There are two possible sources for these difficulties. The first possible reason could have been an inhomogeneity of the Co deposition on the crystal. Since each SMOKE adjustment led to the investigation of a different area on the crystal, a local variation of the coverage would lead to quantitative non-reproducibility. However, AES (Auger Electron Spectroscopy) measurement at different positions of the sample as well as STM investigations revealed that the Co deposition was homogeneous to within 10 %. The second more plausible reason are local variations in step density leading to different growth morphologies which in turn have different magnetic properties².

In order to overcome the problem of non-reproducibility, we applied an other measurement procedure. After cleaning the crystal, we oriented it in the SMOKE measurement direction and adjusted the SMOKE. Then we deposited the Co *in situ*, i.e. without moving the sample from its measurement position. This caused a reduction of the Co flux by $\cos 35^\circ$. We recorded the hysteresis loops either under continuous deposition (with very low deposition flux), or in steps, depositing successive amounts of Co, and measuring between the depositions. Apart from the advantage of staying on the same surface spot and that measurements conditions do not change during a whole set of measurements points, this procedure is very convenient because it is very rapid: we could have as many measurement points in one day as in one week by the other method. The main drawback of this method is the absence of STM images corresponding to each coverage measured. Since we were highly interested in the topography, especially for low coverages, we had to rely on STM measurement done separately on other measurement days. However this measurement procedure was very helpful, in particular for the first part presented below: the measurement of the SMOKE signal versus coverage, which would not have been possible with the initial method³.

6.1.2 Results

Magnetization versus coverage

We performed transverse and polar SMOKE measurements at 300 K on thin layers of Co on Pt(111) up to 20 ML. We observed that the easy axis of magnetization, first out-of-plane at low coverages, turns to be in-plane upon increasing the film thickness. The transition happens between 2 and 3 ML. The results are shown in Figs. 6.1 and 6.2, where the out-of-plane, respectively in-plane magnetization of Co films is plotted

²Macroscopical defects of the sample are the reason for theses local variations in step density, which are visible by STM measurements.

³I wish to thank Emanuelle Vargoz and Stephano Rusponi, who did the SMOKE measurements according to the second measurement procedure.

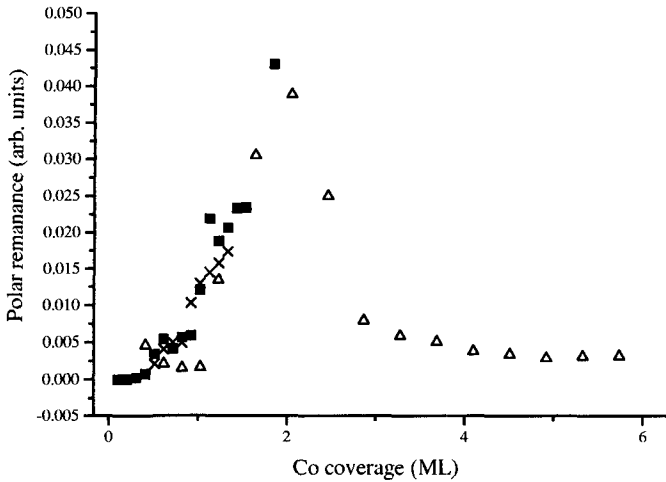


Figure 6.1: Polar SMOKE measurements at 300 K. We report the remanent magnetization as a function of the Co coverage. The polar signal increases as more Co is deposited up to 2 monolayers. Then the signal decreases and falls to nearly zero at 3 ML. The different symbols denote different measurement days.

as a function of the film thickness. The polar signal increases from 0.5 ML on, up to 2 ML where it reaches a peak, and then the signal diminishes to fall to nearly zero at 3 ML. This means that from 0.5 ML on, the film exhibits a ferromagnetic behavior. The magnetization increases with the Co coverage up to 2 ML, and then the signal decreases as the easy axis of magnetization progressively changes from out-of-plane to in-plane. Meanwhile, the transverse signal is zero up to 2 ML, quasi zero between 2 and 3 ML, and starts to increase linearly from 3 ML on up to the highest coverages investigated.

The intermediate stage, between 2 and 3 ML, where both transverse and polar signal is visible can be explained by the formation of domains of different magnetization directions. This can easily happen, seeing that the film is far from being homogeneous in thickness. Regions with 1 ML Co coexist with 2, 3 and even 4 ML high Co regions (see Fig. 6.3 b) and c).). The parts where the film is thinner very likely still have an out-of-plane magnetization easy axis, whereas where the film is thicker, the magnetization presumably has already switched to in-plane. Even for a constant film thickness, different easy axis domains could coexist. For Fe/Cu(100) for example, it has been reported [78] that the transition from in-plane to out-of-plane easy axis occurs gradually over a film thickness range of two monolayers, or for a constant film thickness and variable analysis temperature, over a temperature interval of 50 K.

The non-homogeneity in the film thickness also explains that the polar Kerr intensity remains non-zero after 3 ML, up to $\sim 6 - 7$ ML, remaining nearly constant. The fact

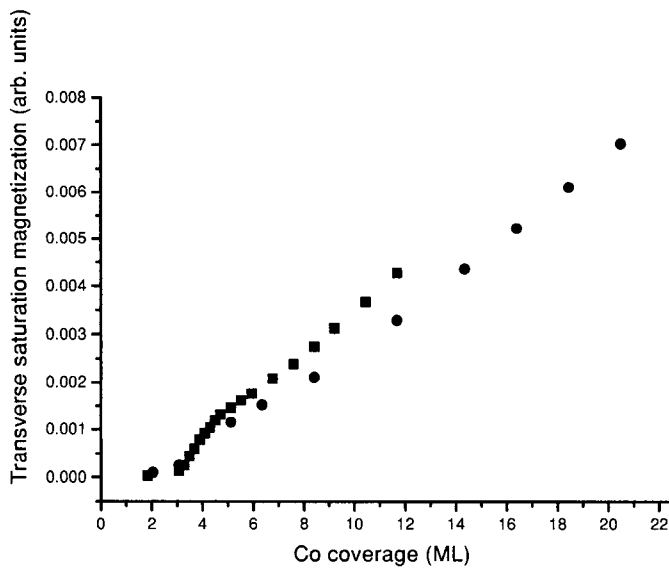


Figure 6.2: Transverse SMOKE measurements at 300 K. The saturation magnetization is plotted as a function of the film coverage. The signal appears at 3 ML and then increases linearly. Different symbols denote two different measurement days.

that the first monolayer is still visible after deposition of 4 ML or more, explains this remanence (see Fig. 6.3 c)). Presumably, the parts of the film with one or two monolayer thickness keep an out-of-plane magnetization easy-axis.

An other possible reason for the remanence of polar signal is a small misalignment of the surface with respect to \mathbf{H} . In this case however, the remanent polar signal should be present at any film thickness, and increases with increasing magnetization, or film thickness, which is not the case.

The change of easy axis of magnetization from out-of-plane to in-plane upon increasing the magnetic layer thickness was already observed on several thin layer or sandwich systems, as for example Fe/Cu(111) [78], Pt capped Co thin layers [79] or Pd/Co and Pt/Co multilayers [15]. Multilayers and capped layers behave similar to overlayers, in that the magnetic anisotropy direction depends on the thickness of the magnetic film(s). However those systems are more complex: the magnetization also depends on the non-magnetic layer thickness. This is the case for example for Co grown on a stepped Cu(100) substrate, whose magnetic anisotropy oscillates with the Cu overlayer thickness [80].

In the case of thin overlayers, the interaction with the non-magnetic substrate may also influence on the magnetization of the sample. However this remains constant for a given sample, the thickness of the substrate being usually large with respect to the magnetic overlayer. In these systems, the reason for the change in easy axis direction with the magnetic film thickness is the large uniaxial surface anisotropy present in these epitaxial systems, competing with the shape anisotropy. In many cases, the out-of-plane easy axis is favored for thinner magnetic films.

The surface anisotropy is obtained by calculating the spin-orbit energy as a function of the spin direction, the lower energy corresponding to the easy axis direction. The out-of-plane magnetization easy axis was predicted for 1 ML thick films of Fe and V, whereas in-plane anisotropy was predicted for 1 ML thick film of Ni [81]. For thicker films, the classical dipole interaction that favors in-plane magnetic anisotropy overwhelms the spin-orbit interaction, and the magnetization easy axis tends to be in-plane.

Our results can be compared with a recent publication, where SMOKE measurements of Co deposited on Pt(111) at room temperature as a function of Co thickness were reported [82]. These results are quantitatively slightly different from ours. It is found that in-plane magnetization (longitudinal SMOKE in their case) appears after 3.7 ML, and that polar hysteresis loops remain together with longitudinal hysteresis loops until 5.8 ML, the maximum of polar Kerr intensity being at nearly 5 ML. The difference of in-plane magnetization onset between these measurements and ours can be due to inaccuracies in flux calibration. However, this can not explain that the maximum of polar Kerr intensity is observed in our case before the onset of in-plane hysteresis loops, and in their case after this onset.

A difference in the film preparation could be responsible for the shift of the polar Kerr intensity peak. In the above mentioned publication, the coexistence of polar and longitudinal Kerr signals is attributed to 3d growth which occurs from 4.5 ML on. We did not record STM images of more than 4 ML Co/Pt(111). However, a small difference in the deposition temperature could easily shift the onset of 3D growth. Our STM

images show that at room temperatures, islands grow immediately 2 ML in height. Figs. 6.3 a), b) and c) show STM images of Co deposited on Pt(111) at the coverages of respectively ~ 0.8 ML, ~ 2 ML and ~ 4 ML. The underlayer Pt substrate is still visible in all cases.

Measurements at 200 K of films grown at 200 K reveal a slightly different behavior. The polar Kerr signal does not increase steadily. Instead, it shows a first local maximum in the region of 0.5 ML, then falls to nearly zero at 1 ML to increase again to the maximum, which occurs at the same coverage as for the case of films grown at 300 K. This behavior is shown in Fig. 6.4. Of course, there are morphological differences between films grown at 300 K and at 200 K. In the latter case, islands are smaller and a smaller proportion of them are bilayered (see Fig. 6.13, and compare with Fig. 6.3 a). However, this does not necessarily mean that the difference in magnetization behavior is due to the morphology difference of the two films.

In order to test whether this behavior is due to the temperature of the Kerr measurement or to a different film structure due to a different deposition temperature, we also performed Kerr measurements at 200 K of films grown at 300 K. On these films, the first maximum is clearly visible as can be seen in Fig 6.5, where we increased the number of measurements in the submonolayer region with respect to Fig. 6.1. We conclude that it is the temperature of the Kerr measurement rather than the growth temperature that is determinant for the presence or the absence of the 0.5 ML maximum.

A possible reason for the higher value of the magnetization at half a monolayer than at one monolayer can be an increase of the magnetic moment per atom for step-atoms compared to the magnetic moments for surface-atoms. It is well established that surface atoms have a higher magnetic moment than bulk atoms. Similarly, atoms in steps have a higher magnetic moment than surface atoms. For Fe for instance, the enhancement is of the order of 0.5 to 0.8 μ_B for the step atom as compared to the surface atom, reaching $3.5 \pm 0.5 \mu_B$ [83, 84]. ($\mu_{surf} = (2.7 \pm 0.2) \mu_B$ for a bcc Fe(110) surface). The continuous increase of the spin magnetic moment from bulk, through surface, steps and to free atoms is attributed in theory to a decrease of the number of nearest neighbors, connected with a decrease in band width [85]. For Co, it has been established that the enhancement of the magnetization at step edges relative to the magnetic moment per surface atoms is about 5% [86], the later being of $1.8 \pm 0.1 \mu_B$. The effect on the magnetization of the magnetic moment increase at step sites was already observed for Co on Cu(001) [87]. The authors of ref. [87] observed a periodic oscillation of the magnetization between 2 and 8 ML, which they attributed to a periodic increase by 10 to 20% of atoms sitting at step sites at half filled layers.

Note that if we compare STM images of 0.6 monolayer and 0.8 monolayer Co on Pt(111), we can estimate that the step atoms increase by roughly 16%, leading to magnetic moment increase of 0.05, which is much lower than the enhancement observed of 0.6. ($I(0.6ML)/I(0.8ML) = 1.6$) In the above mentioned publication, the same anomaly was observed.

A more realistic reason for the form of the SMOKE signal versus coverage is an increase of the coercive field around 1 ML. A careful observation of the hysteresis loops

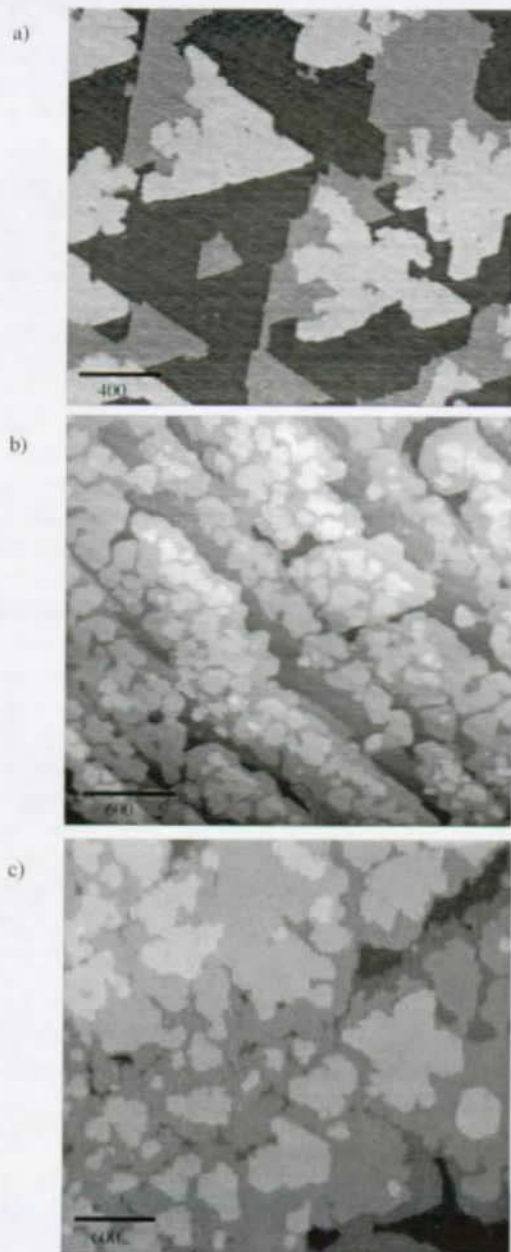


Figure 6.3: STM images of Co/Pt(111) grown at room temperature: Co grows in bilayer islands and keeps this tendency when two or more ML are completed. a) 0.8 ML Co/Pt(111). b) 2 ML Co/Pt(111). c) 4 ML Co/Pt(111).

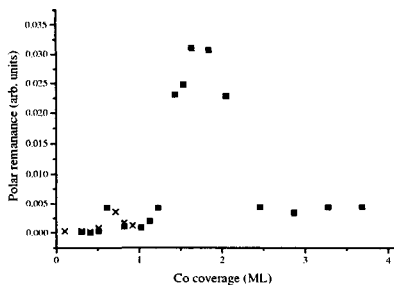


Figure 6.4: The polar SMOKE signal on films up to 3.7 ML deposited and measured at 200 K. Different symbols denote different measurement days.

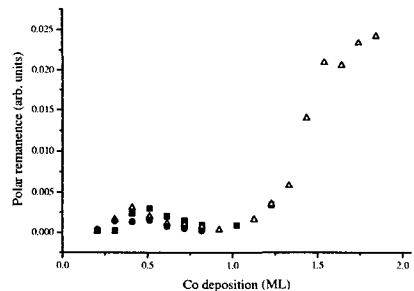


Figure 6.5: Polar Smoke measurement of films grown at 300 K and measured at 200 K. Clearly the first bump is present.

in the region between 0.5 and 1.5 ML reveals that the sample is not saturated. Thus the reduction of the apparent polar remanence can be due to an increase of the coercive field, at a such value that the saturation of the sample is not possible anymore with our magnetic field. In Fig. 6.6, we plotted the polar SMOKE intensities of films grown at 300 K and measured at 200 K together with their coercive fields. The coercive field is measured taking the x value at $y = 0$ Tesla of the loops curve. It has a finite value even when the film is not saturated. Some loops corresponding to points of the plots are also shown. We see that in the hollow region between 0.5 and 1.5 ML, the film is not saturated. According to these considerations, the real SMOKE intensity curve would be monotonous, following approximatively the dashed line. Likewise, the coercive field curve would increase to a higher maximum, around 1 ML cobalt coverage. A higher magnetic field would be necessary to confirm this hypothesis.

The fact that the magnetization enhancement at 0.5 ML doesn't appear when measuring at 300 K, is still not clearly explained. However, since the coercive field certainly depends on the measurement temperature, the effect mentioned above could disappear depending on the position of the peak of the coercive field. Indeed, curve analysis shows that the coercive field peak appears at a lower coverage (see the following paragraph and Fig. 6.9). This would of course weaken the above effect, since at smaller coverages, the Kerr signal is smaller.

Coercive field versus measurement temperature

The magnetic film behavior strongly depends on the sample temperature (for example, the easy axis of magnetization of a given film, can switch from polar to in-plane by varying the temperature [88,89]), as well as on the film deposition temperature. This last dependence comes from the structural temperature dependence, which in turn influences the films magnetic properties. We shall come again to this point, but we will first

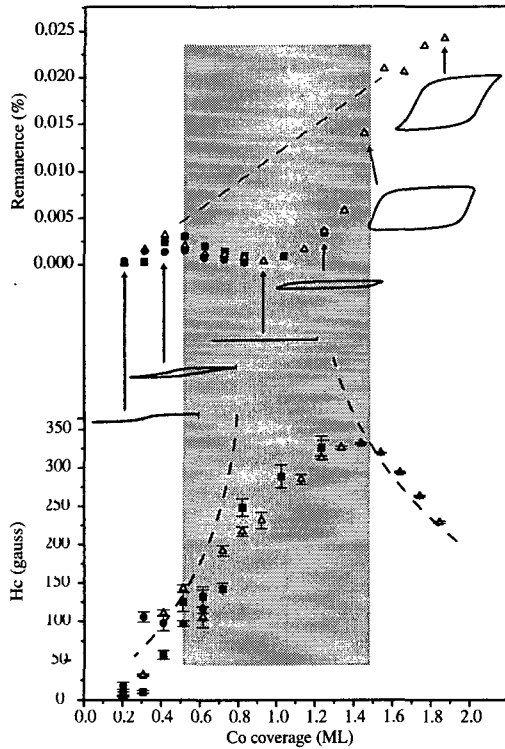


Figure 6.6: Polar SMOKE signal of films grown at 300 K and measured at 200 K. up: polar remanence; down: coercive field. Some loops corresponding to given points of the curves are shown. We see that the decrease of the SMOKE intensity corresponds to the region where the coercive field is not saturated anymore. The real remanence signal might well increase linearly, following the dashed line. In dashed line too is drawn an extrapolation for the real coercive field. The measurements points in the grey region are those for which the hysteresis curves were not reliable because of a non saturation of the films.

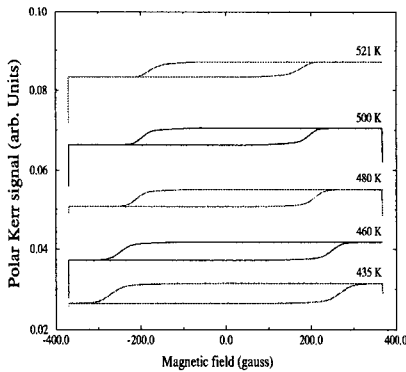


Figure 6.7: Temperature dependence of the coercive field from a 3.5 ML Co film deposited at 315 K. This evolution is not due to a film transformation and is reversible.

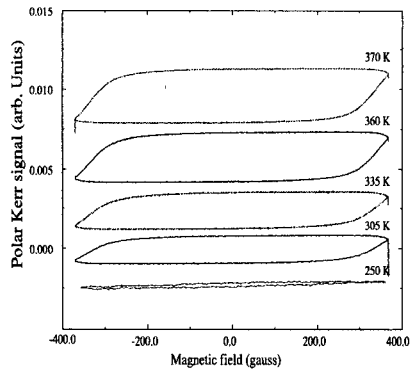


Figure 6.8: Same film as Fig. 6.7. Below 370 K (and with the available magnetic field) the film is not saturated anymore. The lower the temperature, the smaller the remaining loop. The ferromagnetic behavior can be completely hidden when the film is measured at low temperatures.

concentrate on the measurement temperature dependence for a given morphology.

In measuring magnetic behavior, one can focus on the saturation or the remanent magnetization, the easy axis direction⁴, the coercive field, etc ... Since we only have access in a semi-quantitative way to saturation and remanent magnetization, we prefer to concentrate on the coercive field when looking at the temperature dependence.

The coercive field of thin layers diminishes with increasing sample temperature. This is not different from the bulk behavior. A high sample temperature helps the reversal of the magnetization by increasing the spin mobility. This dependence is clearly visible from Fig. 6.7 where 3.5 ML have been deposited on Pt(111) at 315 K and measured between 460 K and 520 K. The consequence for our measurements was that because of the limitation of the available magnetic in-plane field, Kerr measurements at low temperatures did not allow full film saturation. Thus no quantitative nor even qualitative information could be extracted below a certain temperature (depending on the film thickness). Fig. 6.8 shows the same film as Fig. 6.7, measured below 370 K where the film is not saturated. Here, the effect of lowering the temperature is a decrease of the apparent height of the hysteresis loop. This decrease goes on until the remaining signal vanishes in the measurement noise, and the loop closes.

From Figs. 6.1 and 6.5 (polar remanence for films grown at 300 K, and measured at

⁴In the present measurements, we did not observe any easy axis direction switch upon varying the sample temperature.

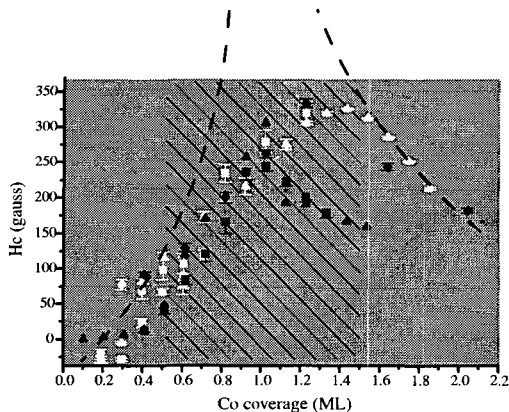


Figure 6.9: Coercive field versus film thickness for films grown and measured at 300 K (black symbols) and for films grown at 300 K and measured at 200 K (white symbols). The form of the coercive field versus film thickness is similar for both films. In the dashed region, the measurement points are unreliable, the film being not saturated. In dashed line is the extrapolated coercive field.

300 K respectively 200 K), we can see that the overall magnetic behavior depends on the sample temperature. In Fig. 6.9, we plotted the coercive field versus film thickness for both films. We wanted to correlate differences in the saturation fields, with differences in the coercive field. However, we must be aware that we still have the same problem of non-saturation. Both films have their coercive field increased with increasing film thickness up to a peak (between 1 and 1.6 ML, not attainable with our available magnetic field), and then decreased again. The initial increasing slope is identical for both films, but the film measured at 200 K seems to have its maximum coercive field peak at a slightly higher coverage. However, two different measurements on the last films gave once an extrapolated peak around 1 ML, and the other time around 1.2 ML, so that the difference between the film measured at 300 K and the one measured at 200 K is not too conclusive. Moreover the coercive field depends on many other parameters, like the size of domains, the film morphology and purity which are difficult to control.

Coercive field versus film structure

One evidence of the dependence of the coercive field on the film structure can be obtained by measuring films grown at different temperatures, since the film structure varies with growth temperature. This dependence is illustrated in Fig. 6.10 for 1.3 ML thick Co films deposited between 100 and 200 K. The higher the deposition temperature, the larger the coercive field. We can assume that the film is smoother when deposited at 200 K, and forms larger patches and islands than if deposited at 100 K. Thus, the

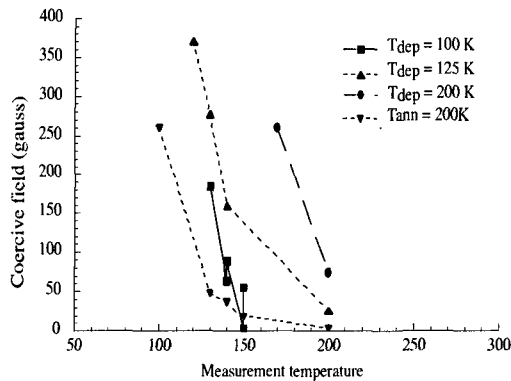


Figure 6.10: Coercive fields versus temperature of 1.3 ML Co films for different deposition temperatures. The higher the deposition temperature, the bigger the coercive field. Annealed films have a lower coercive field than unannealed films.

coercive field is related to the islands size, being larger for larger islands.

Note that for a film deposited at 100 K and subsequently annealed to 200 K, the coercive field is lowered with respect to unannealed films and to films directly deposited at 200 K. STM images do not give any clarifications why the coercive field is lowered after annealing. Both surfaces show an almost complete first monolayer covered by small second layer islands. This structure is shown in Fig. 6.11. Note however that different deposition procedures may lead to films containing different amount of impurities, which also plays a role in the coercive field.

Varying the measurement temperature can also make a given film undergo a ferromagnetic-paramagnetic transition. This transition naturally happens at the Curie temperature. Fig. 6.12 shows an example of this transition for a 1.3 ML Co film deposited at 100 K (STM image of the same film: Fig. 6.11). Here, the transition happens around 180 K. The thinner the film, the lower is the Curie temperature. Note that the fact that the hysteresis loop disappears is not alone a proof that we reach the Curie temperature. It could also mean that the easy axis of magnetization has turned from out-of-plane to in-plane. In the present case, no hysteresis loop was observed in the transverse setup.

So measuring thin films confronts with the following double difficulty: we must be able to lower the sample temperature to measure a possible ferromagnetic behavior, but measuring at too low temperature can hide the ferromagnetic behavior if the coercive field is too high (see Fig. 6.8). To overcome this difficulty in the future, we are presently transforming the UHV chamber in order to allow magnetic fields up to 1 Tesla.

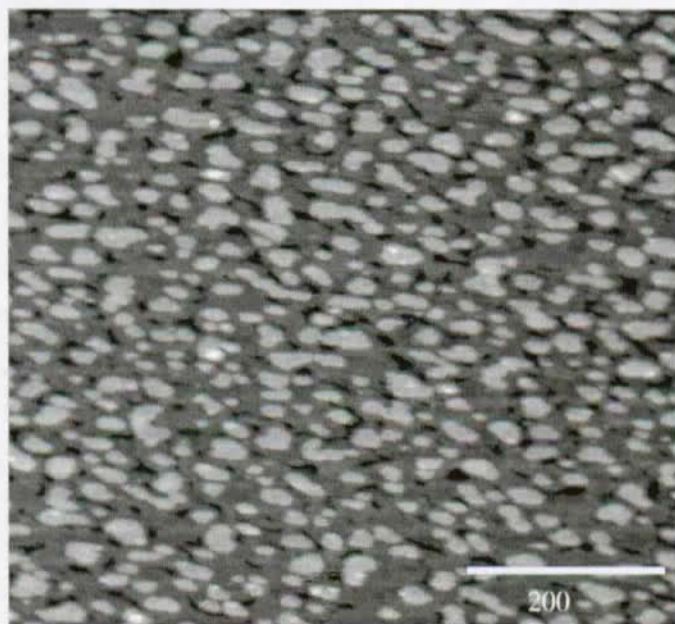


Figure 6.11: 1.3 ML Co deposited at 100 K and annealed to 200 K.

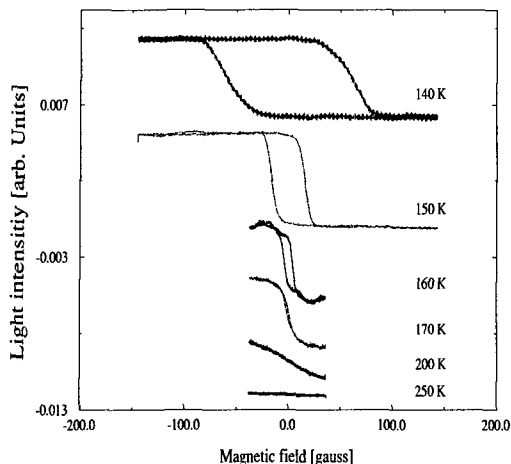


Figure 6.12: Polar SMOKE on a 1.3 ML film deposited at 100 K. The film undergoes a transition ferromagnetic-paramagnetic upon increasing the film temperature

Magnetization of submonolayers

The present work principally deals with metallic nanostructures: small islands and submonolayers. Thus we wanted to characterize the magnetic behavior of those structures. We wanted to find out the following features. When does submonolayer Co films start to be ferromagnetic? Does it happen at the moment where the islands coalesce? Are bilayered islands different from monolayer islands with respect to magnetism? Are the shape or size of those islands reflected in their magnetism? In the following we concentrate on two morphology points: coalescence and bilayered Co islands.

a) Coalescence versus ferromagnetism. As can be seen in Fig. 6.1, for films deposited and measured at 300 K, an hysteresis in the polar loops opens up from 0.5 ML on. In films measured at 200 K, the appearance of polar ferromagnetism and with it a coercive field is detected even earlier (see Fig. 6.5). This is far before island coalescence as already shown in Fig. 6.3 a. Even for films grown at lower temperatures, the coalescence hardly begins before 0.7 ML as can be seen in Fig. 6.13, where 0.7 ML Co have been deposited at 150 K, and where the coalescence just begins. Thus ferromagnetism already happens in small islands, without islands being connected with each other. Looking at the island width of Figs. 6.3 a and 6.13, we can conclude that ferromagnetism already happens in islands 200 Å or less in width.

b) Bilayered versus monolayered islands. To know whether the height of the islands played any role, we evaporated 0.7 ML Co on Pt(111) at 150 K, where islands grow monolayered, and we made SMOKE measurements of this film between 50 K

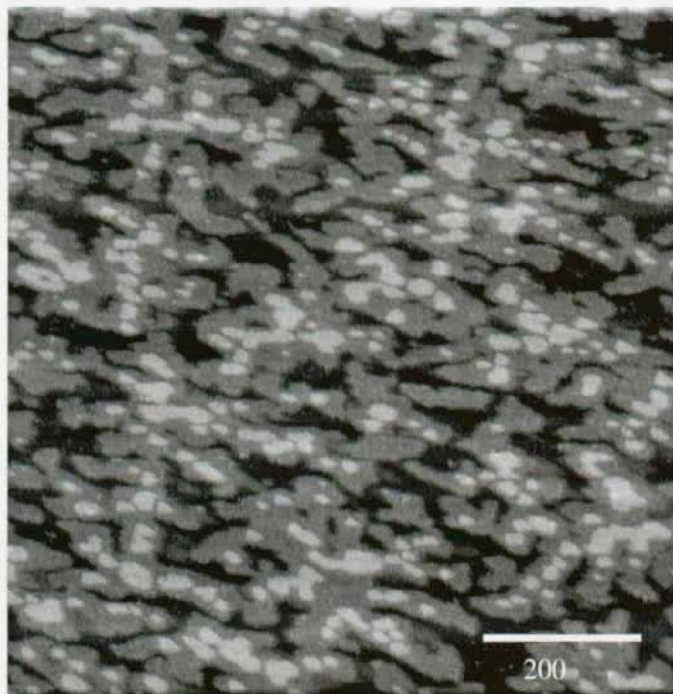


Figure 6.13: 0.7 ML Co deposited at 150 K on Pt(111). At this temperature, a lower proportion of the surface is bilayered, and the coalescence happens at lower coverages than for films grown at room temperature. Here islands are almost coalesced.

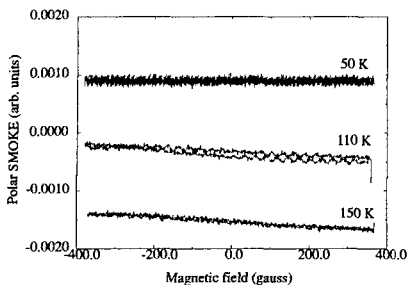


Figure 6.14: Polar SMOKE on the unannealed 0.7 ML Co film, deposited at 150 K and measured between 50 K and 150 K.

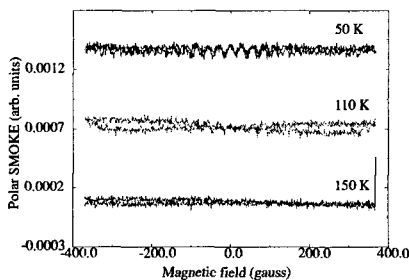


Figure 6.15: Polar SMOKE on the 400 K annealed 0.7 ML Co film, deposited at 150 K, annealed and then measured between 50 K and 150 K.

and 150 K. Subsequently, we annealed that film up to 400 K, so that bilayered islands form [90]. In the limits of our experimental possibilities, SMOKE measurements between 50 K and 150 K of the annealed film reveals a behavior similar to that of the unannealed film, i.e. no ferromagnetic behavior. Results are shown in Figs. 6.14 and 6.15. We conclude that no ferromagnetic behavior is induced by bilayer-islands formation.

6.2 Co/2MLCu/Pt(111)

Going on with the magnetic characterization of Co islands, we measured the regularly dispersed triangular Co islands described in section 5.2. We performed transverse and polar SMOKE experiments, varying the measurement temperature from 40 K to 220 K. We started with 0.3 ML Co, and increased this coverage up to 2 ML Co. Fig. 6.16 shows STM images between 0.5 and 1.3 ML. At 0.3 ML, the regular network described in section 4.2.1 is present⁵. At higher coverages, islands start to coalesce. Nevertheless, the primary regular pattern is still visible up to 1 ML (Fig. 6.16 c). At 1.3 ML, nothing is visible from the precedent regular islands network anymore. For these four surfaces, no ferromagnetic behavior was recorded. Fig. 6.17 shows examples of the SMOKE signal recorded in these films. Only with 2 ML Co on 2MLCu/Pt(111) did we start to see a ferromagnetic behavior (see Fig. 6.18). However at this coverage, nothing is left from the regular array of Co islands. Any regularity was already lost at 1.3 ML (Fig. 6.16 d)).

The aim in measuring these regularly dispersed small structures was to find-out whether they magnetically interact with each other, because of their high density on the substrate and whether their spatial regularity played any role in their magnetic

⁵On this STM image, the apparent coverage is lower than 0.5 ML. Maybe some exchange between Co and Cu atoms took place. For the other STM images, the apparent coverage corresponds to the deposited coverage according to our flux calibration.

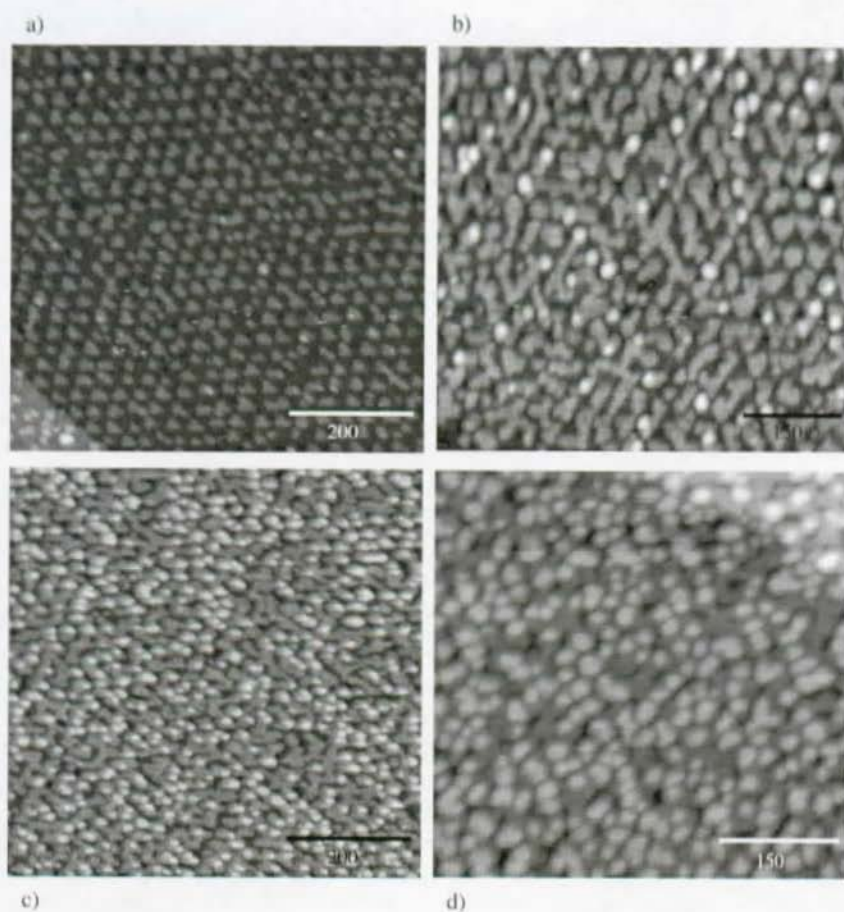


Figure 6.16:

Evolution of the Co island network as a function of the Co coverage.

a) 0.5 ML Co deposited on Pt(111) at 90 K, and annealed to 250 K.

b) 0.65 ML Co deposited on Pt(111) at 95 K, and annealed to 200 K.

c) 1 ML Co deposited on Pt(111) at 95 K, and annealed to 215 K.

d) 1.3 ML Co deposited on Pt(111) at 100 K, and annealed to 300 K.

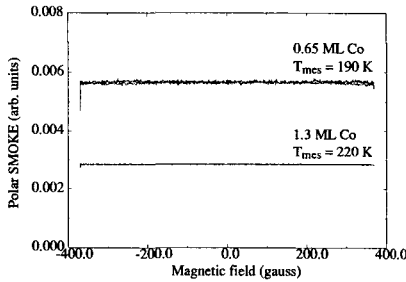


Figure 6.17: Polar SMOKE for films b) (measured at 190 K) and d) (measured at 210 K) shown in Fig. 6.16.

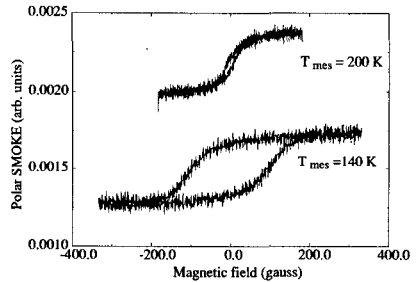


Figure 6.18: Polar SMOKE for 2ML Co deposited on the 2MLCu/Pt(111) network. The hysteresis is clearly evolved up to 200 K. The decreasing H_c value indicates that T_c is close to 200 K, however. Note that at 2 ML, nothing is left from the regular island network.

interaction. However, these small particles are most likely superparamagnetic [91–93]. It turns out that to orient superparamagnetic particles, a magnetic field of 1 to 2 T is needed [92], which is much bigger than our maximum magnetic field of 0.05 to 0.06 T.

6.3 Co/W(100)

In connection with the experimental investigation of correlation between structure and magnetism, this chapter reports results from work done in collaboration with J. Kirschner's group⁶ during a stay of the author in Halle.

We measured the mechanical stress and the magnetic properties of epitaxial Co films on a W(100) substrate. No STM was available for that experiment. However, valuable information could be extracted from LEED and sample bending measurements. We made SMOKE measurements in both the longitudinal and the transverse configurations. For any details of the experimental setup, we refer to [94, 95].

Results for longitudinal and transverse SMOKE as a function of Co coverage up to a film thickness of 80 Å are shown in Figs. 6.19 and 6.20. Measurements were done at two different beam incident angles: 32° and 64° with respect to the sample normal (see inset in Fig. 6.19). For longitudinal SMOKE, a difference of intensity in the signal is visible upon changing the beam incident angle, whereas for transverse SMOKE, almost no change occurs in the signal. Below 3 Å Co – corresponding to 2.5 ML grown pseudomorphic on W(100) – no in-plane magnetization was detectable.

⁶A. Enders, D. Sander and J. Kirschner, at the Max-Planck-Institut für Mikrostrukturphysik, Halle, Germany

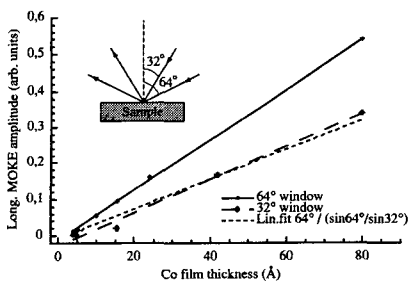


Figure 6.19: Longitudinal SMOKE amplitude as a function of Co film thickness. Measurements are done at two different incident light beam angle: 64° and 32° . The dashed line is the 64° measurement divided by a factor $\frac{\sin(64)}{\sin(32)}$. The resulting line matches the 32° measurement, as expected.

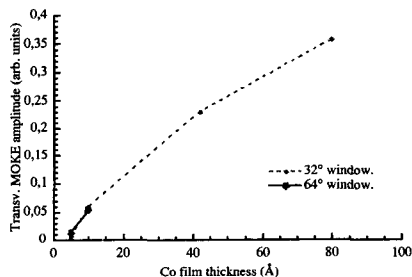


Figure 6.20: Transverse SMOKE amplitude as a function of Co film thickness. In this case, there are no significant differences between measurements made at 64° and 32° .

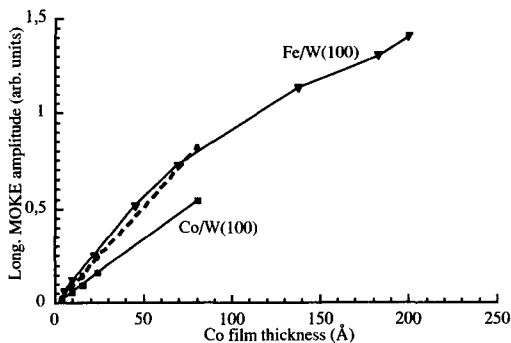


Figure 6.21: Longitudinal SMOKE for Fe and Co films as a function of film thickness. The dashed line is the Co signal multiplied by a factor of 1.5, corresponding to the magnetic moment ratio of Co and Fe surface atoms. It meets quite well the Fe curve. At high coverages, the Fe curve saturates, due to the limited penetration depth of the light beam.

Co and Fe behave in a very similar manner, the Fe giving larger SMOKE signals, as can be seen in Fig. 6.21 where the longitudinal SMOKE amplitude is plotted as a function of film thickness for both metals. This was expected since the magnetic moment per surface atoms in Fe ($= 2.7 \mu_B$) is 1.5 times bigger than in Co atoms ($= 1.8 \mu_B$). Indeed, the Fe magnitude of the MOKE signal is 1.5 times the Co one. Fig. 6.21 shows, along with the longitudinal SMOKE for Co and Fe, the Co curve multiplied by a factor of 1.5. The result, drawn in dashed line, matches the Fe curve.

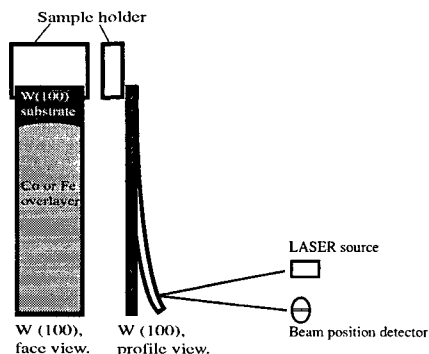


Figure 6.22: Experimental setup for the sample bending measurement. The sample is a thin (0.2mm) W crystal held at one end. Upon deposition of Co or Fe, the sample bends due to the lattice mismatch constraint between the two metals. The sample bending is measured by hitting the sample with a laser beam, the reflected position of which is measured by a split photodiode. The drawing is not to scale.

The SMOKE signal increases linearly, up to a certain value where it saturates, since the light beam has a penetration depth of a few hundreds of angstrom. The saturation is not visible for the Co film since we measured it only up to 80 Å. For the Fe film, the decrease of the slope at high coverages is clearly visible and indicates the limited penetration depth of the light beam.

The SMOKE signal can be correlated with structure through LEED and bending measurements. The substrate is a thin (0.2mm) W crystal which is held by a sample manipulator at one end, the other end being free. It bends upon deposition of Co or Fe due to the constraint resulting of the lattice mismatch between the two metals. Measurement of the bending is done by reflecting a laser beam on the sample and detecting its reflected position with a split photodiode, as sketched on Fig. 6.22 (see references [95,96] for a detailed description of the measurement setup). The deflection of the reflected laser beam is proportional to the sample bending (characterized by the sample curvature radius R), which is related to the film stress σ_F by Stoney's formula [97,98]:

$$\sigma_F = \frac{Et_s^2}{6R(1-\nu)t_F}, \quad (6.1)$$

where t_s and t_f represent the sample and the film thickness, E is the Young modulus of the sample ($E_W = 402$) GPa) and ν its Poisson ratio ($\nu_W = 0.28$) [95,99].

The plot in Fig. 6.23 shows the crystal bending as a function of Co coverage. A positive signal corresponds to a bending in the direction shown on Fig. 6.22, whereas a negative signal corresponds to a bending in the opposite direction⁷. Since the Co lattice

⁷Positive and negative are relative to a zero chosen at the crystal position before starting deposition.

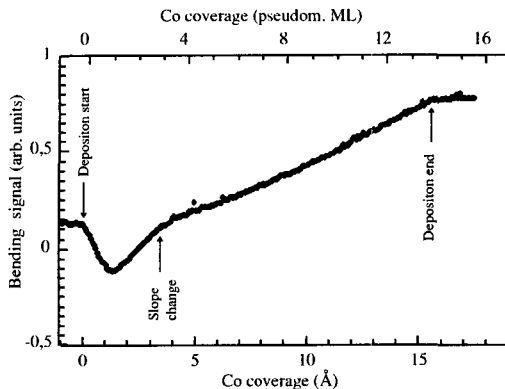


Figure 6.23: Bending signal as a function of Co deposition. The first decrease corresponds to a decrease of the W surface stress (see text). The kink visible at about 3 ML is attributed to a transition between pseudomorphic growth (resulting in an important surface stress), and non-pseudomorphic growth.

unit cell is smaller than the W one, we expect an increasing positive signal upon Co deposition. Actually the bending signal decreases at the beginning, and starts to increase only after about 1 ML Co has been deposited. This first decrease is attributed to a surface stress relaxation. The bare W(100) substrate is stressed because the surface atoms have a lower coordination number and tend to get closer to each other, reproducing the effect of an overlayer made of a material with a smaller lattice constant. This effect happening on both sides, the W substrate remains flat. When Co atoms are deposited on front side of the substrate, the coordination number of the W front side atoms increases, and the surface stress decreases, leading to a negative bending. Only when the first Co monolayer is completed (or nearly completed), does the surface stress increase again, due to Co and W lattice mismatch.

After 1 ML has been deposited,⁸ the bending signal increases linearly up to 3 ML, and the slope of the curve decrease to a lower value for coverages above 3 ML. The bending goes on linearly from 3 ML on up to the coverages measured. This kink in the curve at 3 ML is due to a transition from pseudomorphic to non-pseudomorphic growth, the stress induced by the later being smaller. According to the slopes, the stress drops from 7.7 GPa in the pseudomorphic stage, to 3.6 GPa in the non-pseudomorphic stage [100]. For comparison, Fe/W(100) passes from 9.7 GPa to 1.9 GPa, and Ni/W(100) from 10.6 GPa to 2.3 GPa [100].

LEED measurement gave us information as to whether the Co film was pseudomorphic on the W(100) substrate or not, and at which coverage the transition occurs. When

⁸Unless other specified, by 1 ML we mean that as many Co atoms as the number of surface W atoms has been deposited. This corresponds to the pseudomorphic growth.

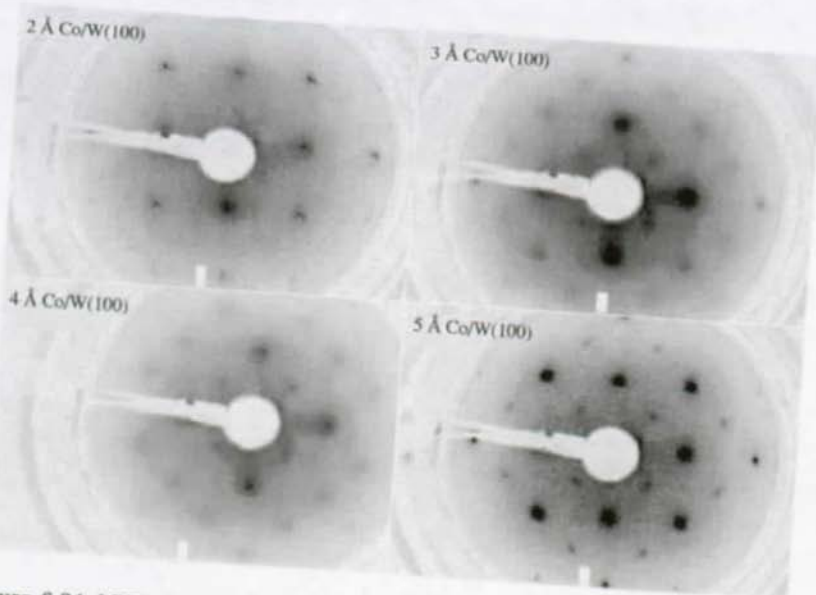


Figure 6.24: LEED measurements of Co films between 2 and 5 Å. The pseudomorph-non pseudomorph transition happens between 2 and 3 Å.

the growth mode is pseudomorph, the LEED figure is similar to the one obtained on the bare W(100) substrate, whereas for non-pseudomorphic growth, new reflection spots appear in the LEED figure, which are characteristic of the crystallographic structure of Co(1120) (see the next paragraph, and Figs. 6.25 and 6.27). Fig. 6.24 shows LEED measurements of Co films of 2, 3, 4 and 5 Å. From these LEED results, we infer that the film is pseudomorph up to a thickness of 2-3 Å, corresponding to 1.8-2.7 ML pseudomorphous Co. Thus the transition pseudomorph- non pseudomorph happens between 1.8 and 2.7 ML.

From the LEED measurements, we may also get information on the epitaxial orientation of Co -which has a hexagonal structure as bulk element- on cubic W(100) face, for thicknesses larger than 3 Å. Fig. 6.25 represents a sketch of the LEED pattern for Co/W(100) for this non pseudomorphic growth, together with the LEED pattern of bare W(100). The LEED spots make an array twice as big in the latter case as in the case of Co/W(100), which means that in real space, the W(100) surface lattice constant is half the one of Co/W(100).

A possible arrangement corresponding to the LEED pattern is shown in Fig. 6.27, where the hexagonal Co(1120) plane is laid on the cubic W(100) plane, which fits with the LEED symmetry. The (1120) hexagonal Co plane nearly matches with the cubic W(100) plane, so that only a small expansion of Co is necessary. We also investigated whether the Co in-plane lattice constant diminishes with film thickness. Within the

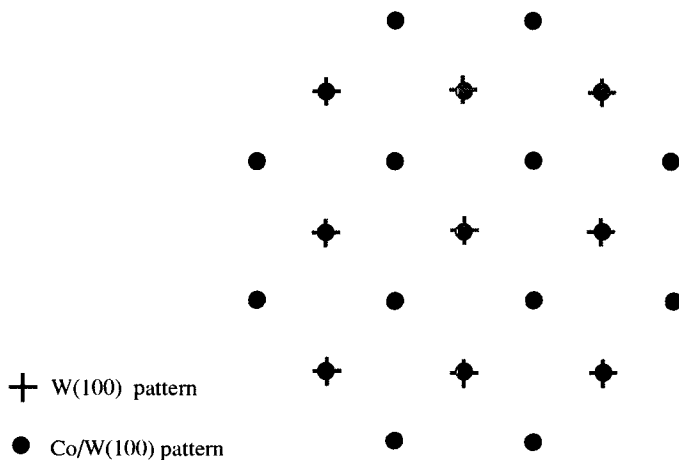


Figure 6.25: Model of the LEED patterns seen in Fig. 6.24.

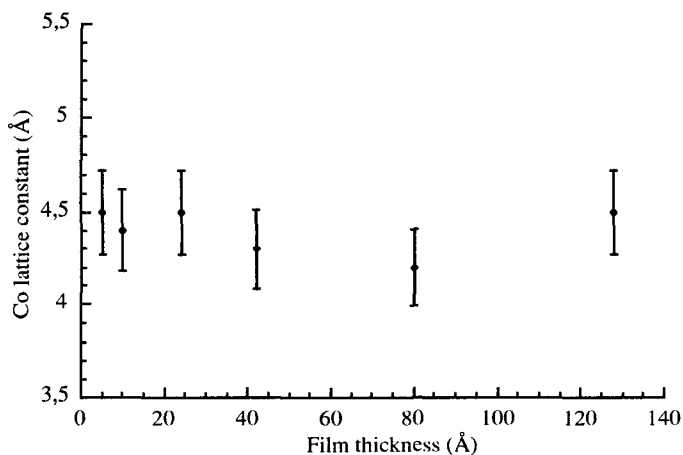


Figure 6.26: The measured lattice constant a (from the LEED patterns) as a function of the Co film thickness. Within the limits of our resolution, no lattice constant evolution is visible with increasing film thickness. The average value for a is 4.4 ± 0.2 Å.

limit of our resolution, and from 5 up to 128 ML, no evolution of the lattice constant was visible. Our results on the plan lattice spacing from LEED experiments are shown on Fig. 6.26.

To summarize our measurements, we see that the onset of in-plane easy axis magnetization corresponds to the end of pseudomorphic growth, as can be deduced from bending

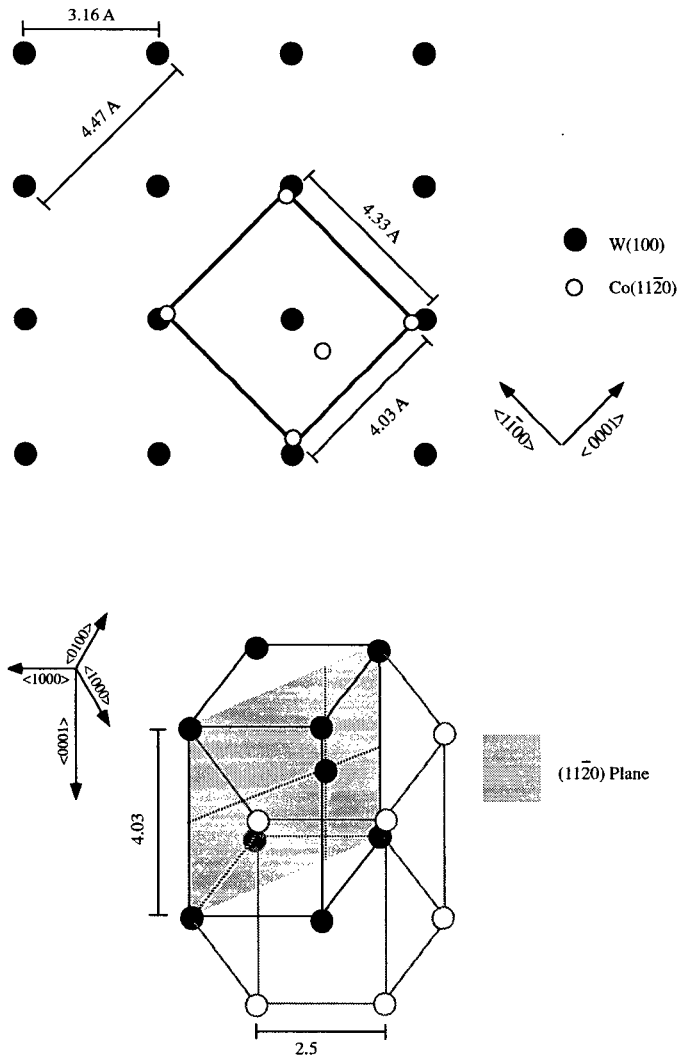


Figure 6.27: Model of a possible configurations for the Co growth on W(100). The lower picture shows the hexagonal Co unit cell (in black), and the (11 $\bar{2}$ 0) plane (in grey). The big hexagonal cell is also shown in light grey lines and white atoms. The upper picture shows the W(100) atoms (black dots) together with the Co(11 $\bar{2}$ 0) atoms (white dots). The atom interspacing is shown, and Co and W atoms are placed in their bulk position. The mismatch between the two metals is of 11 % in the $\langle 0001 \rangle$ direction, and of 3 % in the $\langle \bar{1}100 \rangle$ direction.

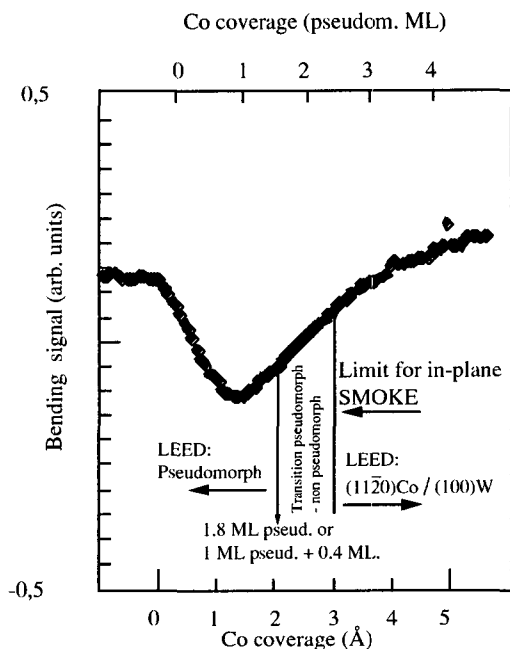


Figure 6.28: Correlation between SMOKE, LEED and bending measurement up to 5 ML. The onset of a ferromagnetic signal corresponds with the transition from non pseudomorph to pseudomorph growth. This transition is visible in LEED measurements, but also in the sample bending measurement. The bending slope is different before and after the pseudomorph non-pseudomorph transition.

and LEED measurements. Correspondences between LEED, SMOKE and bending measurements are summarized in Fig. 6.28. We are tempted to conclude that when the Co atoms interspacing is too big, no ferromagnetism can occur, and that ferromagnetism appear only for non-pseudomorphic growth of Co on W(100). However, this is not necessarily true. The reason for these results may simply come from the fact that the layer is too thin to show a magnetic behavior. It could also be that our resolution is not good enough to detect magnetism below 2.5 ML, or that the magnetization turns to out-of-plane.

Chapter 7

Conclusion and Outlook

The combination of the two analysis tools, STM (Scanning Tunneling Microscope) for structural characterization and SMOKE (Surface Magneto-Optical Kerr Effect) for magnetic characterization, is a very powerful one. One of the aims of this thesis was to identify suitable magnetic systems which could be tailored to give a high density of magnetic structures in the nanometer size regime, which are homogeneous enough – in terms of their size and shape – to yield meaningful results for single magnetic moments from a macroscopic measurement (e.g. the magnetic measurements as deduced from SMOKE). To achieve that and to be able to preserve the as grown structures, it was necessary to combine a UHV-VT-STM with an *in situ* SMOKE setup. The experimental realization of the latter technique was part of this thesis. We recall here the main results presented on the preceding pages.

Using the variable temperature STM, we made a detailed study of the nucleation and growth of several metallic systems: we determined the crystallographic structures and morphologies of thin films of Ag/Pt(111), Co/Pt(111) and Cu/Pt(111) and studied the strain relief patterns of Ag/Pt(111) and Cu/Pt(111) as a function of the adlayer thickness.

We were particularly interested in the surface dislocations present in these heteroepitaxial systems. For Ag submonolayer films on Pt(111), STM measurements and theoretical calculations shed light on new observations, such as strain relief at edges of small Ag islands, or dislocation disappearance in the completed first ML Ag on Pt(111) induced by the chemical potential shift caused by Ag adatoms on-top of these Ag layers.

With the idea to use patterned substrates to control the nucleation processes, we actively searched for surfaces in which dislocations form a periodic network. These were found for 2ML thick films in the two studied systems Ag/Pt(111) and Cu/Pt(111), under certain growth conditions. In both cases, the dislocation pattern topography was well characterized with the help of STM, leading to structural models of the (n \times n) supercells.

Using these patterned substrates, we were able to fabricate in parallel (*i.e.* to fabricate a large number of particles in one step) highly ordered metallic islands by changing macroscopical parameters such as the sample temperature, the incoming atomic flux or the elements involved (substrate and adsorbate). The atomic processes underlying

the formation of regular islands have been identified. A diffusing adatom encounters different energy barriers and binding energies as it diffuses on the substrate, depending whether it is on a pseudomorphic region or on a dislocation-line, which allows the regular islands to form. The different diffusion barriers were inferred for the model case of Ag/2MLAg/Pt(111) from kinetic Monte-Carlo simulations.

The finding of these self-organized structures and the understanding of their formation is very important for two reasons. Firstly, it is a new perspective for in-parallel fabrication of regular islands. We showed that the procedure of growing island arrays on strain-relief templates is a general one, applicable to a whole series of elements. Secondly, the possibility to grow these island arrays opens the possibility to use them for the study of physical properties of low dimensional and very small structures, which differ from the properties observed in bulk mater. The fact that these metallic islands are ordered and almost mono-dispersed permits the use of integrating techniques to characterize the physical properties such as the magnetism. Despite the averaging over many islands, information on a single island can be inferred since all islands are nearly identical.

Combining SMOKE and STM measurements, we related the structure and magnetism of 2D-islands and thin-layers. For example, SMOKE and STM were used together to investigate the ferromagnetic behavior as a function of coalescence in sub-monolayers, or to determinate at which thickness the rotation of the easy magnetization axis of thin layers occurs. For Co films, a marked increase in coercive field was observed at a coverage of 1 ML. Magnetic measurement as a function of measurement- or preparation-temperature were also performed. They allowed the determination of the Curie temperature for thin films. Finally, measurements were performed on the regularly dispersed islands. For these very small structures however we were limited by the maximum available magnetic field in our chamber (0.5-0.6 T). Indeed these small structures are believed to be superparamagnetic, and 1 to 2 T is necessary to align their magnetic moments, and to obtain a saturated signal [92].

For further experiments, some changes of our experimental chamber are planed. For the magnetic measurement in particular, two improvements are scheduled. We shall install a larger magnet in the UHV chamber. This will allow the measurement of small particles, which are shown to have a superparamagnetic behavior (see for example [91-93]). It would also permit the sample saturation in the Co ML range, where the coercive field was found to increase dramatically.

Another possibility to improve magnetic measurements is by replacing our present Pt(111) crystal by an ultraflat crystal substrate, since the magnetic behavior turned out to be extremely sensitive to the step density. In addition, this would reduce the magnetic measurement noise due to light scattering upon reflection at macroscopical defects such as scratches. Naturally, the possibility to change the sample temperature is very important in all our measurements. The available temperatures range is wide, from ~ 40 K to more than 1400 K. The extension of this range to lower temperatures would be a further improvement, since magnetic behavior largely depends on sample temperature. In particular, it was found that the thinner the film, the lower is the

Curie temperature. It may be that for certain structures with reduced dimensions, the Curie temperature is below ~ 40 K, in which case the ferromagnetic behavior would be hidden.

The possibilities of combined measurements with STM and SMOKE are still numerous. Here are some ideas of possible measurements with our present experimental setup: Firstly, most of our magnetic measurements were done on cobalt. It would be interesting to investigate in more detail the magnetic behavior of iron, especially for the small regular islands shown in section 5.2, since iron has a bigger magnetic moment than Co. Similarly, measurements on Ni would be rewarding because its coercive field is smaller than that of Co, being thus easier to magnetize at low temperatures. Second, we did not investigate the magnetization as a function of alloy formation. By heating the films, or by growing them at higher temperatures, it is possible to form surface alloys between the substrate and the adsorbate. Controlled alloy formation is also possible by evaporating simultaneously two elements, or by forming inhomogeneous islands by successive deposition of different materials. To which extent this surface alloying influences ferromagnetism would be interesting to measure, since it will give information on the spin interaction as a function of magnetic atom interspacing. Also, the coercive field could be adjusted by controlling the percentage of each element in the alloy. Finally, in the submonolayer range, other properties could be measured. For example, the magnetism of fractal islands versus compact islands, of elongated islands condensated at steps, and so on. Many other possibilities exist, the above ideas being only examples of possible measurements.

Appendix A

Signification of the main symbols used:

Symbols used in chapter 2

χ_m :	Magnetic susceptibility	$\mathbf{M} = \chi_m \mathbf{H}$
χ_e :	Electric susceptibility	$\mathbf{P} = \chi_e \epsilon_0 \mathbf{E}$
μ :	Magnetic permeability	$\mu = \frac{\mathbf{B}}{\mathbf{H}} = \mu_0(1 + \chi_m)$
σ :	Electric conductivity	$\mathbf{j} = \sigma \mathbf{E}$
ϵ :	Dielectric function	$\epsilon = \frac{\mathbf{D}}{\mathbf{E}} = \epsilon_0(1 + \chi_e)$
κ :	Dielectric permittivity tensor	$\kappa = (1 + \chi_e) = \epsilon/\epsilon_0$

Symbols used in chapter 4

T:	Sample temperature (K)
F:	Deposition flux ($\frac{atoms}{seconds \times lattice site}$)
ν_0 :	Attempt frequency for diffusion to adjacent lattice site
ν_{dl} :	Attempt frequency for diffusion across surface partial dislocation
E_m :	Intracell energy barrier
E_{dl} :	Intercell energy barrier
n_1 :	Adatom density ($\frac{atoms}{lattice site}$)
n_x :	Island density ($\frac{islands}{lattice site}$)
D:	Diffusion coefficient ($\frac{lattice sites}{seconds}$)
σ_1 :	Capture rate of monomers
σ_x :	Capture rate of clusters
i:	Critical nucleus size

Appendix B

List of the acronyms used in the text

AES:	Auger Electron Spectroscopy
LCP:	Left Circularly Polarized light
LEED:	Low Energy Electron Diffraction
MBE:	Molecular Beam Epitaxy
MO:	Magneto-Optical
MOKE:	Magneto-Optical Kerr Effect
Piezo:	Piezoelectric crystal
RCP:	Right Circularly Polarized
SMOKE:	Surface Magneto-Optical Kerr Effect
STM:	Scanning Tunneling Microscope
UHV:	Ultra High Vacuum

Bibliography

- [1] Miniaturization in electronic devices and detectors is very important in astronomy, where the maximum size and weight of spatial instruments is limited. See for example: P. Jakobsen, ASP Conf. Series, **164**, 397 in "Ultraviolet-Optical Space Astronomy Beyond HST" Ed. J.A. Morse, J.M. Shull and A.L. Kinney (1999). P. Gare, R. Engelhardt, A. van Dordrecht *et al*, Spie **1159**, 433, in "X-Ray and Gamma-Ray instrumentation for Astronomy and Atomic physics" (1989).
- [2] Medical applications of nanotechnology are, for example, biosensor used to measure the concentration of substances such as insulin within a living body, or the implant technology for which the interface layers play a decisive part in determining the rejection or acceptance of a foreign body.
- [3] see for example R.P. Cowburn and M.E. Welland, *SCIENCE* **287**, 1466, (2000).
- [4] E. Bauer, Z. Krist. **110**, 372 (1958).
- [5] E. Bauer and J. v.d. Merwe, Phys. Rev. B **33**, 3657 (1986).
- [6] J. A. Venables, G. D. T. Spiller, and M. Hanbücken, Rep. Prog. Phys. **47**, 399 (1984).
- [7] H. Röder *et al.*, Nature **366**, 141 (1993).
- [8] H. Brune, C. Romainczyk, H. Röder, and K. Kern, Nature **369**, 469 (1994).
- [9] H. Brune *et al.*, Surf. Sci. Lett. **349**, L115 (1996).
- [10] G. Binnig, H. Rohrer, C. Gerber, and E. Weibel, Phys. Rev. Lett **49**, 57 (1982).
- [11] G. Binnig and H. Rohrer, Helvetica Physica Acta **55**, 726 (1982).
- [12] D. Eigler and E. Schweizer, Nature **344**, 524 (1990).
- [13] M. F. Hommie, C. P. Lutz, and D. M. Eigler, Science **262**, 218 (1993).
- [14] B. Jonker *et al.*, Phys. Rev. Lett. **57**, 142 (1986).
- [15] P. F. Carcia, J. Appl. Phys. **63**, 5066 (1988).
- [16] M. Baibich *et al.*, Phys. Rev. Lett. **61**, 2472 (1988).

- [17] G. Binash, P. Grünberg, F. Saurenbach, and W. Zinn, Phys. Rev. B **39**, 4828 (1989).
- [18] M. Faraday, Phil. Trans. R. Soc. **131**, 1 (1846).
- [19] J. Kerr, Phil. Mag. **3**, 321 (1877).
- [20] J. Kerr, Phil. Mag. **5**, 161 (1878).
- [21] S. Bader, J. Magn. Magn. Mater. **100**, 440 (1991).
- [22] E. R. Moog, J. Zak, M. L. Huberman, and S. D. Bader, Phys. Rev. B. **39**, 9496 (1989).
- [23] E. Palik, *Handbook of Optical Constants of Solids* (Academic Press, Orlando FL, 1985).
- [24] P. Argyres, Phys. Rev. **97**, 334 (1955).
- [25] H. Bennet and E. Stern, Phys. Rev. A **137**, 448 (1965).
- [26] H. Ebert, Rep. Prog. Phys. **59**, 1665 (1996).
- [27] P. M. Oppeneer, T. Maurer, J. Sticht, and J. Kübler, Phys. Rev. B. **45**, 10924 (1992).
- [28] V. N. Antonov, V. P. Antropov, and B. N. Harmon, Phys. rev. B. **59**, 14552 (1999).
- [29] L. D. Landau and E. M. Lifshitz, *Electrodynamics of Continuous Media* (Pergamon, New York, 1984).
- [30] M. J. Freiser, IEEE trans. on magn. **Mag-4**, 152 (1968).
- [31] C.-Y. You and S.-C. Shin, Appl. Phys. Lett. **69**, 1315 (1996).
- [32] C. S. Wang and J. Callaway, Phys. Rev. B. **9**, 4897 (1974).
- [33] V. L. Moruzzi, J. F. Janak, and A. R. Williams, *Calculated Electronic Properties of Metals* (Pergamon, New York, 1978).
- [34] J. Callaway and C. S. Wang, Phys. Rev. B. **7**, 1096 (1973).
- [35] H. Brune, H. Röder, K. Bromann, and K. Kern, Thin Solid Films **264**, 230 (1995).
- [36] H. Röder, H. Brune, J.-P. Bucher, and K. Kern, Surf. Sci. **298**, 121 (1993).
- [37] K. Bromann, Ph.D. thesis, Ecole Polytechnique Fédérale de Lausanne, Switzerland, 1997.
- [38] J. A. Venables, Philos. Mag. **17**, 697 (1972).

- [39] J. A. Venables, Phys. Rev. B. **36**, 4153 (1987).
- [40] H. Brune, Surf. Sci. Rep. **31**, 121 (1998).
- [41] H. Brune *et al.*, Phys. Rev. B. **60**, 5991 (1999).
- [42] J. Shen *et al.*, Phys. Rev. B. **56**, 2340 (1997).
- [43] J. Hauschild, H. J. Helmers, and U. Gradmann, Phys. Rev. B. **57**, R677 (1998).
- [44] M. B. P. Gambardella, H. Brune, K. Kuhnke, and K. Kern, Phys. Rev. B. **61**, 2254 (2000).
- [45] V. Marsico, M. Blanc, K. Kuhnke, and K. Kern, Phys. Rev. Lett. **78**, 84 (1997).
- [46] D. Chambliss, R. Wilson, and S. Chiang, Phys. Rev. **66**, 1721 (1991).
- [47] J. A. Meyer, J. D. Baikie, E. Kopatzki, and R. J. Behm, Surf. Sci. **365**, 647 (1996).
- [48] S. Esch, M. Hohage, T. Michely, and G. Comsa, Phys. Rev. Lett. **72**, 518 (1994).
- [49] M. Bott, M. Hohage, T. Michely, and G. Comsa, Phys. Rev. Lett. **70**, 1489 (1993).
- [50] S. Liu, L. Bönig, J. Detch, and H. Metiu, Phys. Rev. Lett. **74**, 4495 (1995).
- [51] H. van der Vegt, H. Pinxteren, M. Lohmeier, and E. Vlieg, Phys. Rev. Lett. **68**, 3335 (1992).
- [52] H. Brune, K. Bromann, H. Röder, and K. Kern, Phys. Rev. B. **52**, 14380 (1995).
- [53] J. A. Meyer, P. Schmid, and R. J. Behm, Phys. Rev. Lett. **74**, 3864 (1995).
- [54] T. Michely, M. Hohage, S. Esch, and G. Comsa, Surf. Sci. **349**, L89 (1996).
- [55] B. Fischer *et al.*, Phys. Rev. Lett. **82**, 1732 (1999).
- [56] J. Jacobsen, K. W. Jacobsen, and P. Stoltze, Surf. Sci. **317**, 8 (1994).
- [57] Y. Tanishiro *et al.*, Surf. Sci. **111**, 395 (1981).
- [58] A. R. Sandy *et al.*, Phys. Rev. Lett. **68**, 2192 (1992).
- [59] H. Brune, H. Röder, C. Boragno, and K. Kern, Phys. Rev. B **49**, 2997 (1994).
- [60] J. V. Barth, H. Brune, G. Ertl, and R. J. Behm, Phys. Rev. B **42**, 9307 (1990).
- [61] S. Narasimhan and D. Vanderbilt, Phys. Rev. Lett. **69**, 1564 (1992).
- [62] J. C. Hamilton and S. M. Foiles, Phys. Rev. Lett. **75**, 882 (1995).
- [63] K. Bromann, H. Brune, M. Giovannini, and K. Kern, Surf. Sci. **388**, L1107 (1997).

- [64] J. Jacobsen *et al.*, Phys. Rev. Lett. **75**, 489 (1995).
- [65] S. M. Foiles, Surf. Sci. **292**, 5 (1993).
- [66] J. C. Hamilton *et al.*, Phys. Rev. Lett. **82**, 4488 (1999).
- [67] C. Günter, J. Vrijmoeth, R. Q. Hwang, and R. J. Behm, Phys. Rev. Lett. **74**, 754 (1995).
- [68] H. Brune, M. Giovannini, K. Bromann, and K. Kern, Nature **394**, 451 (1998).
- [69] A. R. Miedema, Z. Metallkde **69**, 287 (1978).
- [70] C. Boragno, H. Röder, H. Brune, and K. Kern (unpublished).
- [71] C. Günter *et al.*, Phys. Chem. **97**, 522 (1993).
- [72] R. Q. Hwang *et al.*, J. Vac. Sci. Technol. **A10**, 1970 (1992).
- [73] J. Vrijmoeth, C. Günter, J. Schröder, and R. J. Behm, in *Magnetism and Structure in System of Reduced Dimension* (R. F. C. Farrow (Ed.), New York, 1993), Chap. P. 55.
- [74] B. Voigtländer, G. Meyer, and N. M. Amer, Surf. Sci. **255**, L529 (1991).
- [75] J. A. Stroschio, D. T. Pierce, R. A. Dragoset, and P. N. First, J. Vac. Sci. Technol. **A 10**, 1981 (1992).
- [76] T. Michely, M. Hohage, M. Bott, and G. Comsa, Phys. Rev. Lett. **70**, 3943 (1993).
- [77] S. Ovesson, A. Bogicevic, and B. I. Lundqvist, Phys. Rev. Lett. **83**, 2608 (1999).
- [78] R. Allenspach and A. Bischof, Phys. Rev. Lett. **69**, 3385 (1992).
- [79] N. W. E. McGee, M. T. Johnson, J. J. de Vries, and J. aan de Stege, J. Appl. Phys. **73**, 3418 (1993).
- [80] W. Weber *et al.*, Phys. Rev. Lett **76**, 3424 (1996).
- [81] J. C. Gay and R. Richter, Phys. Rev. Lett. **56**, 2728 (1986).
- [82] C. S. Shern *et al.*, Surf. Sci. **429**, L497 (1999).
- [83] M. Albrecht, U. Gradmann, T. Furubayashi, and W. A. Harrison, Europhys. Lett. **20**, 65 (1992).
- [84] M. Albrecht, T. Furubayashi, U. Gradmann, and W. A. Harrison, J. Magn. Magn. Mater. **104-107**, 1699 (1992).
- [85] U. Gradmann, *Handbook of Magnetic Materials* (Elsevier Science Publishers, Amsterdam, 1993), Vol. 7, p. 1.

- [86] A. V. Smirnov and A. M. Bratkovsky, *Phys. Rev. B* **54**, R17371 (1996).
- [87] Q. Y. Jin, H. Regensburger, R. Vollmer, and J. Kirschner, *Phys. Rev. Lett.* **80**, 4056 (1998).
- [88] D. P. Pappas, K. P. Kämper, and H. Hopster, *Phys. Rev. Lett.* **64**, 3179 (1990).
- [89] D. Pescia and V. L. Pokrovsky, *Phys. Rev. Lett.* **65**, 2599 (1999).
- [90] H. Brune, C. Boragno, and K. Kern (unpublished).
- [91] J. Xu, M. Howson, B. Hickey, and D. Greig, *Phys. Rev. B* **55**, 416 (1997).
- [92] S. Padovani, I. Chado, F. Scheurer, and J. Bucher, *Phys. Rev. B* **59**, 11887 (1999).
- [93] S. Padovani, F. Scheurer, I. Chado, and J. Bucher, *Phys. Rev. B* **61**, 72 (2000).
- [94] D. Sander, A. Enders, and J. Kirschner, *IEEE Trans. Magn.* **34**, 2015 (1998).
- [95] D. Sander, *Rep. Prog. Phys.* **62**, 809 (1999).
- [96] D. Sander, A. Enders, and J. Kirschner, *Rev. Sci. Instrum.* **66**, 4734 (1995).
- [97] G. G. Stoney, *Proc. R. Soc. London ser. A* **82**, 122 (1909).
- [98] A. Brenner and S. Senderoff, *Res. Natl. Bur. Stand.* **42**, 105 (1949).
- [99] D. Sander, A. Enders, and J. Kirschner, *J. Magn. Magn. Mater.* **198-199**, 519 (1999).
- [100] T. Gutjahr-Löser, Ph.D. thesis, MPI Halle, 1999.

List of Publications

1. *Pseudomorphic growth induced by chemical adatom potential.*
K. Bromann, H. Brune, M. Giovannini, and K. Kern
Surf. Sci. **388**, L1107 (1997).
2. *Self-organized growth of nanostructure arrays on strain-relief patterns.*
H. Brune, M. Giovannini, K. Bromann, and K. Kern
Nature **394**, 451 (1999).
3. *Self-organized growth of cluster arrays.*
K. Bromann, M. Giovannini, H. Brune, and K. Kern
Eur. Phys. J. D **9**, 25 (1999).
4. *Dislocation structure of submonolayer films near the commensurate-incommensurate phase transition: Ag on Pt(111).*
J. C. Hamilton, R. Stumpf, K. Bromann, M. Giovannini, K. Kern, and H. Brune
Phys. Rev. Lett. **82**, 4488 (1999).

Curriculum Vitae

Name: Giovannini Marcella

Date of Birth: January 5 1970

Nationality: Swiss

1986–1989 High School at the Collège Voltaire, Geneva Switzerland

1989–1990 Journey in South-America

1990–1996 Studies in physics at the University of Geneva Switzerland
Diploma thesis in the group of Prof. R. Flückiger, on the $\text{YBa}_2\text{Cu}_3\text{O}_{7-\delta}$ superconductor.

1996–2000 Research and teaching assistant in the group of Prof. K. Kern
at the Institute for Experimental Physics of the Swiss Federal
Institute of Technology in Lausanne (EPFL)

Winter 1998 Joint research studies with the group of Prof. J. Kirschner
at the Max-Planck-Institute für Mikrostrukturphysik, Halle,
Germany.

2000 PhD thesis: “Metallic thin layers and nanostructures: fabrication and characterization”

Remerciements

J'aimerais remercier tous ceux qui m'ont accompagnée et aidée pour la réalisation de ce travail.

En premier lieu, je remercie ici mon directeur de thèse Klaus Kern, qui m'a donné l'opportunité d'effectuer cette recherche au sein de son groupe, ainsi que les membres du jury qui ont bien voulu juger cette thèse.

Je veux ensuite remercier Karsten Bromann, mon prédécesseur, avec qui j'ai travaillé plus d'un an et qui m'a transmis son savoir-faire expérimental. J'ai profité de nombreuses discussions scientifiques avec lui, et ses qualités humaines en ont fait un ami avec lequel il m'a toujours été très agréable de travailler. Je veux également remercier Harald Brune qui a supervisé ce travail. Il m'a fait profiter de ses grandes compétences tant expérimentales que théoriques, et a effectué une relecture critique de mon manuscrit.

D'autres personnes ont relu mon manuscrit pour en corriger l'anglais. Je pense surtout à Véronique Mailly qui a relu la presque totalité de ma thèse. Merci à elle et aux autres pour leur gentillesse et leur patience.

Je veux encore remercier tous les doctorants et post-docs du groupe Kern, qui participent à une bonne ambiance de travail, en particulier ceux avec qui j'ai eu la chance de partager le bureau pour des périodes plus ou moins longues. Plus généralement, j'aimerais remercier tous les membres de l'IPE qui rendent l'atmosphère de travail agréable et détendue. Tous ceux avec qui je suis allée une fois ou l'autre discuter d'un problème physique, qui ont partagé avec enthousiasme leurs connaissances particulières dans un domaine, ou plus simplement avec qui je suis allée manger ou prendre un café durant ces trois ans et demi de recherche. Beaucoup sont devenus des amis. Merci à tous.

La réalisation de ce travail n'aurait pas été possible sans le concours de l'équipe technique. J'aimerais en particulier remercier André Guisolan, Gilles Grandjean, Claude Blanc, Philippe Zürcher et Michel Fazan pour toutes les pièces fabriquées ainsi que Philippe Cordey et Arnold Vonnez pour les réparations (toujours urgentes) d'appareils électroniques. Un grand merci aussi à Martial Doy et Andrea Testa, les indispensables

experts en informatique.

Pendant ma thèse, j'ai pu profiter d'un séjour au *Max-Planck-Institut für Mikrostrukturphysik* à Halle, en Allemagne. Je m'y suis familiarisée avec la technique de mesure magnétique utilisée dans ma thèse. J'aimerais remercier le prof. J. Kirschner de m'avoir accueillie dans son groupe, ainsi que Dirk Sander et Axel Ender qui m'ont très gentiment intégrée dans leur équipe de recherche.

Un grand merci enfin à mes parents pour tout ce qu'ils m'ont apporté et m'apportent encore, ainsi qu'à mon mari pour son amour et son soutien constant.